# EFFECT OF FRICTION STIR PROCESSING ON FRACTURE TOUGHNESS AND CRACK GROWTH BEHAVIOUR OF FUSION WELDED 5083 GRADE ALUMINUM PLATES

A THESIS SUBMITTED TO
THE GRADUATE SCHOOL OF NATURAL AND APPLIED SCIENCES
OF
MIDDLE EAST TECHNICAL UNIVERSITY

BY

GÜNSELİ AKÇAY

IN PARTIAL FULFILLMENT OF THE REQUIREMENTS
FOR
THE DEGREE OF MASTER OF SCIENCE
IN
METALLURGICAL AND MATERIALS ENGINEERING

JULY 2015

Approval of the thesis:

# EFFECT OF FRICTION STIR PROCESSING ON FRACTURE TOUGHNESS AND CRACK GROWTH BEHAVIOUR OF FUSION WELDED 5083 GRADE ALUMINUM PLATES

submitted by **GÜNSELİ AKÇAY** in partial fulfillment of the requirements for the degree of **Master of Science in Metallurgical and Materials Engineering Department, Middle East Technical University** by,

Prof. Dr. Gülbin Dural Ünver ___________
Dean, Graduate School of **Natural and Applied Sciences**

Prof. Dr. C. Hakan Gür ___________
Head of Department, **Metallurgical and Materials Engineering**

Prof. Dr. C. Hakan Gür ___________
Supervisor, **Metallurgical and Materials Engineering Dept. METU**

**Examining Committee Members:**

Prof. Dr. Vedat Akdeniz _______________
Metallurgical and Materials Eng. Dept. METU

Prof. Dr. C. Hakan Gür _______________
Metallurgical and Materials Eng. Dept. METU

Assoc. Prof. Dr. Y. Eren Kalay _______________
Metallurgical and Materials Eng. Dept. METU

Assist. Prof. Dr. Caner Şimşir _______________
Manufacturing Engineering Dept. Atılım University

Assist. Prof. Dr. Mert Efe _______________
Metallurgical and Materials Eng. Dept. METU

**Date:** 24.07.2015

**I hereby declare that all information in this document has been obtained and presented in accordance with academic rules and ethical conduct. I also declare that, as required by these rules and conduct, I have fully cited and referenced all material and results that are not original to this work.**

Name, Last name : Günseli AKÇAY

Signature :

# ABSTRACT

## EFFECT OF FRICTION STIR PROCESSING ON FRACTURE TOUGHNESS AND CRACK GROWTH BEHAVIOUR OF FUSION WELDED 5083 GRADE ALUMINUM PLATES

Akçay, Günseli

M.S., Department of Metallurgical and Materials Engineering

Supervisor: Prof. Dr. C. Hakan Gür

July 2015, 104 Pages

The purpose was to investigate the effects of post-weld friction stir processing (FSP) on the microstructure and fatigue crack propagation in Aluminum Alloy 5083 H111 weldments. As preliminary study, optimization trials were done in order to decide the type, rotational speed, and travel speed of the FSP tool. Microstructural examinations, hardness and tensile tests were done on as-processed materials. In the second part of the work, FSP was applied on the weld zone of the 5083 H111 plates that were joined by gas metal arc welding and a series of samples were prepared. Tensile, hardness, fracture toughness and fatigue crack propagation tests were carried out on the samples prepared from the base metal, weld metal and FSPed weld metal. Microstructures and fracture surfaces of the samples were investigated by optical microscope and scanning electron microscope. Some improvements in hardness, tensile and fracture properties in the weldment were obtained after FSP, and the results were compared and discussed to explain the reasons and main mechanisms.

**Keywords:** *Aluminum; Gas metal arc welding; Friction stir processing; Fatigue crack propagation.*

# ÖZ

## SÜRTÜNME KARIŞTIRMA PROSESİNİN 5083 ALUMİNYUM ALAŞIMLARININ ERGİTME KAYNAĞI İLE BİRLEŞTİRMELERİNDE ÇATLAK İLERLEME DAVRANIŞINA ETKİSİ

Akçay, Günseli
Yüksek Lisans, Metalurji ve Malzeme Mühendisliği Bölümü
Tez Yöneticisi: Prof. Dr. C. Hakan Gür

Temmuz 2015, 104 Sayfa

Bu çalışmada, sürtünme karıştırma prosesinin (SKP) kaynaklı Aluminum 5083 H111 plakalarının mikroyapı ve çatlak ilerleme davranışına etkisi araştırılmıştır. Ön çalışma olarak farklı dönme hızları, ilerleme hızları ve uç tipleri denenerek SKP parametreleri optimize edilmiştir. Mikroyapı incelemeleri, sertlik ve çekme deneyleri proses uygulanmış malzemelere yapılmıştır. Çalışmanın ikinci kısmında gaz metal ark kaynağıyla birleştirilen 5083 H111 plakalarının kaynak bölgesine sürtünme karıştırma prosesi uygulanmıştır. Çekme, sertlik, kırılma tokluğu ve çatlak ilerleme testleri ana metal, kaynak metali ve SKP uygulanmış kaynak metalinden çıkartılan numunelerle gerçekleştirilmiştir. Tane yapıları ve kırılma yüzeyleri optik mikroskop ve taramalı elektron mikroskobuyla incelenmiştir. Kaynak metalinin sertlik, çekme ve kırılma özellikleri SKP ile iyileştirilmiş ve sonuçların ardında yatan sebepler açıklanmaya çalışılmıştır.

***Anahtar Kelimeler:*** *Aluminyum; Gaz metal ark kaynağı; Sürtünme karıştırma prosesi; Çatlak ilerlemesi.*

*For the campus and people of METU..*

# ACKNOWLEDGMENTS

I sincerely thank my supervisor Prof. Dr. C. Hakan Gür, who guided me during this study.

Dr. Koray Yurtışık and Dr. Süha Tirkeş deserve a profound appreciation for their guidance, support throughout the study.

I deeply appreciate Mr. Göksu Gürer, Mr. Mertcan Başkan, Mr. Shahin T. Firouzeh, M. Mert Karadağlı, Mr. Arif Atalay Özdemir, Mr. Cemal Yanardağ, Mr. Orhan Aydın and Mr. Önder Şahin whose help were invaluable during fabrication and testing processes.

I am grateful to Mrs. Burcu Tolungüç, Mr. Tolga Ertürk, and Mrs. Mine Kalkancı for their encouragement, guidance and support.

Without the support of Odak Kompozit Teknolojileri A.Ş., this thesis might have not finished. I thank all personnel for their sincerity.

Finally, I am deeply in depth to my family for their moral and monetary support.

# TABLE OF CONTENTS

# LIST OF TABLES

TABLES

# LIST OF FIGURES

FIGURES

# CHAPTER 1

# INTRODUCTION

Utilization of aluminum alloys in aerospace, automotive, marine and railway industries is gradually increasing due to their high specific strength and corrosion resistance. Many production routes for the final component or construction include conventional welding techniques namely gas metal arc welding (GMAW) and gas tungsten arc welding (GTAW) [1]. During fusion welding it is critical to minimize formation of discontinuities in the weld metal in order to keep the strength at acceptable levels. Major defects and/or discontinuities encountered in aluminum welding are porosity, hot crack and lack of penetration etc. Although some nondestructive techniques can be applied, micro discontinuities which deteriorate mechanical properties of fusion welds [2] cannot be detected.

Application area of friction stir processing has been growing since its invention. In 1991, friction stir welding (FSW) started to be used as solid-state welding. While it is used for welding of different materials or joining non-fusion weldable materials, friction stir processing (FSP) developed as a local microstructural modification technique by refining grain structure based on the basic principles of friction stir welding. FSW has been found to be superior compared to fusion welding in terms of mechanical strength and environmental friendliness [3, 4]; however, since it is used to join separate parts, FSP is easier process in which the workpiece is bulk.

Friction stir processing is known to cause dynamic recrystallization of matrix, fragmentation and homogenization of secondary particles, elimination of porosities [5-10]. In literature, information about the effect of friction stir processing on fusion welds is lacking. Therefore, application of FSP on weld metal has been investigated.

In this study, friction stir processing was used to modify weld metal structure of 20 mm thick Al 5083 H111 weldments. Three type of tools were tried to optimize friction stir processing. Temperature measurements, tensile tests, grain size calculations, hardness measurements, fracture toughness and fatigue crack propagation tests were done. Fractography of fracture surfaces were investigated by means of scanning electron microscope.

Grains of weld metal were refined and disclosure of macro and micro discontinuities were obtained by friction stir processing. Improved tensile strength, fracture toughness and hardness was obtained. Resistance to crack growth was improved for high stress intensities. However, fatigue crack growth rate of as-welded state has been measured as lowest at low stress intensities.

# CHAPTER 2

# THEORY

## 2.1. AA 5083 Alloy and Its Weldability

Aluminum is known to be most abundant element after oxygen and silicon in Earth's crust. Aluminum alloys have high specific strength, high electrical conductivity and high corrosion resistance. The most important property of aluminum can be its relatively low density, 2.7 g/cm$^3$. All these properties of aluminum extent its application area immensely. Area of use includes transportation vehicles, food packaging, kitchen utensils, defense and aerospace equipment, electrical transmission lines etc.

Aluminum and its alloys are divided in two main classes: cast compositions and wrought compositions. Different identification systems are used to distinguish aluminum alloys depending on their compositions and metallurgical condition. While four digit numbers are used for wrought alloys, three digit numbers with a decimal point are used for cast alloys. In both designations, first digit denotes the major alloying elements. In Table 1, principal alloying elements are given.

Table 1. Designation systems for cast and wrought alloys.

| **Wrought Alloys** | | **Cast Alloy** | |
|---|---|---|---|
| **Alloy Series** | **Principal Alloying Element** | **Alloy Series** | **Principal Alloying Element** |
| 1xxx | 99.000% Minimum Aluminum | 1xx.x | 99.000% Minimum Aluminum |
| 2xxx | Copper | 2xx.x | Copper |
| 3xxx | Manganese | 3xx.x | Silicon Plus Copper and/or Magnesium |
| 4xxx | Silicon | 4xx.x | Silicon |
| 5xxx | Magnesium | 5xx.x | Magnesium |
| 6xxx | Magnesium and Silicon | 6xx.x | Unused Series |
| 7xxx | Zinc | 7xx.x | Zinc |
| 8xxx | Other Elements | 8xx.x | Tin |
| | | 9xx.x | Other Elements |

Aluminum alloys further divided by their temper conditions. As seen in Table 2, two major type of treatments applied on aluminum are strain hardening and heat treatment. Cast alloys are used as heat treated or as-cast conditions; i.e. they are not work hardened. On the other hand, wrought alloys are subdivided into heat-treatable and non-heat-treatable alloys depending on the major strengthening method. 1xxx, 3xxx, 4xxx, and 5xxx series alloys belong to non-heat-treatable alloys. Their strength is derived by solid solution hardening and by strain hardening. Heat-treatable alloys are 2xxx, some 4xxx, 6xxx, and 7xxx series alloys. They are solution heat treated, quenched and age hardened. Further work hardening can be employed.

Table 2. The basic temper designations [11].

| Letter | Meaning |
|---|---|
| **F** | As fabricated – Applies to products of a forming process in which no special control over thermal or strain hardening conditions is employed |
| **O** | Annealed – Applies to product which has been heated to produce the lowest strength condition to improve ductility and dimensional stability |
| **H** | Strain Hardened – Applies to products which are strengthened through cold-working. The strain hardening may be followed by supplementary thermal treatment, which produces some reduction in strength. The “H” is always followed by two or more digits |
| **W** | Solution Heat-Treated – An unstable temper applicable only to alloys which age spontaneously at room temperature after solution heat-treatment |
| **T** | Thermally Treated - To produce stable tempers other than F, O, or H. Applies to product which has been heat-treated, sometimes with supplementary strain-hardening, to produce a stable temper. The “T” is always followed by one or more digits |

In 5xxx series Al-Mg alloys, strength is achieved though mainly work hardening, and solution strengthening and lesser extent by controlling grain size. Primary alloying element, magnesium, has two major effects. It promotes work hardening and increase strength by solid solution hardening.

Equilibrium phase diagram of aluminum - magnesium system shows $Al_3Mg_2$ (β phase) secondary solid phase (Figure 1) and magnesium solid solubility of 1.7 wt% at room temperature. Thermal exposure of these alloys can cause stress corrosion because of the formation of the β phase on grain boundaries. Unlike the phase diagram, Mg content of matrix is usually is high and decomposition is low in commercial alloys. In these series, precipitation hardening is not observed in alloys having less than 5% Mg [12].

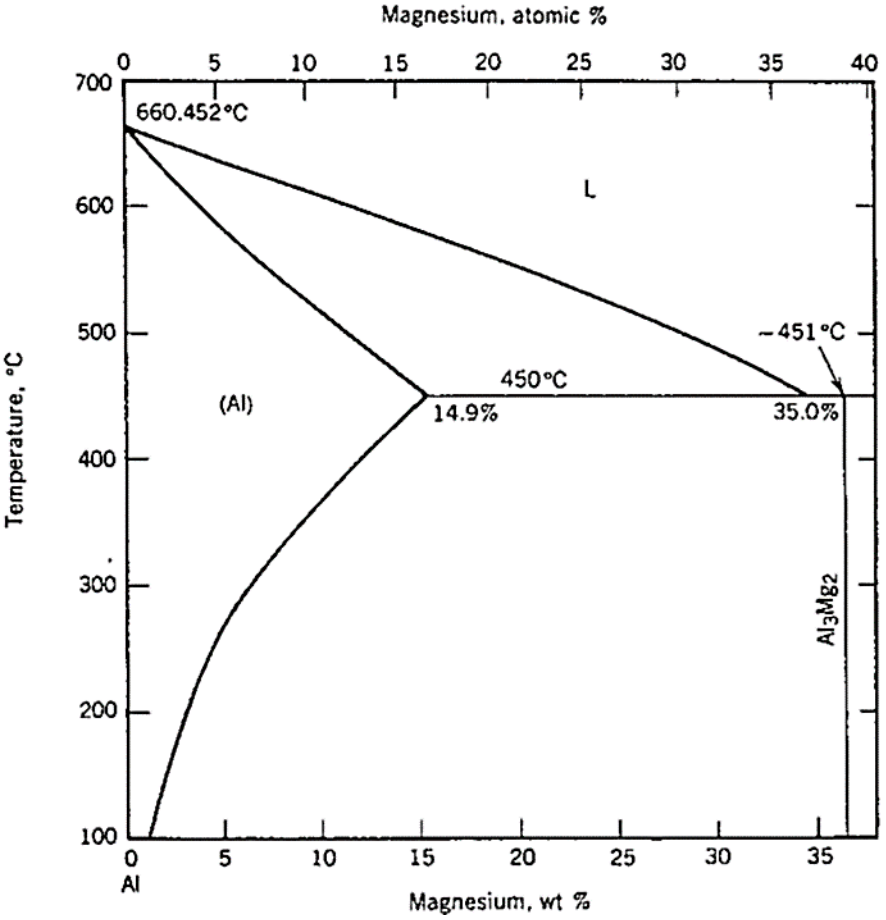

Figure 1. Al-Mg binary phase diagram.

Additional alloying elements such as manganese and zirconium can be added for further strengthening. Mn is used to enhance work hardening and decrease recrystallized grain size. Zr, on the other hand, can be used to decrease grain size.

Generally found phases in 5xxx series include $Mg_2Si$, $Al_6(Fe,Mn)$, $Al_{12}(Fe,Mn)_3Si$, $Al_3Fe$ since silicon and iron are present as impurities. $Mg_2Si$ phase is usually observed in microstructure because of low solubility even though its deleterious effects. Second most commonly observed phase is $Al_6(Fe,Mn)$. This phase is favored because it is known to retard recrystallization.

Aluminum alloy 5083 H111 is the base metal used in this study. It has a typical composition of Al-4.7Mg-0.8Mn-0.1Cr with residual levels of Fe and Si. This aluminum alloy is preferred mainly because of good weldability and good corrosion resistance. It has excellent cold formability and moderate strength. Ship building, unfired welded pressure vessels, armor plates are some utilizations of 5083 aluminum alloys.

Temper condition H111 is work hardened between H11 and H12 conditions. The first digit indicates that only strain hardening is employed. The second digit specifies that one-eight hard strain hardening is obtained (Table 3).

Table 3. H temper condition

| **- The first digit after the h indicates a basic operation:** | |
|---|---|
| **H1** | Strain Hardened Only. |
| **H2** | Strain Hardened and Partially Annealed. |
| **H3** | Strain Hardened and Stabilized. |
| **H4** | Strain Hardened and Lacquered or Painted. |
| **- The second digit after the h indicates the degree of strain hardening:** | |
| **HX2** | Quarter Hard |
| **HX4** | Half Hard |
| **HX6** | Three-Quarters Hard |
| **HX8** | Full Hard |
| **HX9** | Extra Hard |
| **- The third digit indicates variation of two-digit temper.** | |

Tensile properties of Al 5083 alloy in both fully annealed (O temper) and H113 temper conditions are given in Table 4. It is seen that hardening increased tensile strength 9% and yield strength 47%. Elongation, on the other hand decreased with strain hardening. In the table, weldments of Al 5083 can also be compared. Tensile strength of weldments are approximately 6% lower than unwelded plates. Although the elongation of weldments were found to be same, the yield strength of H113 temper is %38 higher than as-welded plate [13].

Table 4. Typical tensile properties of alloy 5083 and its GMA weldments [13].

| | **Tensile strength (MPa)** | **Yield strength (MPa)** | **Elongation %** | **Reduction in area %** | **Notch tensile strength (MPa)** |
|---|---|---|---|---|---|
| **Plate, O temper, longitudinal specimen** | | | | | |
| | 310 | 155 | 20 | 32 | 335 |
| **Plate, O temper, transverse specimen** | | | | | |
| | 315 | 160 | 19 | 26 | 325 |
| **Plate, H113 temper, longitudinal specimen** | | | | | |
| | 335 | 235 | 15 | 23 | 425 |
| **Plate, H113 temper, transverse specimen** | | | | | |
| | 345 | 235 | 16 | 24 | |
| **Weld in O temper plate, 5356 filler metal, longitudinal specimen** | | | | | |
| | 290 | 145 | 15 | 22 | |
| **Weld in H113 temper plate, 5356 filler metal, longitudinal specimen** | | | | | |
| | 295 | 145 | 16 | 30 | 305 |

Aluminum weldments differ from ferrous weldments in many ways due to thermal properties, physical properties and strengthening methods of aluminum alloys. The high reactivity of aluminum with oxygen forms $Al_2O_3$ instantaneously. Although this phase forms as corrosion resistant layer when aluminum is exposed to air, it is electrical insulator. Therefore, it may cause arc instability. High heat transfer coefficient of aluminum also causes fluctuations in heat input which might result in lack of penetration and/or fusion [14]. In Figure 2, some welding defects are shown. Porosity and hot cracks are major problems in aluminum weldments. Distortion and shrinkage voids are also problems encountered aluminum welding due to high thermal expansion coefficient. Due to the strengthening method, loss of precipitation hardening and cold working effects , weld metal and heat affected zone are usually the weakest points in aluminum weldments.

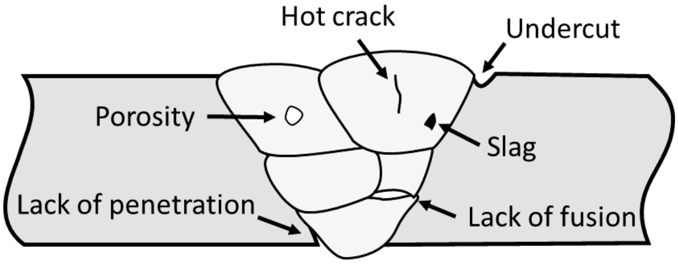

Figure 2. Welding defects.

Weldability of 5xxx series aluminum alloys are higher than precipitation hardened alloys. Dissolution and/or growth of precipitates cause additional strength loss at heat affected zone of heat treatable aluminum weldments. Secondly, presence of precipitate forming elements increases the sensitivity to hot crack.

Hot cracking, solidification cracking, is observed because of low melting eutectics forming along grain boundaries. Cracking in fusion zone can be observed due to segregation of precipitate forming elements during solidification. In HAZ, the high temperature; consequently, high diffusivity may cause formation of eutectics which are responsible for hot cracking. In 5xxx series, hot crack sensitivity is shown to decrease with increased magnesium content (Figure 3). Aluminum 5083 Al-Mg alloy having 4-4.9% magnesium is known to be weldable without difficulty. For aluminum welding, filler alloy can also be selected depending on the magnesium content. For example, filler alloy 5356 which has high amount of magnesium is used in this study.

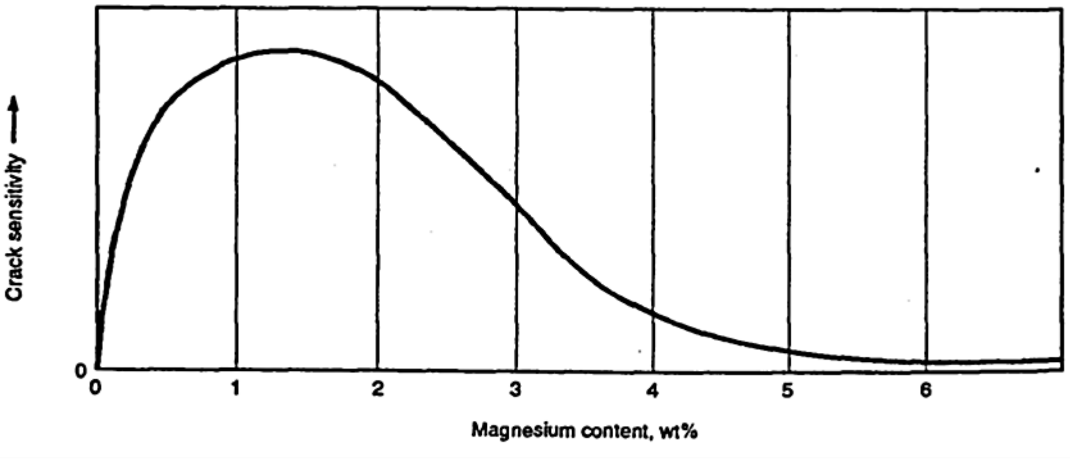

Figure 3. Plot of hot crack sensitivity versus magnesium content to show peak in susceptibility obtained for aluminum-magnesium (5xxx) alloys. [15]

Porosity is one of the main defects encountered in 5xxx series aluminum weldments. The paramount reason behind porosity is the abrupt decrease in hydrogen solubility of aluminum during solidification. Gas molecules are nucleate and grow in bubbles when the metal starts to crystallize. Hydrogen pores might not form if the solidification time is short; however, it might be kept longer in order for hydrogen to escape from weld pool.

For minimum pore density, any hydrogen source must be eliminated. Water, hydrocarbons and hydrated oxides must be cleaned from the surface of base and filler materials. High grade shieling gas should be used. Storage of filler metal and shieling gas must be done carefully.

## 2.2. Welding Processes

### 2.3.1. Fusion Welding

The weldment in fusion welding is formed by solidification of liquid pool of melted surfaces of joining components, usually with molten filler metal. Heat necessary for melting is obtained by various heat sources such as electric arc, electron or laser beam, flame and resistance heating.

The final weld structure is altered by physical and chemical processed induced by the applied heat. Three main zones can be identified as fusion zone (FZ), heat affected zone (HAZ) and unaffected base material (Figure 4) while fusion line represents the liquidus isotherm of base material in two-dimension representation. Fusion zone is where the melting temperature is reached. Upon solidification, the material in the fusion zone is called weld metal. In HAZ, heat is not enough for liquidation; however, it can affect the morphology by annealing, grain growth and precipitation reactions. Microstructure in heat affected zone is formed according to the temperature gradient developed due to local heat input.

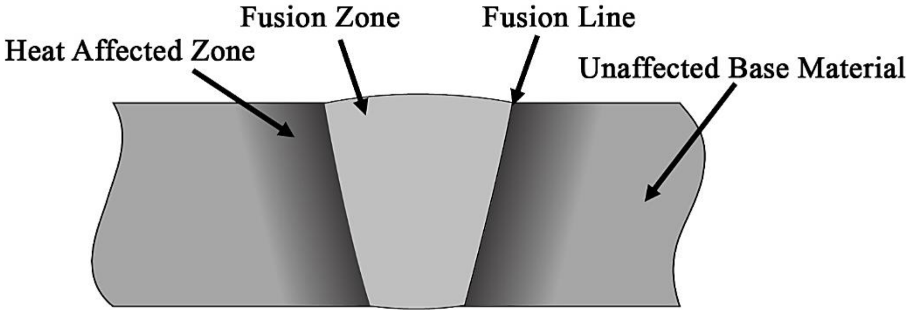

Figure 4. Typical metallurgical zones.

### 2.3.2. Gas Metal Arc Welding (GMAW)

Heating in GMAW is established by an arc formed between consumable continuous filler electrode and the workpiece. Schematic diagram of gas metal arc welding is shown in Figure 5. An electrical current is applied to the tubular contact tube which surrounds the wire electrode. The arc produced because of the current cause local melting and filling of weld gap. In the meantime, a shielding gas is supplied to protect the molten material from ambient atmosphere for controlling the metallurgy.

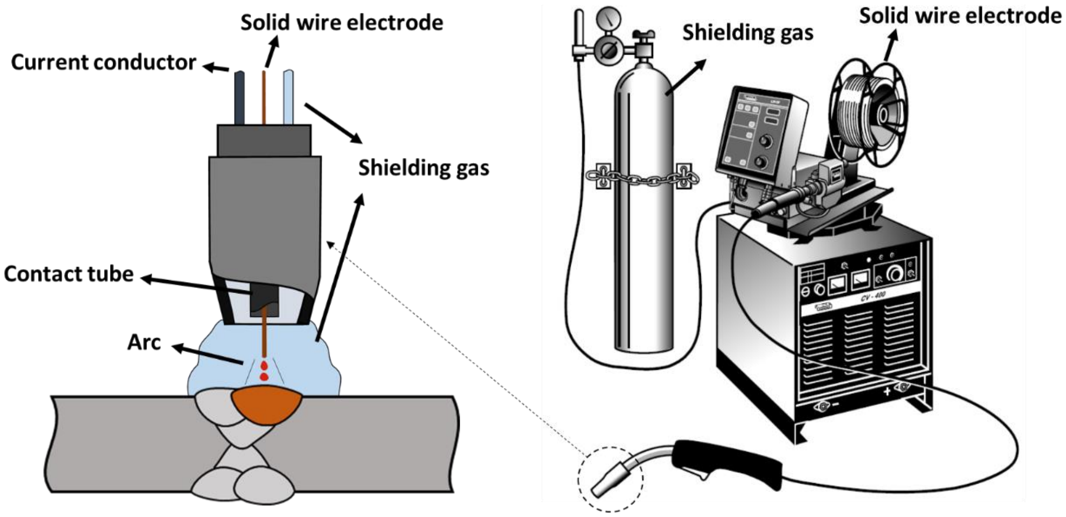

Figure 5. Gas metal arc welding [14].

Shielding gas is selected depending on the materials to be joined. They can be gas mixtures of active gases ($CO_2$ and $O_2$) and/or inert gases (Ar and He). Gas metal arc welding process is also called metal inert gas (MIG) welding when inert gases are used as shielding gas.

Some advantages of gas metal arc welding are its high productivity, less skill level needed for operating personnel and ease of automation. GMA welding of aluminum alloys is also preferred due to the cathodic cleaning action which breaks and disperses the oxide film on surface.

## 2.3. Friction Stir Processing

Friction stir processing is a variant of friction stir welding. Although these two techniques have the exact same principle, they differ in their application area. The aim of friction stir processing is not joining like friction stir welding. It is used for local modification of microstructure in order to improve formability, ductility, mechanical strength etc.

In friction stir processing, a rotating non-consumable tool is inserted into material to be processed and traversed. In Figure 6, schematic diagram of friction stir welding is shown. The workpiece must be clamped to prevent motion of workpiece under exerted forces. A backing plate might be needed to support the workpiece and work as a heat sink. A key hole is usually left at the end which can be prevented or eliminated from the final structure.

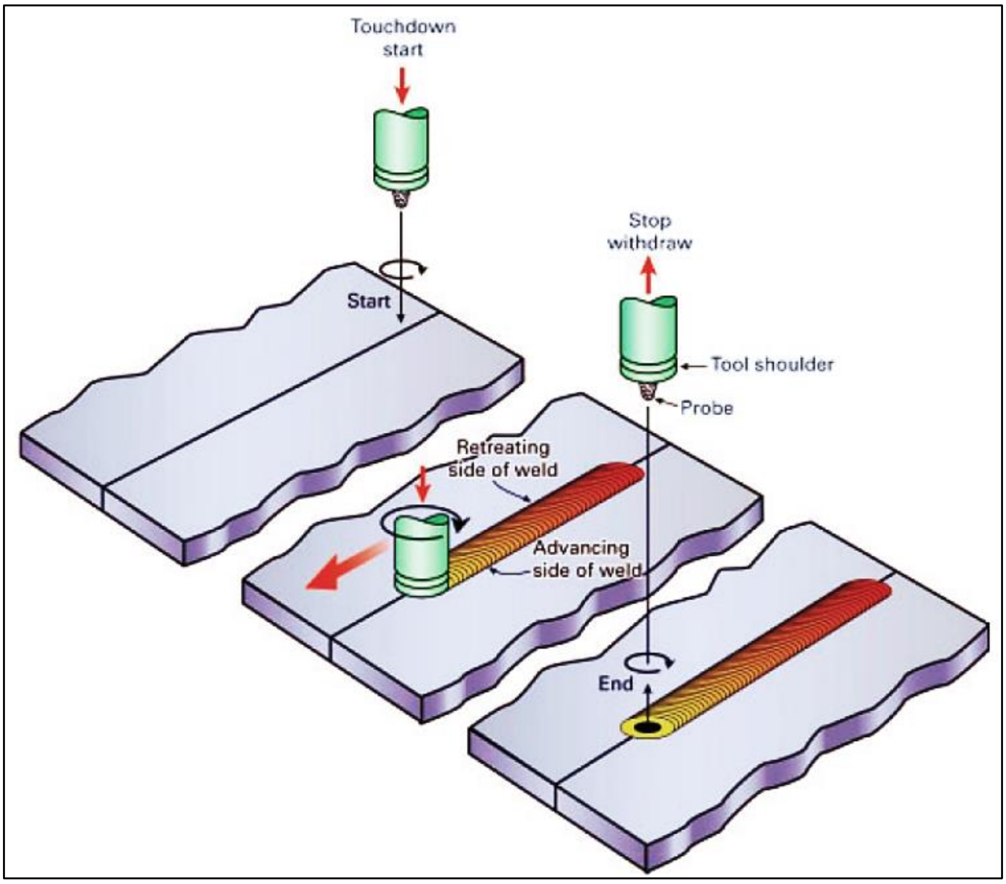

Figure 6. Schematic diagram of friction stir welding [16].

This action of the tool causes severe local plastic deformation and temperature increase due to frictional and adiabatic heating which causes dynamic recrystallization. While recrystallization is preferred for obtaining fine grain structure; the stirring action is favored for homogenizing powder metallurgy alloys, cast materials and also to produce metal matrix composites. Application area of friction stir processing has been expanding since its invention in 2001.

The macro view of single pass of FSP is shown in Figure 7. The process is heterogeneous due to material flow mechanics. The sides of weld center are called advancing side and retreating side. The former is where the direction of travel is parallel to tangential velocity of tool rotation and retreating side is where the two velocity vectors have opposite direction. Flash can form at the top surface due to expelled material from the workpiece-tool interface.

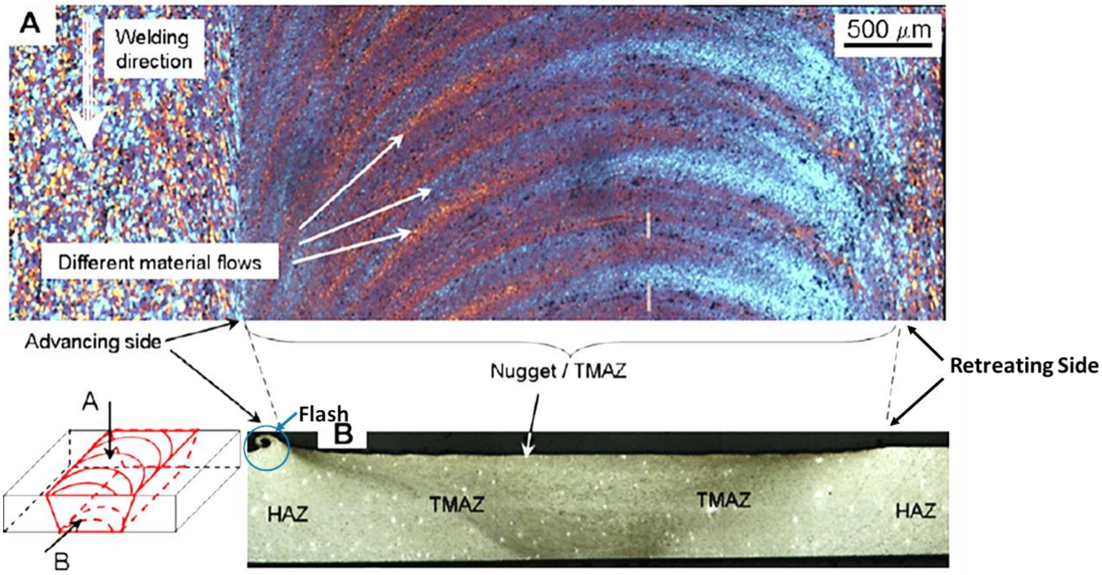

Figure 7. (a) Top view, (b) Cross-section [17].

Although processed zone can form in different shapes; generally four zones are identified in cross-section of friction stir welded/processed parts: nugget or stir zone, thermo-mechanically affected zone (TMAZ), heat affected zone (HAZ) and unaffected base metal.

The nugget experiences high strains and temperatures higher than recrystallization temperature of the material processed. Fine equiaxed grains are observed in this region. In literature, many analyses have been done to understand the mechanism behind the microstructure evolution in nugget; however, conflicting results have been found. Jian-Qing et al. [18] has proposed a multi-mechanism which can explain recovery and recrystallization mechanism (Figure 8).

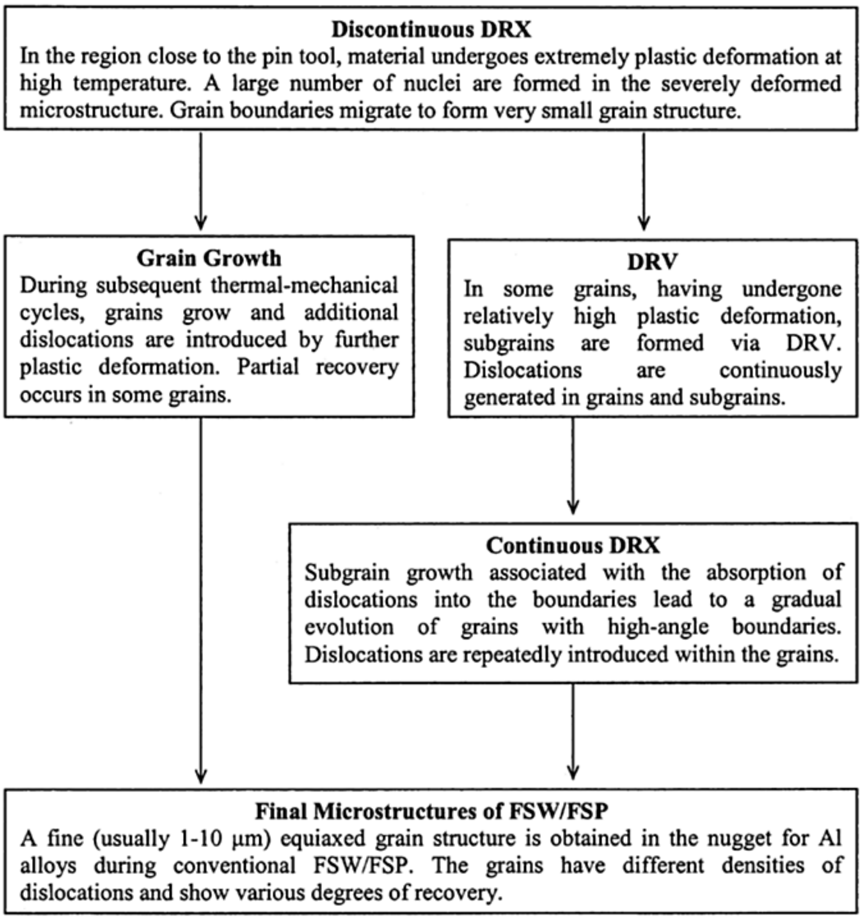

**Discontinuous DRX**

In the region close to the pin tool, material undergoes extremely plastic deformation at high temperature. A large number of nuclei are formed in the severely deformed microstructure. Grain boundaries migrate to form very small grain structure.

**Grain Growth**

During subsequent thermal-mechanical cycles, grains grow and additional dislocations are introduced by further plastic deformation. Partial recovery occurs in some grains.

**DRV**

In some grains, having undergone relatively high plastic deformation, subgrains are formed via DRV. Dislocations are continuously generated in grains and subgrains.

**Continuous DRX**

Subgrain growth associated with the absorption of dislocations into the boundaries lead to a gradual evolution of grains with high-angle boundaries. Dislocations are repeatedly introduced within the grains.

**Final Microstructures of FSW/FSP**

A fine (usually 1-10 μm) equiaxed grain structure is obtained in the nugget for Al alloys during conventional FSW/FSP. The grains have different densities of dislocations and show various degrees of recovery.

Figure 8. Schematic illustration of microstructure evolution during FSW/FSP [18].

The thermo-mechanically affected zone (TMAZ) exhibits deformed grains but not recrystallized grains. High stacking fault energy of aluminum enables high plastic strain without recrystallization. Second phases can be found on grain boundaries due to local heating [19].

In heat affected zone (HAZ), plastic deformation does not occur; however, the heat evolved during processing can cause phase transformations like precipitate coarsening.

Main processing parameters are the tool geometry, travel speed, rotational speed, and downward force or plunge depth. Material properties of the workpiece are important when selection optimum process parameters.

Transverse speed and rotational speed affects the heat generation and material viscosity in opposite ways. As the ratio of rotational speed to transverse speed increases, higher temperatures are obtained. The exposure time to frictional heat is decreased by faster processing. Higher rotational speed increases plastic deformation and material mixing [19].

Downward force or plunge depth should be controlled during friction stir processing. These parameters are necessary for adequate forging of material. Increasing the force or depth of the tool can cause excessive flash formation and higher temperatures. Material thinning and grain growth can be observed which deteriorate mechanical properties.

Influence of tool geometry also includes heat generation and material flow. Moreover, the axial force needed for processing can be decreased by changing the tool design. Friction stir tool usually consists of a pin and a shoulder; however, tools with only shoulder can also be preferred. In Figure 9, some pin designs are shown. Different geometries can be used; for example cylindrical and triangular pins are studied in literature. Geometrical features such as threads, flats or fludes can be machined on pin surface. On the other hand shoulder profiles can be flat, concave or convex. Some shoulder features are shown in Figure 10.

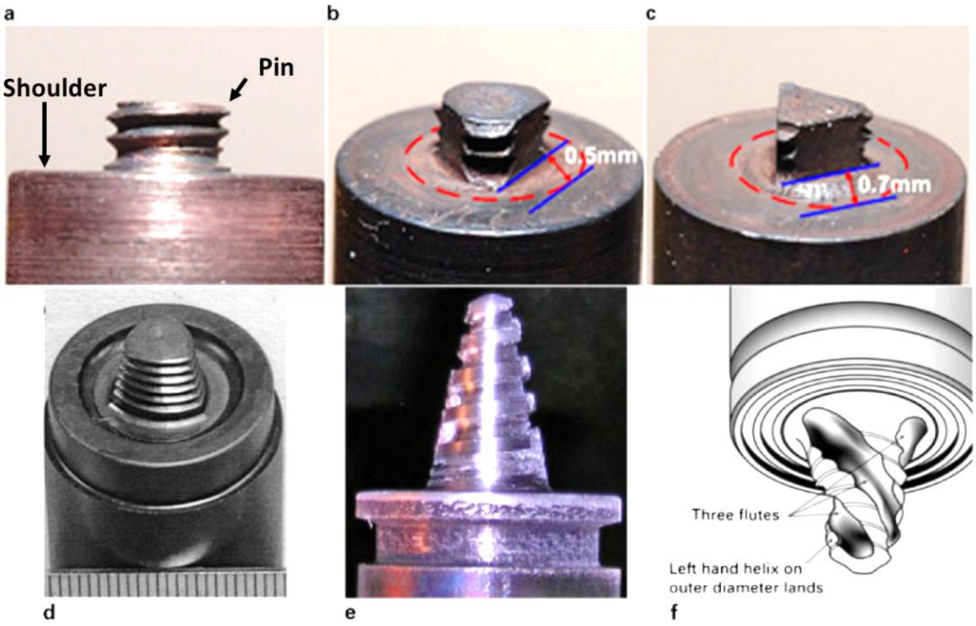

Figure 9. Friction stir pin profiles (a) Cylindrical Threaded, (b) Three flat threaded, (c) Triangular, (d) Trivex, (e) Threaded conical, (f) Triflude [20].

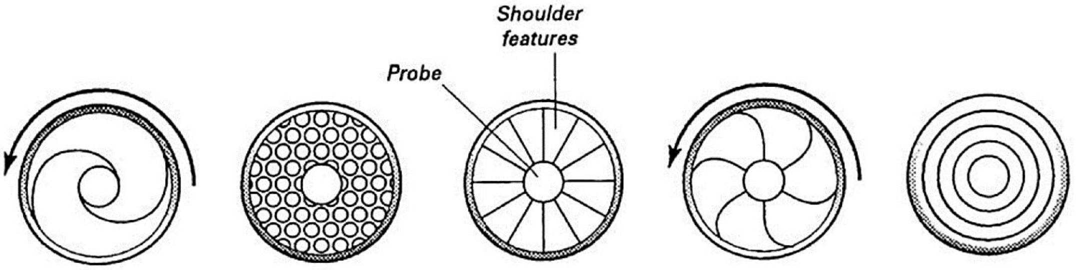

Figure 10. Different shoulder features [4]

Friction stir processing/welding models have been developing in order to understand the mechanism and optimize process parameters; however, trial and error method is usually followed for specific materials and definite geometries. For example, Hidetoshi et al. studied friction stir welding of 5mm thick 5083-O and 1050-H24 plates. They used different travel speed, rotational speed and pin geometries. The triangular prism was found to give best mechanical properties for 5083-O plate at high rotational speed (1500 rpm); while better tensile properties were obtained with columnar pin with threads at medium rotational speed (600 rpm). On the other hand, a columnar tool without threads produced the best weld among 1050-H24 plates in terms of their tensile strength [21].

High heat input during friction stir processing can cause overaging or dissolution of strengthening precipitates in heat-treatable alloys and loss of work hardening in strain hardened alloys. Therefore, process parameters should be selected as to be hot enough for material flow but cold enough for better mechanical properties. To keep the temperature of material minimum, lower ratio of rotational speed to travel speed can be used. External cooling or tool cooling can be applied. Finally, tool designs which enables processing under smaller forces and consequently at lower heat input values can be selected [16].

To process high volume of materials, the dimensions of friction stir processing tool can be increased; however, capacity of friction stir processing equipment must be sufficient to resist and support forces needed for plunging and traversing. Other approach to increase processed volume is application of multiple passes. Since the process is not symmetrical, consideration should be given to direction of rotation. An advanced technology, Re-stir, is developed by TWI to eliminate asymmetry [22]. In this method, symmetry is acquired by changing rotational direction periodically. One multi-pass study done by J. Gandra et al. [23] examines the differences in overlapping by advancing side or by retreating side. They used 8 mm thick AA5083-H111 plates. Processed region is shown to be more uniform in thickness but with more irregular surface finish if overlapping is done by advancing side (Figure 11). Mechanical properties were also studied in their study. In Figure 12, maximum loads attained by samples are given. Overlapping by retreating side has been found to give better results.

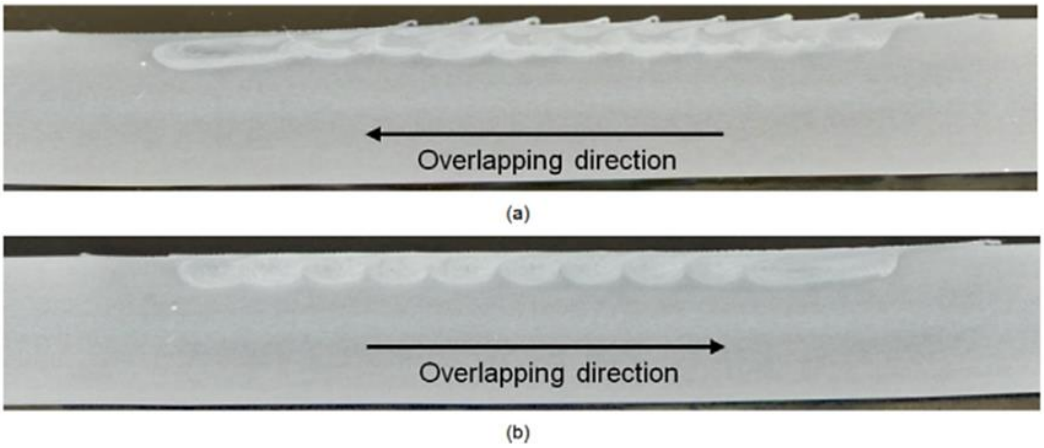

Figure 11. Macrographs of the cross-sections in friction stir processed surfaces when overlapping (a) by the advancing side, (b) by the retreating side [23].

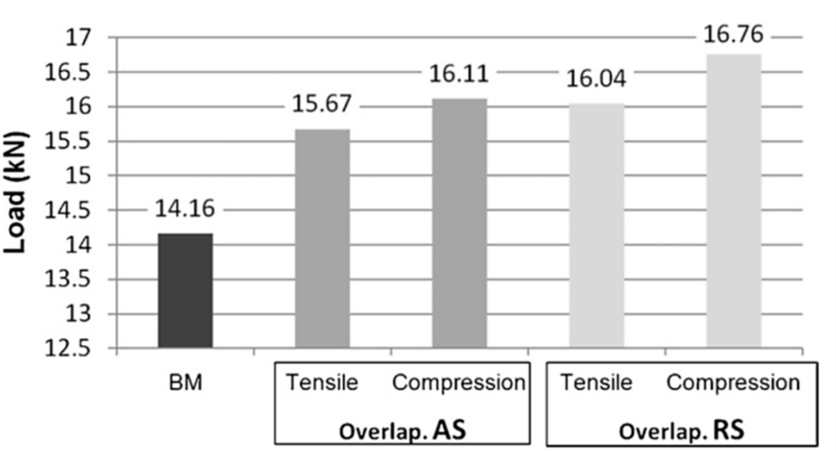

Figure 12. Maximum loads attained by as-processed samples during bending test relatively to the base material [23].

## 2.4. Fracture Mechanics; Fatigue Crack Growth

### 2.4.1. Fatigue

Fatigue of materials is time-dependent damage accumulation under cyclic stresses. It consists of two stages: crack initiation and crack growth. Under fluctuating loads, slip bands form locally due to local stress concentrations. Nucleation of micro-cracks at surface can be observed at a 45º angle to the loading axis as shown in Figure 13.

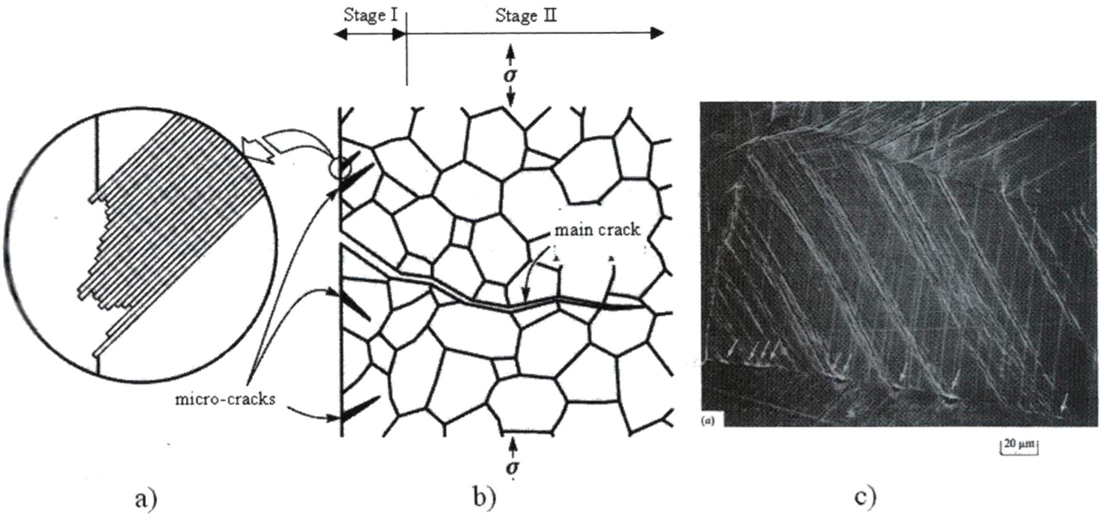

Figure 13. (a) Initiation of micro-cracks due to the sliding of alternate planes and to the formation of intrusions and extrusions at the frees surface (cross-section), (b) Formation of a main crack from micro-cracks, (c) Characteristic formation of stage 1 intrusions and extrusions at the surface of a fatigue specimen made of copper [24].

After micro-crack formation, cracks can grow or join into macro-cracks propagating perpendicular to principle loading axis. Catastrophic fracture occurs when the material cannot carry the load due to propagated fatigue crack. However, crack growth can be stopped by material barriers like grain boundaries. Facture surface at stable crack growth is usually seen as transgranular fracture (Figure 14).

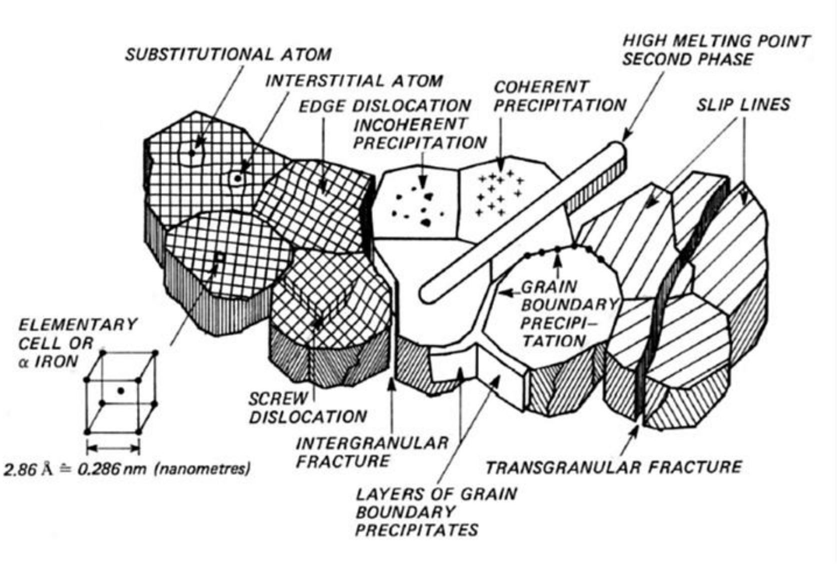

Figure 14. Micro structural features in metals [25].

In Figure 15, possible scenarios of fatigue crack growth are given. The dotted lines implies that crack growth is not always occur. The upper crack growth curve starts from a macro defect such as incomplete penetration found in weldments. The fatigue life of this crack can be monitored by non-destructive testing methods. The below two curves follows a micro crack for which the life of the component cannot be estimated by scheduled examinations.

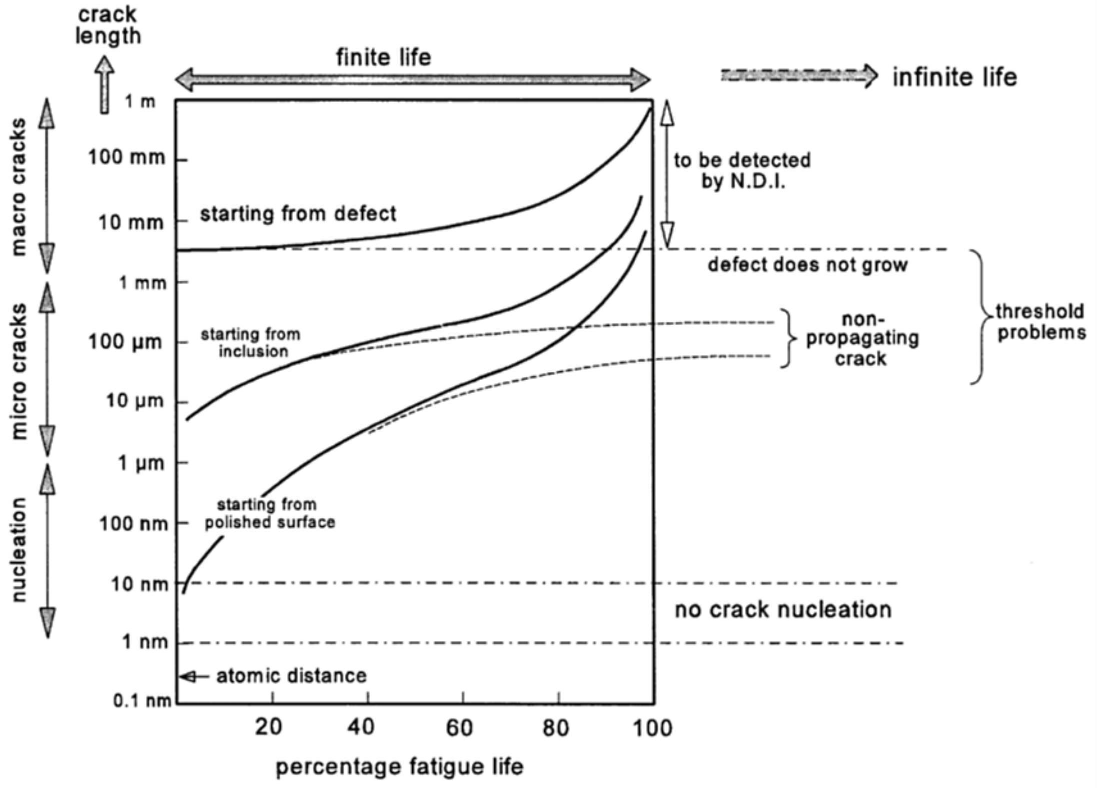

Figure 15. Different scenarios of fatigue crack growth [26].

### 2.4.2. Damage Tolerant Design

Structural designs can be done in infinite life, safe-life or damage tolerant design methodologies. For infinite life and safe-life approaches, S-N curves are used. S and N designates stress amplitude and number of cycles respectively. In Figure 16, results of fatigue tests conducted at different stress levels of a low-alloy steel are given. In infinite life approach, stress of the structural component is restricted under the fatigue limit (fatigue threshold or endurance limit) of the material. However, most materials do not show a fatigue limit and the stress level at for example $10^7$ is taken as its material strength. Safe-life design is done such that failure of a component is not expected within a pre-determined number of cycles. The component is removed when the calculated life is over regardless of its condition. This approach focuses crack initiation stage and it is more suitable for lower two fatigue curves shown in Figure 15.

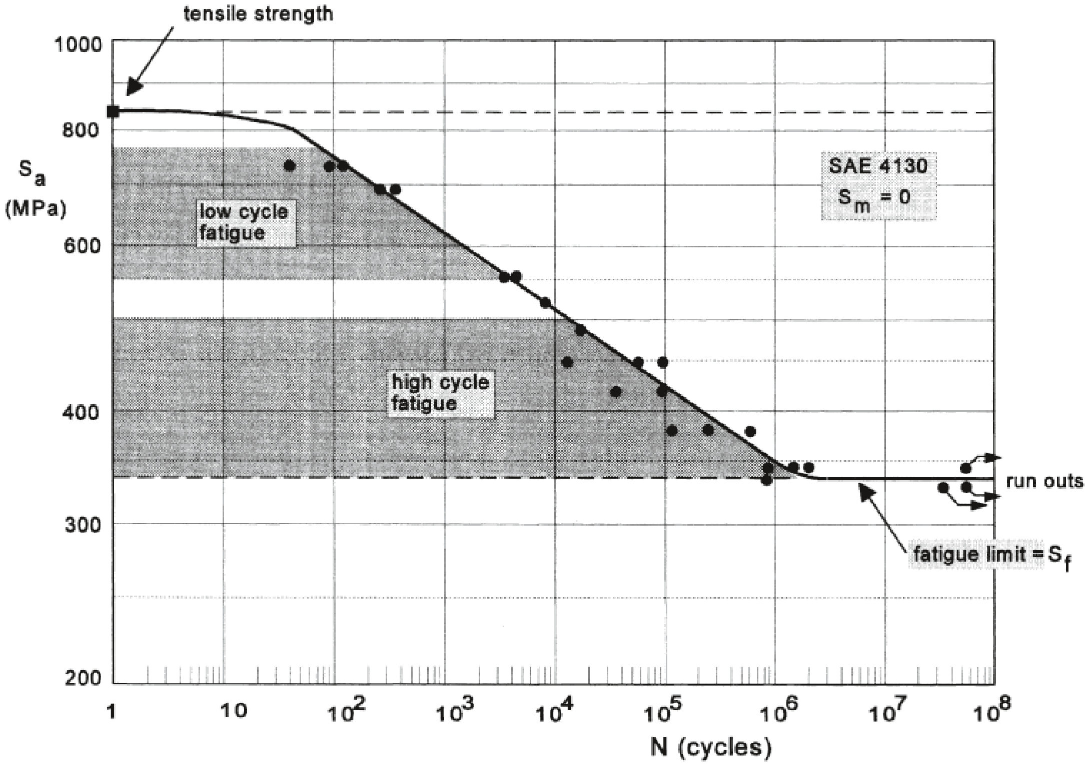

Figure 16. S-N of a low-alloy steel (R = -1) [26].

Damage tolerant design is usually preferred because stress concentration points like notches and scratches are commonly found on structures and cause fatigue cracks which decrease the fatigue threshold and total fatigue life. One method of damage tolerant design is to prevent instantaneous failure of a system, structural elements are designed such that the fracture of the component does not cause total system failure (fail-safe design). Second, structures are examined for any cracks periodically and crack growth behavior is examined. When the crack reaches the critical point, the component is removed from service.

Fusion weldments as briefly discussed in 2.3.3., generally contain flaws which can act as cracks. Consequently, fatigue crack growth rates are more critical than crack initiation for a joint. Damage tolerant design; therefore, is more suitable than safe-life approach which does not give information about propagation of cracks.

### 2.4.3. Fatigue Crack Growth

Macro cracks are shown to usually propagate normal to loading axis. In many situations, the type of force is tensile and called as mode 1 in literature. In Figure 17, three modes are shown. While the crack opening mode is shear in mode 2, the load is tearing in mode 3.

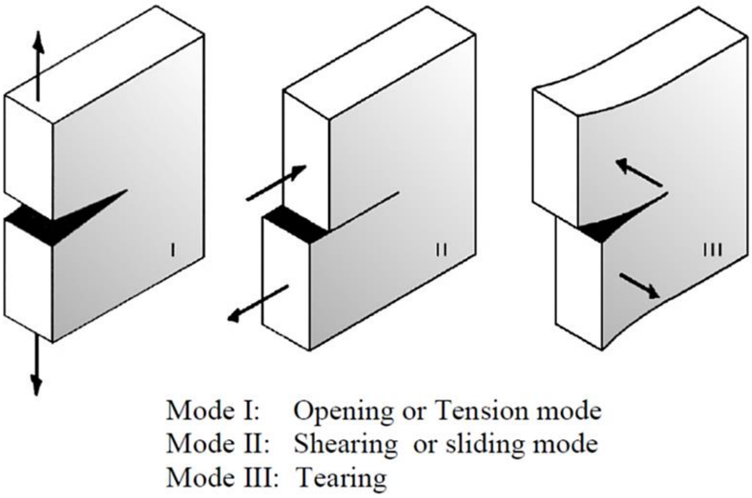

Figure 17. Different modes of crack surface displacements.

Cracks causes a local stress concentration near the crack tip. The stress field around the crack can be analyzed by stress intensity factor (K). This factor essentially has an elastic nature; however, it can be used where the plastic deformation is relatively small.

$$K = Y\sigma\sqrt{\pi a} \qquad \#1$$

σ is the applied stress (MPa),

Y is dimensionless parameter which depends on specimen geometry and crack length,

$a$ is the crack length (m).

Stress intensity factor is used to describe the crack growth resistance of a material, i.e. fracture toughness of a material. Since the amount of plastic deformation increases with decreasing thickness of specimen, thick samples must be prepared which ensure plane strain condition (Figure 18).

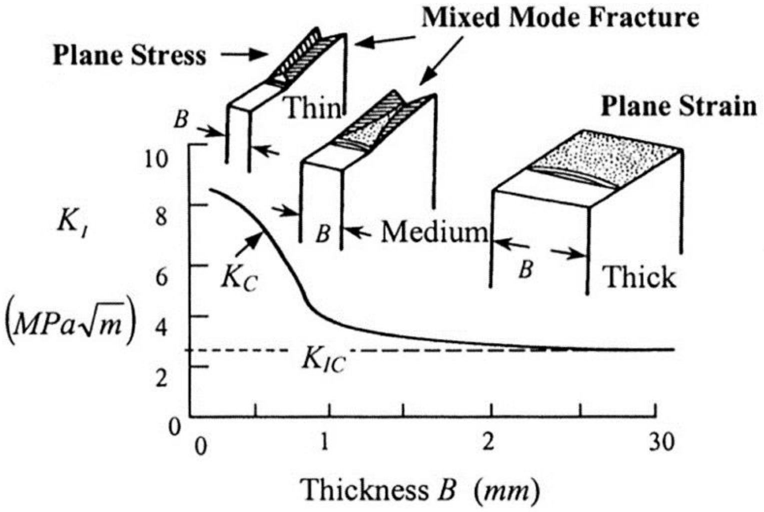

Figure 18. Effect of specimen thickness on fracture toughness [27].

Fatigue crack growth behavior of materials are also analyzed with stress intensity factor. Fatigue crack growth (da/dN) is known to depend on stress intensity factor range (ΔK) in a cycle and stress ratio (R). These parameters are explained in Figure 19.

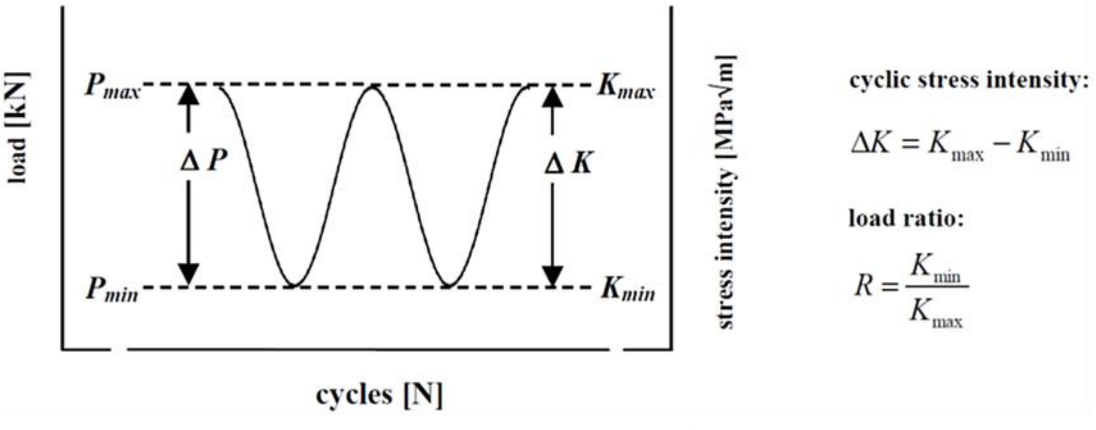

Figure 19. Mechanical parameters to describe the fatigue loading system [25].

One reason behind using stress intensity factor range (ΔK) for calculation of fatigue crack growth rate (da/dN) is that it gives the possibility to use dissimilar test parameters. For example, two test results of same material conducted at different stress amplitudes are given in Figure 20. Although the crack propagation rate at similar crack lengths is increases for higher stress, crack growth rate versus stress intensity factor range curves overlap.

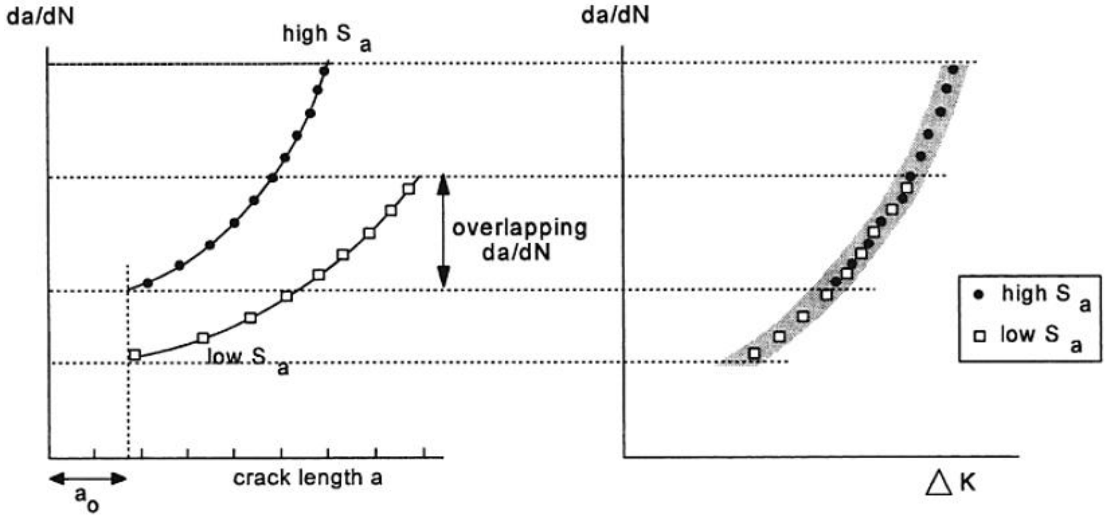

Figure 20. Fatigue crack growth curves ($S_a$= Stress amplitude) (a) da/dN – a, (b) da/dN – ΔK [26].

In Figure 21, a typical crack growth curve of a macro-crack is given. This curve can be divided into three parts. The second part is sometimes called Paris regime where a power law is applied. This law sometimes called Paris-Erdoğan law has been commonly used in fatigue crack closure analysis; however, it does not include the effect of stress ratio, R.

$$\text{Paris-Erdoğan Law: } \frac{da}{dN} = C\ (\Delta K)^m \qquad \#2$$

Where C and m are material constants dependent on the environment, test conditions, and material properties [28].

Taking logarithm of the law gives a linear equation:

$$\log\left({}^{da}/_{dN}\right) = \log C + m \times \log(\Delta K) \qquad \#3$$

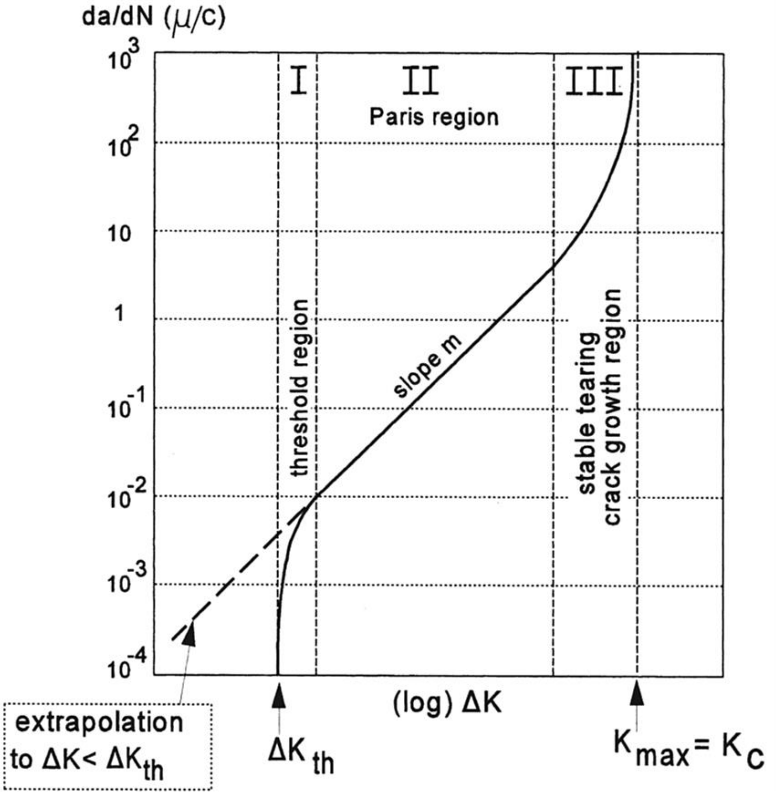

Figure 21. Three regions of the crack growth rate as a function of ΔK [26].

Two asymptotes in the crack growth curves represents fatigue crack growth threshold ($\Delta K_{th}$) and the fracture toughness of material if the test piece does not show excessive plastic deformation. $\Delta K_{th}$ defined as the minimum stress required for crack growth depends on the residual stresses and microstructure.

In Figure 22a, a macro-view of fractured fatigue specimen is given. Crack initiation points are shown with arrows. At the bottom region is the final-fracture zone. The final-fracture occurs at 45° where maximum shear stress is present. Beach marks which are characteristic features of fatigue are visible. These marks can be an indicative of different crack growth rates. Striations which are microscopic features of fatigue is shown in Figure 22b. In one beach mark, thousands of fatigue striations can be distinguished [29].

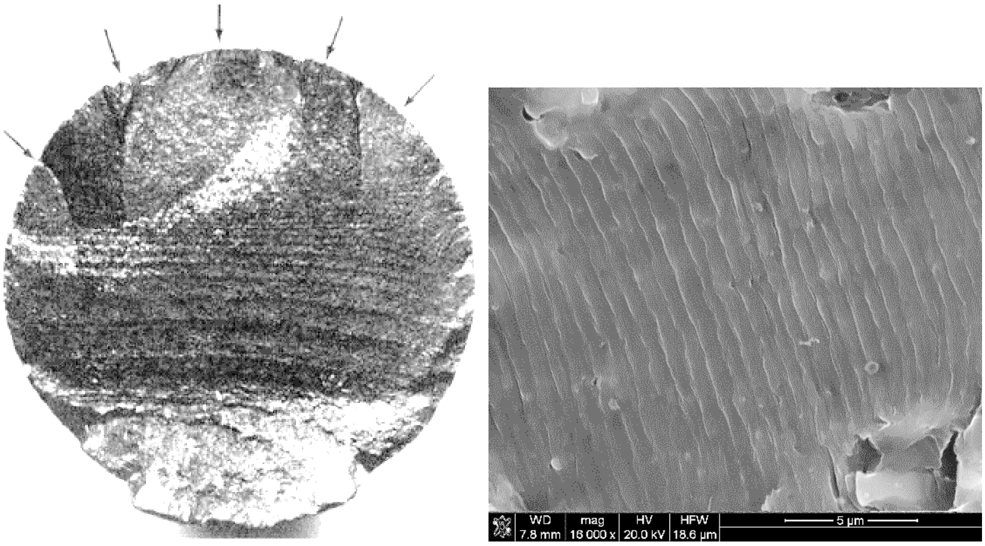

(a) (b)

Figure 22. (a) Fatigue fracture surface [30], (b) Striations.

One fatigue crack growth mechanism proposed by Laird is given in Figure 23. Propagation is said to occur due to two slip systems that are at the location of maximum shear stress (±45º to crack plane). During loading, plastic deformation occurs at the crack tip which causes crack growth. Although each striation has been thought to form during one cycle in some theories, there are other models in which the number of cycles per striation changes with stress intensity factor inversely [31].

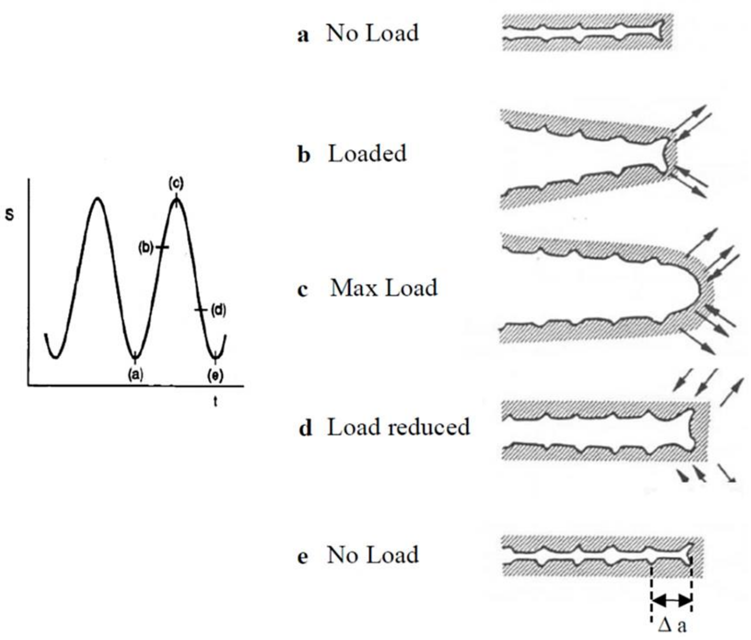

Figure 23. Fatigue crack growth mechanism [25].

Fatigue crack growth process can be affected by many factors. Several crack closure mechanisms have been postulated such as plasticity induced, roughness induced and crack-filling closure. Schematic drawings of some closure mechanisms are given in Figure 24. Plasticity induced crack closure is considered to be caused by plastic deformation at the crack tip. In some studies, retardation of fatigue crack growth rate has been explained by an overload causing plasticity-induced closure [32]. Roughness induced closure can occur due to mismatch between opposing crack surfaces. Microstructural heterogeneity in a material can deflect the crack path causing mix mode crack opening [31]. Several studies has shown that fine grain materials has higher fatigue crack growth rates compared to coarser grained materials [31-33]. One major crack-filling closure mechanism is oxidation of fatigue surfaces. Similarly viscous liquids can result in slower crack growth rates.

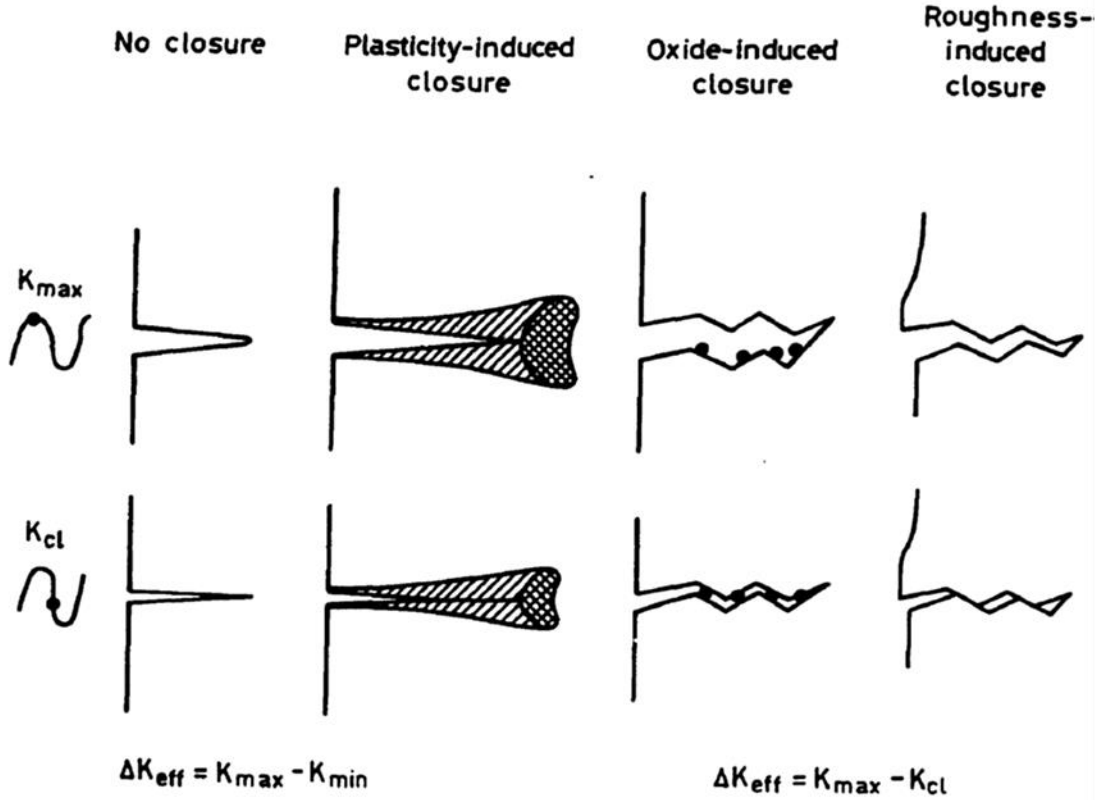

Figure 24. Schematic illustration of the main mechanisms of fatigue crack closure, after Suresh and Ritchie [32].

## 2.5. Previous Works

Friction stir technology has been investigated in many aspects such as microstructure, material flow, heat sources, temperature distributions, computer simulations, generated forces and mechanical properties. Review articles and books has started to be published in order to combine the knowledge. In this thesis, studies in which friction stir processing was applied in order to improve fusion weld properties are summarized.

### 2.5.1. Post-processing 6082 Weldments

Silva et al. studied the effect of friction stir processing on 6mm thick AA6082-T6 MIG welded (GMAW) plates. They observed that tensile strength and hardness of weld zone are not affected significantly by FSP. Since 6xxx series are heat-treatable alloys, the main strengthening mechanism is precipitation hardening and during fusion welding hardening precipitates dissolve decreasing mechanical strength and hardness. Therefore, hardness and tensile strength of as-welded plates and FSPed welds are inferior compared to base metal. On the other hand, fatigue tests demonstrated that fatigue life of MIG welds can be improved by FSP. They explained the increased fatigue strength by grain refinement, geometric modification and the removal of welding defects [35]. The authors also found similar results when FSPed T-joints [36].

### 2.5.2. Post-Processing 5083 Weldments

Fuller and Mahoney applied FSP on the surface 6mm 5083 H321 weldment three different way: weld toe by retreating side, weld toe by advancing side and weld crown. In Figure 25, macrographs showing different processing strategies are shown (Arc weld nugget is shown by (1), while base metal and FSP region are indicated by (2) and (3) respectively.).

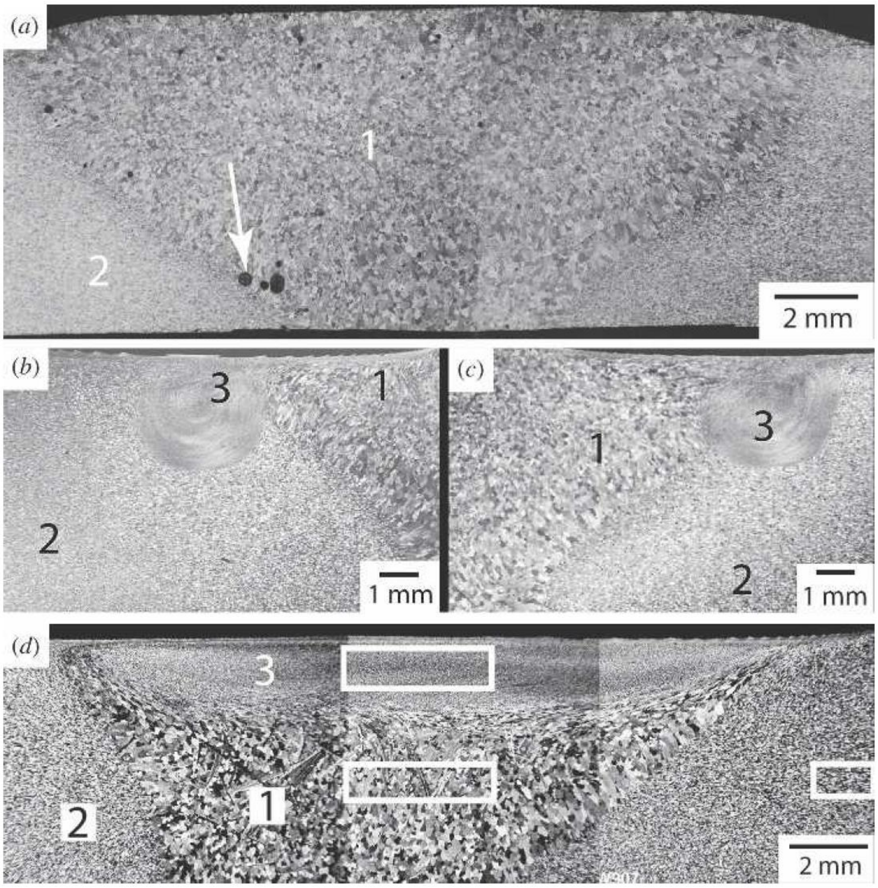

Figure 25. Light macrographs of 5083-H321 Al/5356 Al arc weld in the following conditions: (a) As-welded, (b) Weld toe FSP with arc weld nugget on advancing side, (c) Weld toe FSP with arc weld nugget on retreating side, (d) Weld crown FSP [37].

Microstructure analysis has showed presence of $Mg_2Si$ and $Al_6(Fe, Mn)$ particles. In the FSPed regions, the secondary particles were smaller indicating the fragmentation and spheroidizing due to FSP. Dislocation density in the arc weld nugget is low and occasional subgrain networks are present. Therefore, the weld nugget is same as an as-cast microstructure. Base metal has high dislocation density with them found primarily as subgrain structures. FSPed regions has recrystallized microstructure such that grains have either high or low density of dislocations.

FSP improved local tensile properties (yield strength, tensile strength, and elongation) of as-weld by grain refinement, porosity healing, precipitate and solid solution strengthening. Fatigue resistance of weld metal also increased by FSP. Discontinuities that become crack initiation sites are removed by FSP forming a fine-grain layer [37].

One other study about FSP of weld toe is done by Borrego et al. Although the hardness of FSPed region is higher than as-weld and base metal, effect of friction stir processing on tensile properties were found to be negligible. Improvement of hardness has been attributed to the plastic deformation induced by the friction stir processing because base metal is a strain hardened alloy. Similar to the study of Muller et al., post-processing increased the fatigue strength. Grain refinement, elimination of welding defects (namely porosity and lack of wetting) and geometry modification [38].

### 2.5.3. Pre-Processing Nickel-based Alloy Weldments

Rule et al examined the effect of FSP pretreatment on grain size and liquation cracking susceptibility of 6.3 mm thick nickel-based alloy weldments. Grain size of both weld metal and HAZ decreased by application of FSP prior to gas tungsten arc welding (GTAW). Refinement of weld metal grain size is attributed to the smaller grains along the fusion boundary increasing nucleation sites. Particle size of NbC has not changed by FSP implying no fragmentation occurred due to stirring.

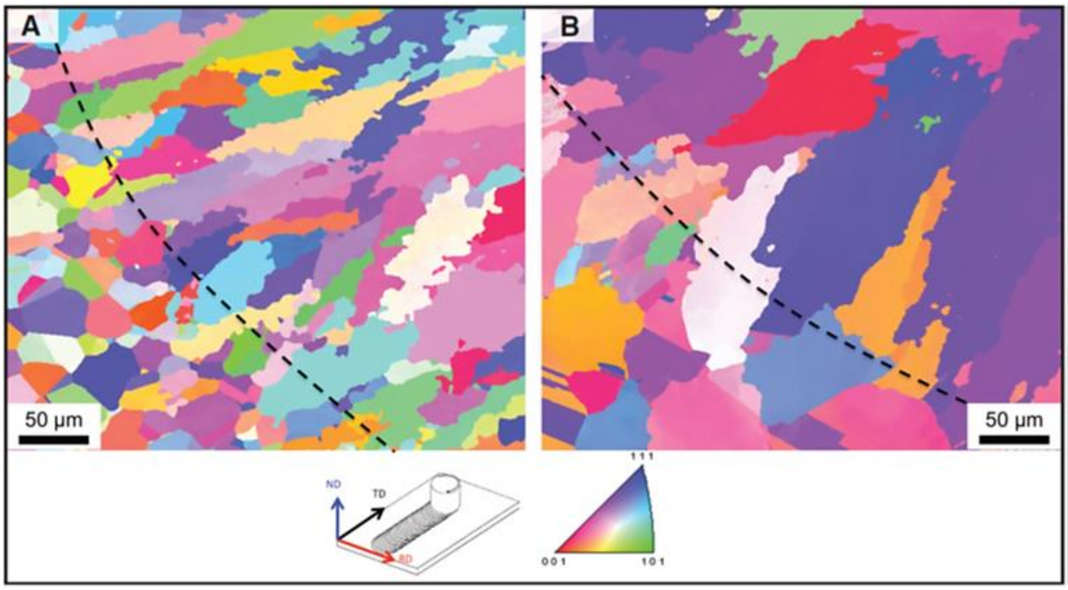

Figure 26. Inverse pole figure maps along the fusion boundary
(a) FSP pretreated; (b) untreated.

Effect of heat input during GTAW is shown in Figure 27. Although the grain size in the HAZ of untreated weldments increases with the heat input, the grain size of FSP pretreated HAZ is smaller than untreated welds.

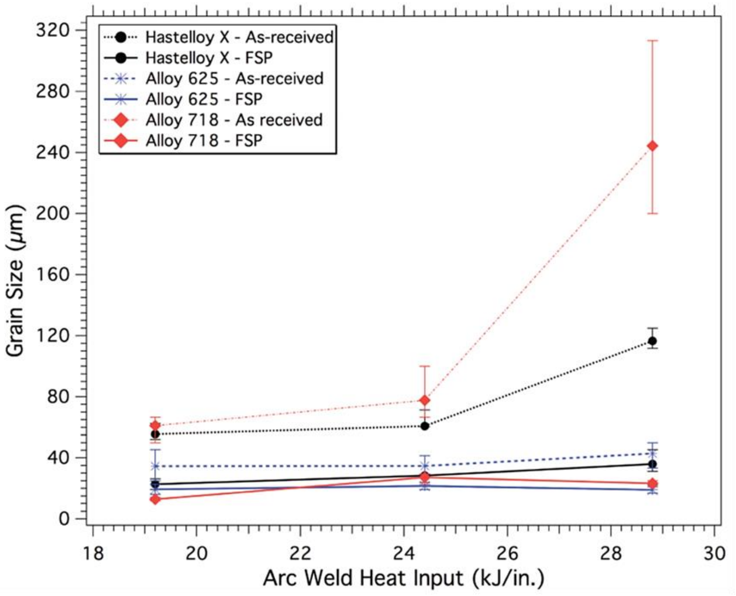

Figure 27. Arc weld HAZ grain size response to heat input.

HAZ liquation cracking susceptibility was reduced by FSP pretreatment. Varestraint vest was done and crack lengths were measured. Although total crack length was not always smaller for pretreated welds, maximum crack length of untreated welds was higher compared to FSP pretreated HAZ depending on the alloy composition. [39]

### 2.5.4. Effect of FSP on Residual Stress Levels of 6082 and 5083 Weldments

Nobre et al. examined the effect of FSP on residual stress levels on 6 mm AA6082-T651 and AA5083-H111 fillet welds (T-joints). Contradicting results were found for different materials.  Residual stress of 5083 welds increased by FSP; whereas, stress relaxation occurred in FSPed 6082 welds. They also investigated the residual stress after 10000 loading cycles. Residual stress relaxation was observed especially in as-weld 6082. They concluded that residual stress has minor effect on the final mean stress and improvement of fatigue strength by FSP cannot be explained by residual stresses [40].

# CHAPTER 3

# EXPERIMENTAL

## 3.1. General

In the experiments, the procedure given in Figure 28 was followed. Characterization methods and the related equipment are given in Figure 29.

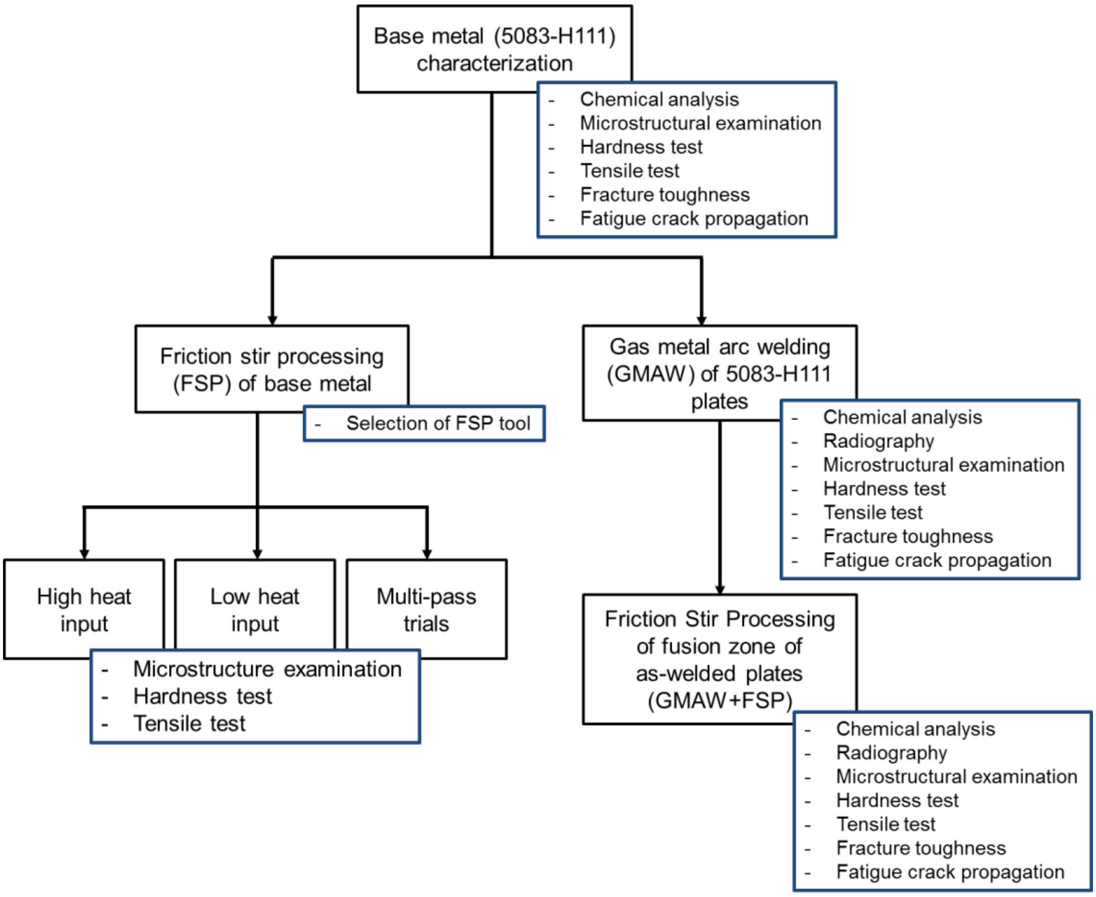

Figure 28. Flow chart of the experiments.

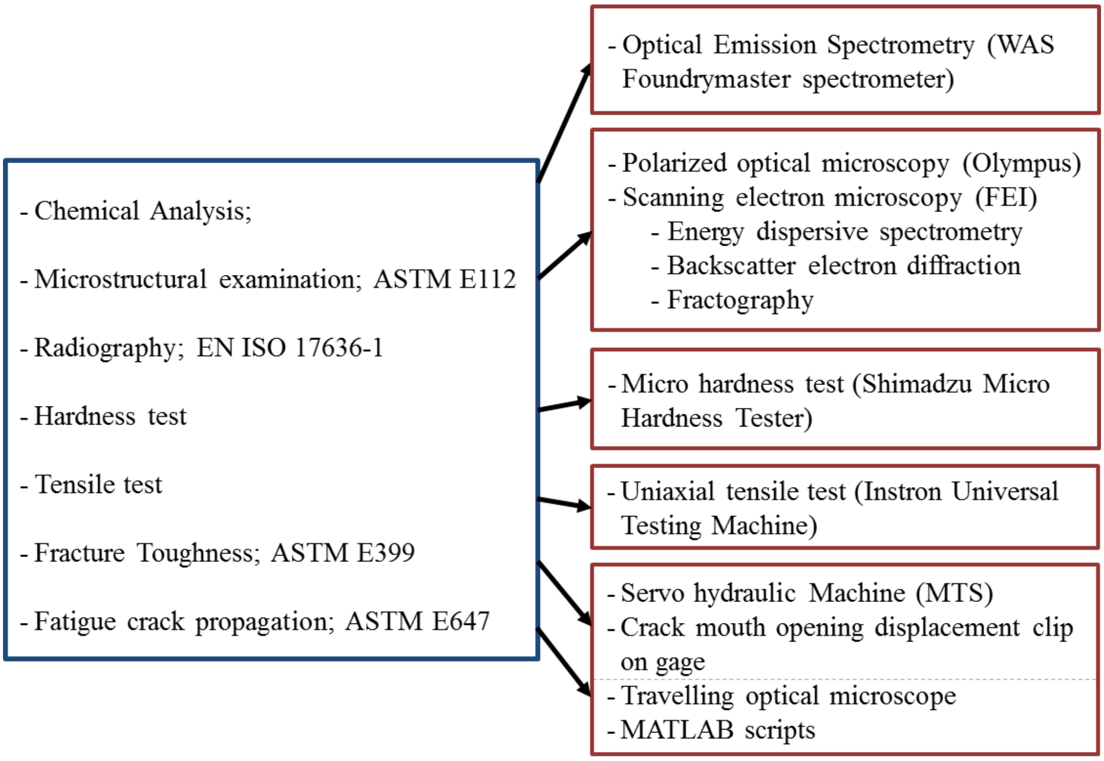

Figure 29. Characterization methods and the equipment used in experiments.

### 3.2. Base and Weld Metal

5083 H111 aluminum plates (300 mm x 150 mm x 20 mm) were used. H111 designates that they are work-hardened less than the amount required for a controlled H11 temper (1/8 hard). Yield strength and % elongation of the base material were found to be 203±14 MPa and 17±1% for the transverse direction.

WAS Foundrymaster spectrometer was employed for chemical analysis. The chemical constituents of the base and weld metal are tabulated in Table 5 and Table 6 respectively. Chemical analysis of weld metal was done after machining of weld cap, grinding with 320 grid abrasive paper and etching by Flick’s reagent. The surface of the base metal sample was ground by 400 grid paper before chemical analysis. Results of optic emission spectroscopy are in acceptable levels according to ASTM B209 and AWS A5.10 for base metal and weld metal, respectively.

Table 5. Chemical analysis of base metal.

| **5083 H111** | **Si** | **Fe** | **Cu** | **Mn** |
|---|---|---|---|---|
| Experimental | 0,17±0,05 | 0,4±0,1 | 0,04±0,001 | 0,56±0,01 |
| Standard | 0,4 max | 0,4 max | 0,1 max | 0,4-1 |
| | **Mg** | **Zn** | **Cr** | **Ti** |
| Experimental | 4,79±0,06 | 0,04±0,01 | 0,09±0,002 | 0,05±0,001 |
| Standard | 4-4,9 | 0,25 max | 0,05-0,25 | 0,15 max |

Table 6. Chemical analysis of weld metal.

| **AWS A5.10 ER5356** | **Si** | **Fe** | **Cu** | **Mn** | **Be** |
|---|---|---|---|---|---|
| Experimental | 0,08±0,01 | 0,15±0,01 | 0,01±0,001 | 0,2±0,01 | <0,0002 |
| Standard | 0,25* | 0,4* | 0,1* | 0,05-0,2 | 0,0003* |
| | **Mg** | **Zn** | **Cr** | **Ti** | |
| Experimental | 4,79±0,17 | <0,0050 | 0,07±0,002 | 0,08±0,001 | |
| Standard | 4,5-5,5 | 0,1* | 0,05-0,2 | 0,06-0,2 | |

*maximum amount

### 3.3. Gas Metal Arc Welding

The plates were gas metal arc welded along the rolling direction. AWS A5.10 ER5356 rod with a diameter of 1.2 mm was used as the filler material. Shielding gas was welding-grade argon having minimum purity of 99.998%. After a preliminary work, the weld bevel is decided to be double-V groove. Beveled plates were butt welded at the flat position as seen in Figure 30. The welding parameters are listed in Table 7.

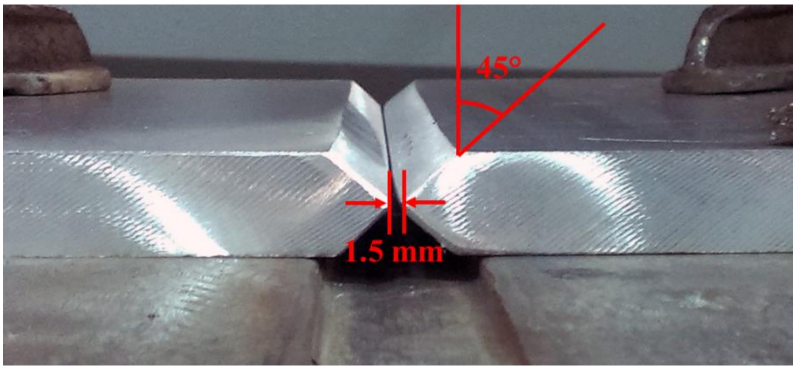

Figure 30. Groove geometry.

Table 7. Process parameters of GMAW

| | **Wire Feed Rate (m/min)** | **Arc Voltage (V)** | **Welding Current* (A)** | **Linear Welding Speed* (mm/s)** | **Gas Flow Rate (lt/min)** | **Heat Input* (kJ/mm)** |
|---|---|---|---|---|---|---|
| **Root pass** | 10.5 | 22.5 | 170 | 5.3 | 18 | 0.5 |
| **Filler passes** | 12 | 25 | 185 | 5.7 | 18 | 0.6 |

*Average value

### 3.4. Radiographic Testing

FSPed plates, as-welded plates and FSPed weldments were radiographically inspected. Tests were performed according to EN ISO 17636-1/2013 [43]. X-ray unit Eresco (200 kV) was employed for radiography. D4 type films were used. 80 kV and 4.6 mA were applied for 80 seconds. Density of the radiographs was in the range of 1.50-2.00.

Results of the radiographical inspection of as-welded plates were used to select defectless samples for tensile testing and also for friction stir processing. Tensile test specimens were cut from plates which are free from macro porosity and lack of penetration (Figure 31).

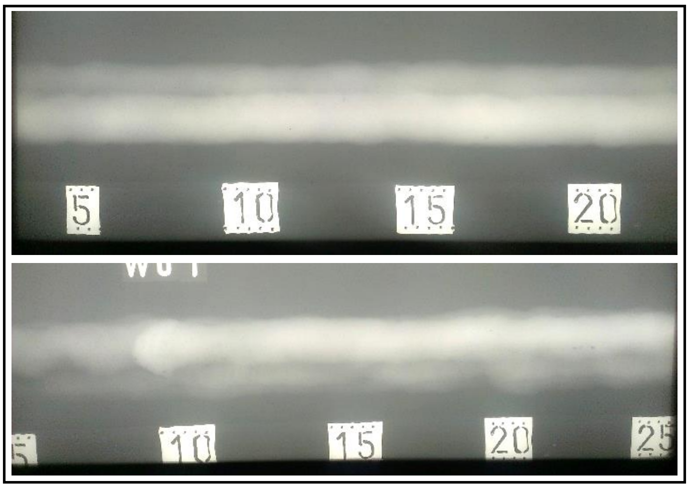

Figure 31. Radiographs of the as-welded plates used for tensile testing.

The radiographs of as-welded plates and friction stir processed plates are shown in Figure 32 and Figure 33. In Figure 32, high amount of macro porosity can be observed in as-welded condition. Another defective as-welded plate is given in Figure 33. It does not have macro porosity; however, lack of penetration is detected. Friction stir processing both plates seems to close defects found in as-welded condition. Nevertheless, short tunnels formed during FSP are seen as black lines at the end of passes. Other indications on the radiographic images are typical discontinuities, which occurs at the start and the end of the process. The dark circles seen on the radiographs are at the zones where FSP was stopped, the tool was taken out from the plate. Start point of FSP is perceived as dark circles surrounded by lighter color.

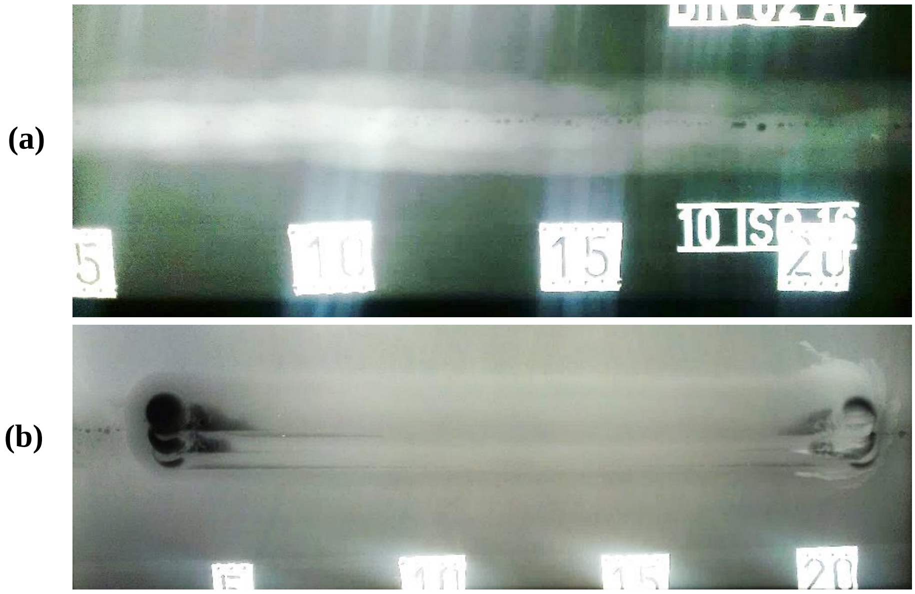

Figure 32. Radiographs of (a) as-welded plate with porosities, (b) after FSP.

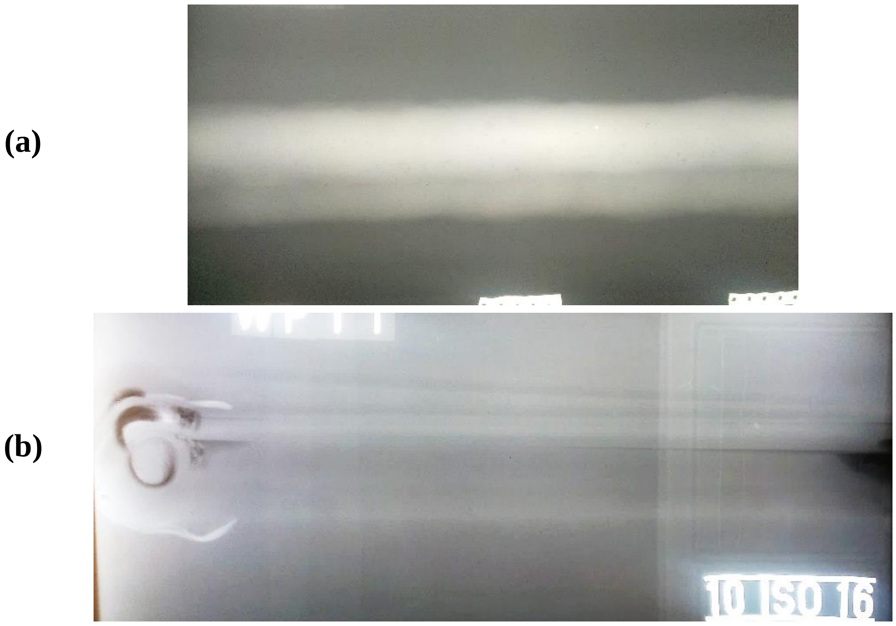

Figure 33. Radiographs of (a) as-welded plate with lack of penetration, (b) after FSP.

### 3.5. Friction Stir Processing

Three types of tools were tried in optimization of friction stir processing (see Chapter 4). Then, “triflat” tool was decided to be the best choice. It has a scroll shoulder that has a diameter of 20 mm. Pin of the tool has a length of 9 mm and upper diameter of 9 mm. It is treaded and has 3 flat sides (Figure 34).

Figure 34. “Triflat” tool for FSP.

Six series of samples were prepared:

1) Single pass 720 rpm, 100 mm/min.
2) Single pass 210 rpm, 185 mm/min.
3) Multi-pass 720 rpm, 100 mm/min.
4) Multi-pass 290 rpm, 185 mm/min.
5) Multi-pass 290 rpm, 100 mm/min.
6) Friction stir processing of weld metal: 290 rpm, 100 mm/min.

Multi-pass FSP were done in 5 passes in both sides as trial before processing as-welded plates. Friction stir processing of weld metal was done in total of 6 passes. (Figure 35). Surface of plates were machined before FSP to obtain flat surface free from weld cap. In each side, three passes were applied by providing overlaps such that retreating side of one pass was on the advancing side of previous pass.

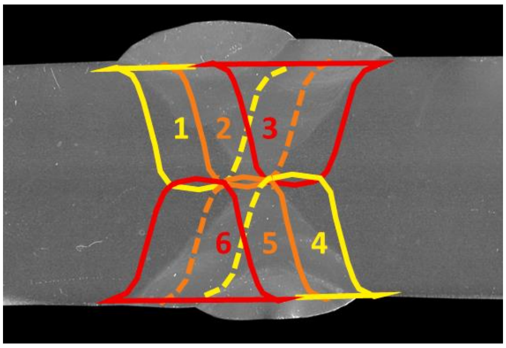

Figure 35. Configuration for the friction stir processing of the as-welded plate.

In the first trials, temperature was measured for three passes. For each pass, four K-type thermocouples were placed in the holes drilled on the plate (Figure 36).

Thermocouples were connected to SCXI-1112 module of National Instruments. A block diagram was written in LabView. Data reading was set to 20 Hz.

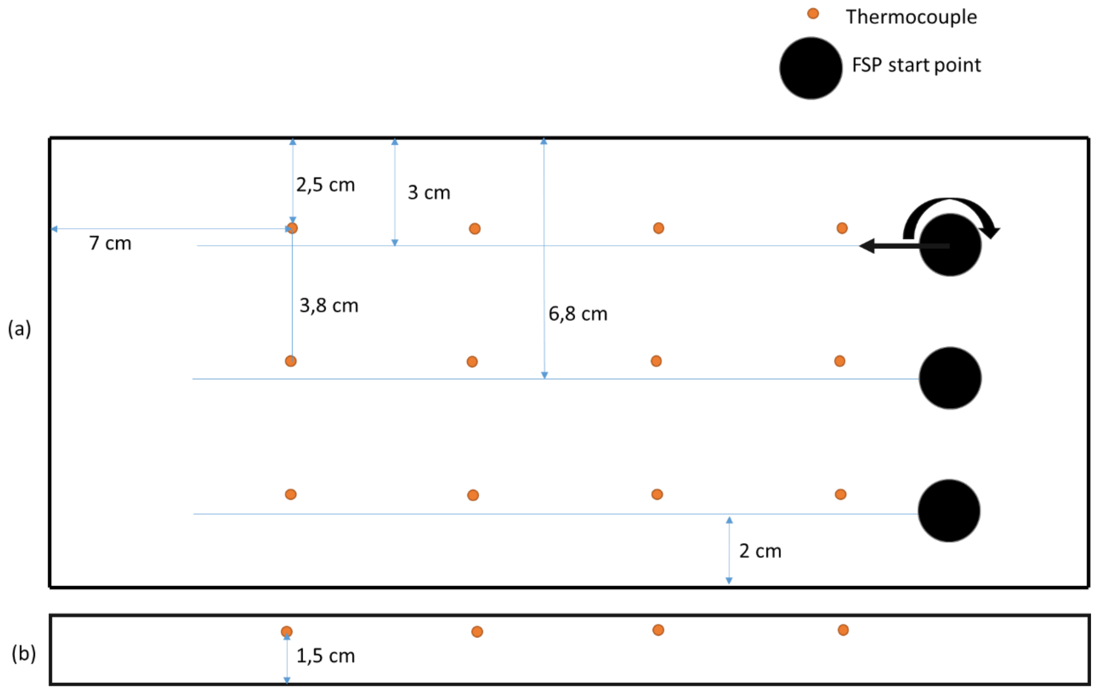

Figure 36. Positions of the thermocouples. (a) Top view, (b) Side view.

### 3.6. Microstructural Examination and Analyses

For metallographic analyses, specimen surface was ground with 80, 400, 800, 2000 abrasive papers. After grinding, cloth polishing was done with 3 μm and 1 μm diamond suspension. Colloidal silica was used for final polishing. For optical inspection, specimens were etched for 1.5 minutes with modified Barker's solution (195 ml $H_2O$ + 5 ml $HB_4F$ + 5 ml $H_2O_2$). Etching voltage was set to 20 Volt. For backscatter electron diffraction (EBSD), polished specimen surface was electropolished with 5% perchloric acid + 95% ethanol.

FEI brand scanning electron microscope (SEM) was used for elemental analysis of precipitates by energy-dispersive X-ray spectroscopy (EDS), backscatter electron diffraction (EBSD) and fractography. As-polished samples were used for EDS and EBSD analyses.

Two different methods were used for grain size measurements. Firstly, optical grain size measurement was done on images of etched samples obtained by polarized optical microscope. Linear intercept method was applied according to ASTM E112. The other method was backscatter electron diffraction. This technique was resorted for friction stir processed samples for which grain size measurement is difficult due to 0-5 μm grain diameter.

Area fractions of precipitates were calculated with an image analysis software, Clemex. After final polishing, 5 to 10 images from each sample were taken by optical microscope.

## 3.7. Mechanical Tests

### 3.7.1. Hardness Test

Hardness tests were done with HMV2 Shimadzu Micro Hardness Tester. 19.614 N load was applied for 10 seconds for each indentation.

### 3.7.2. Tensile Test

For tensile testing of the multi-pass FSPed base metal, two to three samples were prepared perpendicular to the FSP direction.  The geometry of specimens is shown in Figure 37.

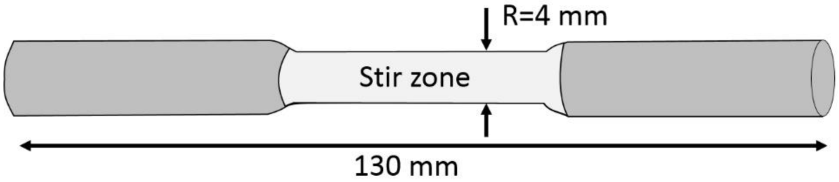

Figure 37. Tensile test specimen of the FSPed base metal.

For tensile testing of the base metal and weldments, two types of tensile specimens were prepared as shown in Figure 38. As-welded and FSPed samples were prepared perpendicular to welding direction. Base metal specimens were cut perpendicular to the rolling direction which is same as the welding direction. 5 specimens were prepared as Type I and 2 specimens were prepared as Type II.

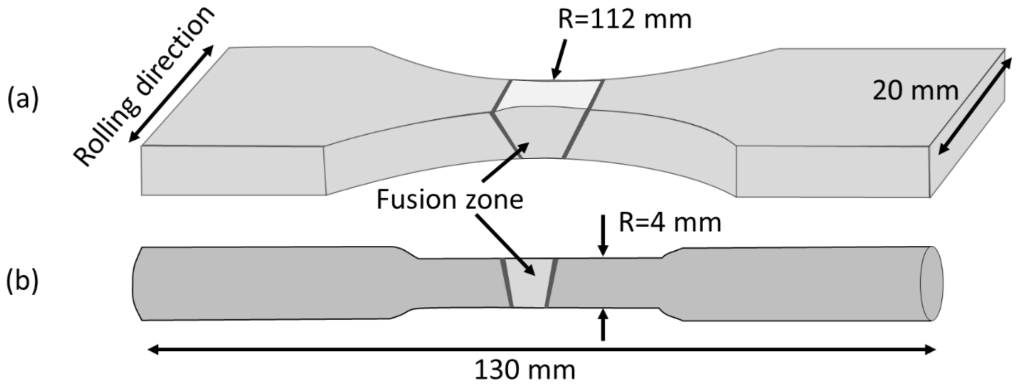

Figure 38. Tensile test specimens (a) Type I, (b) Type II.

Tensile specimens of Type II were used to determine the weakest point of the weldment. Since as-welded and FSPed specimens fractured at their fusion lines and un-processed base metal respectively, the Type I specimens were used to measure tensile strength.

### 3.7.3. Fracture Toughness

Compact tension specimens were prepared for fracture toughness test (Figure 39). MTS servo-hydraulic machine with a capacity of 100 kN equipped with Instron 8500 was employed at room temperature. Fatigue precracking was conducted at maximum loads at 4000 N and 3000 N with the stress ratio (R) of 0.1 for initial part and final stage respectively, so that $K_{max}$ did not exceed 80% and 60% of the estimated value of $K_{Ic}$ of the materials. Precrack size was kept between 0.45 and 0.55 times the width.

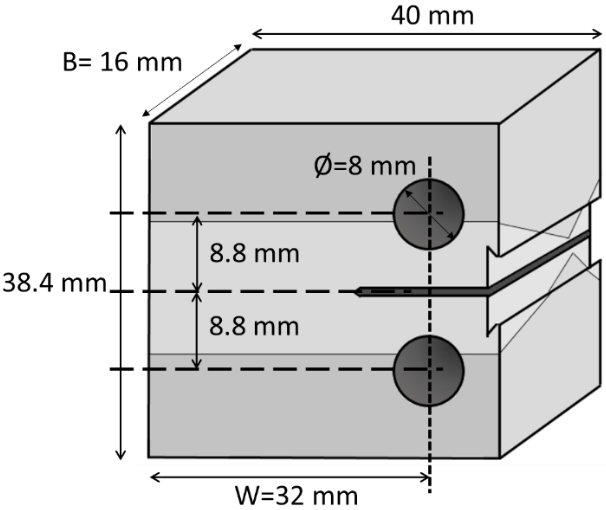

Figure 39. Fracture toughness test specimen.

Force versus crack mouth opening displacement curves were obtained digitally. The $P_{max}/P_Q$ ratio of the specimens were higher than 1.10. Thus, $K_{Ic}$ tests were found to be invalid according to ASTM E399 Section 9.1.3. $K_Q$, conditional results, were calculated by using Equation 4.

$$K_Q = \frac{P_Q}{\sqrt{BB_N W}} f\left(\frac{a}{W}\right) \qquad \#4$$

Where $f\left(\frac{a}{W}\right) = \frac{\left(2+\frac{a}{W}\right)\left[0.886+4.64\frac{a}{W}-13.32\left(\frac{a}{W}\right)^2+14.72\left(\frac{a}{W}\right)^3-5.6\left(\frac{a}{W}\right)^4\right]}{\left(1-\frac{a}{W}\right)^{3/2}}$

$P_Q$ = force determined according to ASTM E399 Section 9.1.1. (N),
B = specimen thickness (m),
$B_N$ = specimen thickness between the roots of the side grooves (m),
W = specimen width (depth) (m),
a = crack size determined according to ASTM E399 Section 8.2.3. (m).

### 3.7.4. Fatigue Crack Propagation

Fatigue crack propagation tests were carried out at room temperature. Dimensions of the compact-tension specimens are given in Figure 40. For each zone, 3-4 specimens were cut such that notch was parallel to rolling direction for base material and to welding/processing direction for as-welded materials and FSPed weldments. Electric discharge machining was used for preparation of the specimens.

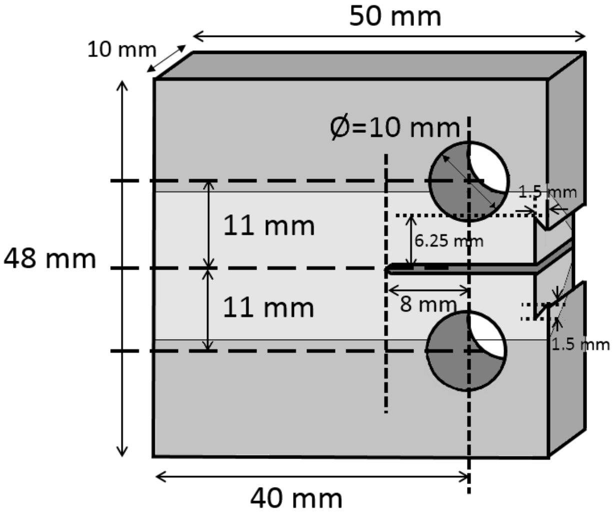

Figure 40. Geometry of compact tension specimens [46].

The constant-force-amplitude test procedure was applied for the stress ratio of 0.1. Loading was sinusoidal with 10 Hz frequency. Maximum load applied for the pre-crack stage was in the range of 4400 N to 4600 N. Crack propagations were done under the mean load of 1815 N with an amplitude of 1485 for the base metal and the FSPed weld metal. Sinusoidal load applied for crack propagation in the weld metal was 2035±1665 N.

Crack size (a) measurements were done with the travelling optical microscope having a resolution of $9.12 \times 10^{-3}$ mm. Crack mouth opening displacement (CMOD) was also measured by clip-on gage.

Three MATLAB scripts were written to evaluate fatigue crack growth test data. One script was used to convert CMOD data to crack size. Second script was used to calculate the stress intensity and the crack growth rate following incremental polynomial method. Final script was used for determination of the coefficients of the Paris-Erdoğan law.

First program finds slope of the P versus $V_m$ graph for each cycle; then, it converts the calculated slope into crack size by Equation 1 taken (ASTM E399). Elastic constraint modulus was chosen between 60 to 70 GPa to be in agreement with the optically calculated crack size.

$$a = w(1000 - 4500U + 13157U^2 - 172551U^3 + 879944U^4 - 1514671U^5) \quad \#5$$

where $U = \frac{1}{1+\sqrt{\frac{E' B_e V_m}{P}}}$

$V_m$= crack mouth opening displacement, (m),
P= applied force, (N),
$B_e$= $(B-B_N)^2/B$,
$E^{'}$=elastic constraint modulus (Pa) (E for plane stress; $E/(1-\nu^2)$ for plain strain)
ν= Poisson’s ratio

After obtaining crack size from CMOD data, an elimination procedure was applied based on the average value of neighboring data. First, average of 41 crack size values was calculated. If 21th crack size that differs 0.0005 mm from the average, it was not considered for further calculations. This process was done for each cycle except the first 20 and the last 20 data.

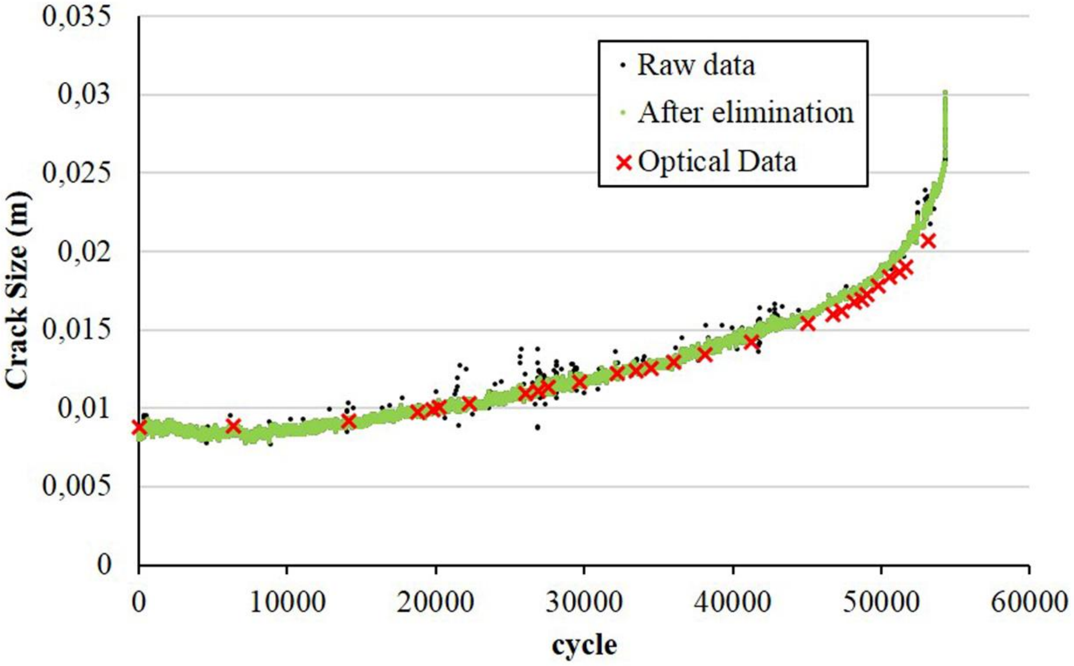

Figure 41. Crack size data obtained from CMOD

Second script was written to obtain fatigue crack growth rate (da/dN) versus stress-intensity factor range (ΔK) graphs for both CMOD data and optical data. ASTM 647 incremental polynomial method was followed. A second order polynomial was fitted to sets of (2n+1) successive data points such that for $i^{th}$ data point, n neighboring data points before and after the data point with itself are counted if applicable. While n=3 was selected for optical data, n=500 was used for CMOD data. Crack growth rate was calculated from the derivative of polynomial fitted to each data point. Stress-intensity factor ranges (ΔK) for the corresponding data point was computed with the fitted crack size using Equation 2.

$$\Delta \mathrm{K} = \frac{\Delta \mathrm{P}}{B\sqrt{W}} \frac{(2+\alpha)}{(1-\alpha)^{\frac{3}{2}}} (0.886 + 4.64\alpha - 13.32\alpha^2 + 14.72\alpha^3 - 5.6\alpha^4) \qquad \#6$$

where $\alpha = a/W$, and this expression is valid for $a/W \geq 0.2$.

The coefficients of the Paris-Erdoğan equation were calculated by fitting best line to the steady state of log(da/dN) vs log(ΔK).

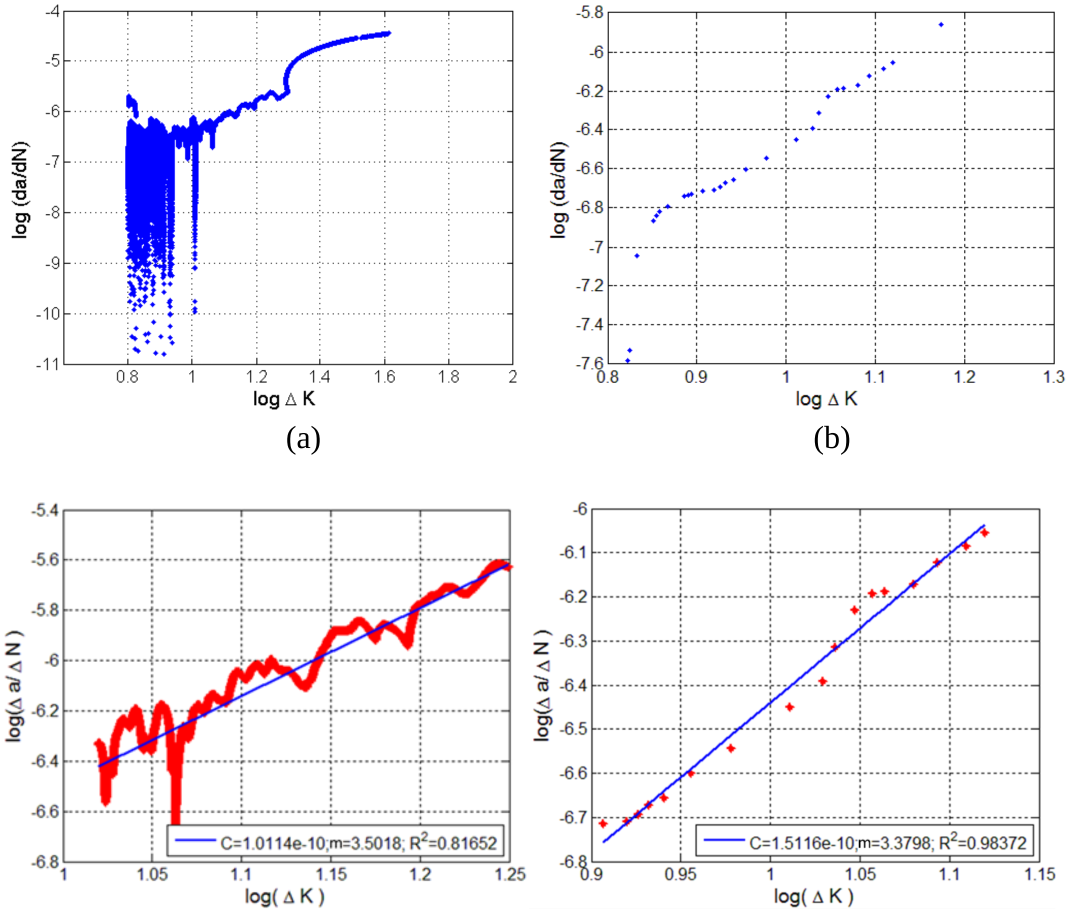

(a) (b)

(c) (d)

Figure 42. log (da/dK) versus log (ΔK) graphs for a base metal sample (a) Full range CMOD data, (b) Full range optical data, (c) Steady stage best fit line of CMOD data, (d) Steady stage best fit line of optical data.

# CHAPTER 4

# RESULTS

## 4.1. Optimization of Friction Stir Processing

### 4.1.1. Tool A01

The first tool A01 was made of H13 steel (Figure 43). Hardness of the tool after was measured as 493 HV2 (≈49 HRC).

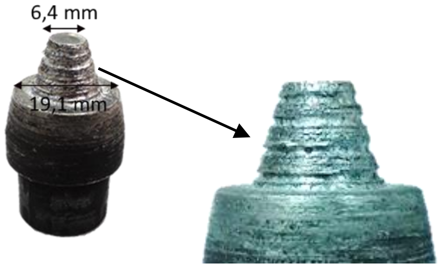

Figure 43: Photos of tool A01.

The plates were FSPed parallel to the rolling direction. 3 passes were done on one plate as shown in Figure 36. Variable process parameters were rotational speed, travel speed, angle of the tool to travel direction, x, and angle of the tool to perpendicular to travel direction, y. Parameter sets tested with A01 tool are listed in Table 8. No backing plate was used.

Table 8. Process parameters of trials with A01 tool.

| | **Rotation speed (rpm)** | **Travel speed (mm/min.)** | **x°** | **y°** |
|---|---|---|---|---|
| **DN1** | 900 | 21 | - | - |
| **DN2** | 900 | 21 | 2 | - |
| **DN3** | 900 | 21 | 2 | 2 |
| **DN4** | 1120 | 17 | -2 | -2 |
| **DN5** | 1400 | 17 | 2 | 2 |
| **DN6** | 560 | 17 | 2 | 2 |
| **DN7** | 560 | 21 | 2 | 2 |
| **DN8** | 560 | 27 | 2 | 2 |
| **DN9** | 355 | 43 | 2 | -2 |
| **DN10** | 355 | 68 | 2 | -3 |
| **DN11** | 355 | 21 | 2 | 2 |
| **DN12** | 355 | 43 | 2 | -3 |
| **DN13** | 224 | 43 | 2 | -2 |

Temperature measurements were conducted by four thermocouples for every trial. Average of the readings is given in Figure 44. Temperature of the plate is seen to get lower with each trial.  The time period at high temperature also gets shorter for successive trials.

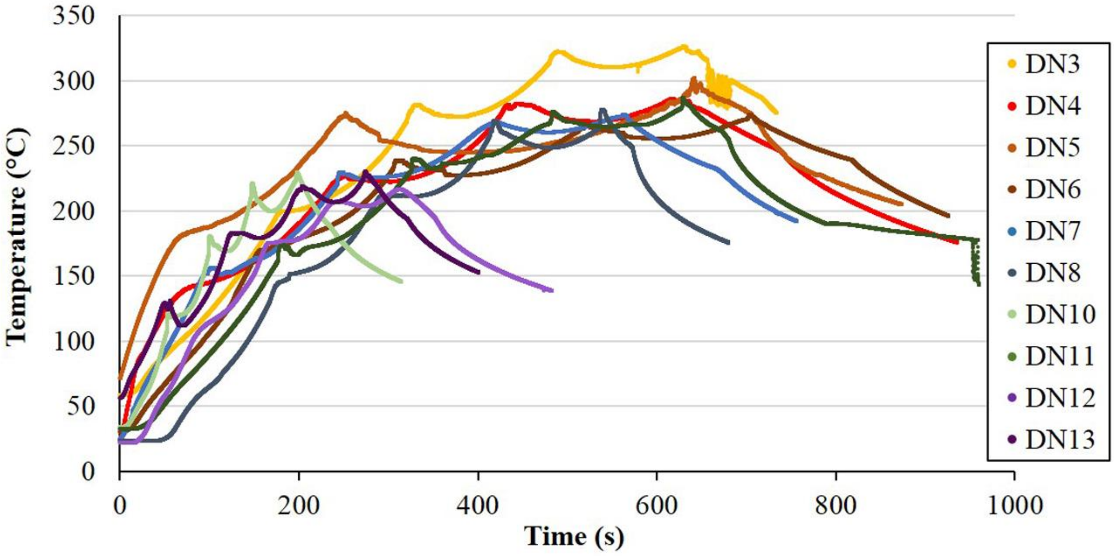

Figure 44. Results of the temperature measurements (average of 4 thermocouples).

Macro inspection of six passes was done to samples sectioned perpendicular to travel direction. Radiographic test of plates were also done (Figure 45). Although all passes had defects, the volume of defects formed by friction stir processing were decreased.

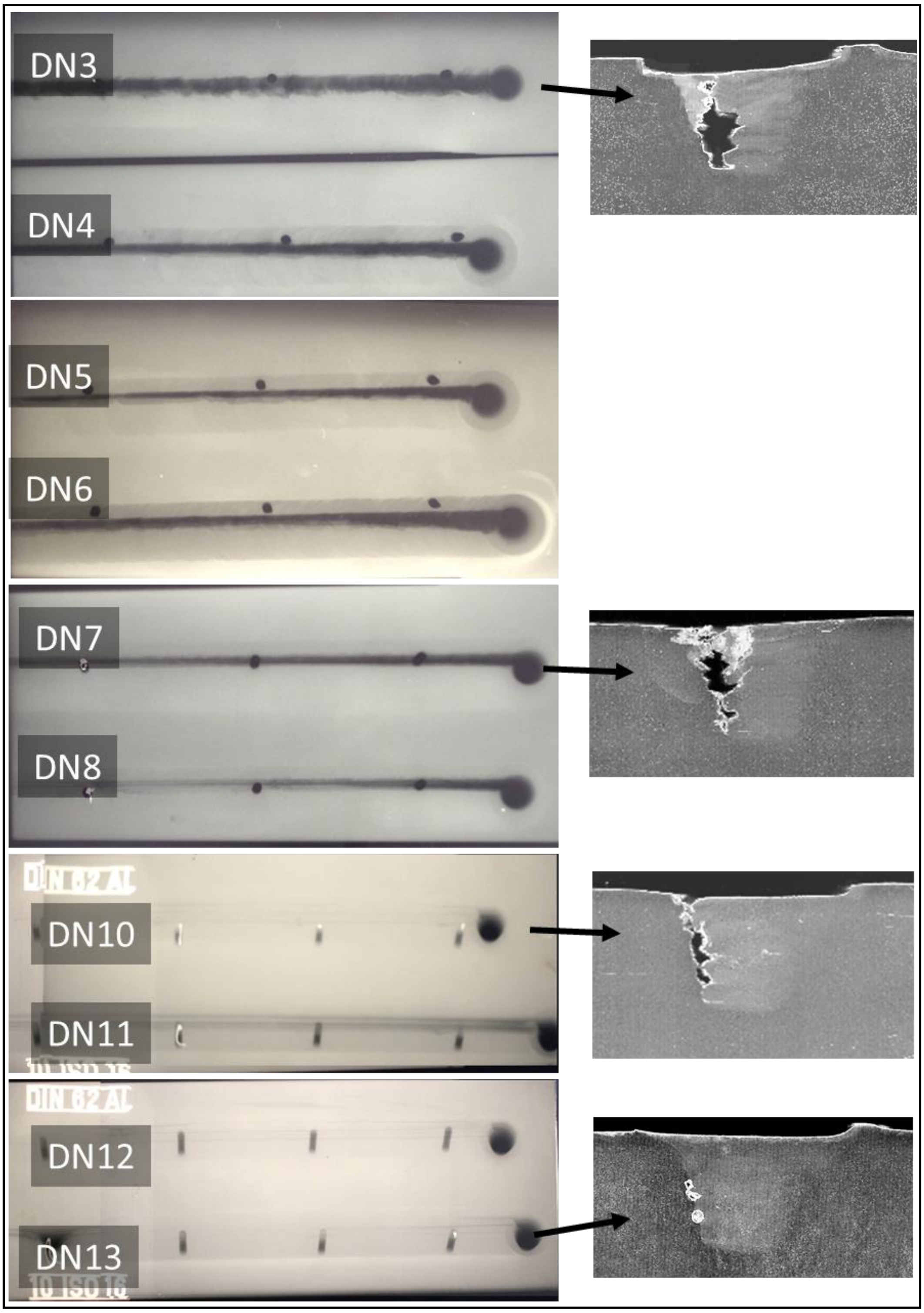

Figure 45. Radiography of trials with tool A01.

### 4.1.2. Tool Triflute

The second tool used for friction stir processing was machined by CNC machine. It has a scroll shoulder and a threaded pin. Three flutes has been machined on the pin part (Figure 46).

Figure 46. The photograph of the “triflute” tool.

The trials with the triflute tool have been performed for different rotational speeds and travel speeds (Table 9). Tilt angle was kept zero.

Table 9. The processing parameters used in trials with the tool “triflude”

| | **Rotation speed (rpm)** | **Travel speed (mm/min.)** |
|---|---|---|
| **N14** | 210 | 24-40-100 |
| **N15** | 290 | 100 |
| **N16** | 290 | 100 |
| **N17** | 290 | 100 |
| **N18** | 290 | 100 |
| **N19** | 210 | 185 |
| **N20** | 210 | 185 |
| **N21** | 110 | 185 |
| **N22** | 150 | 185 |
| **N23** | 980 | 40 |
| **N24** | 720 | - |
| **N25** | 530 | - |
| **N26** | 530 | 65 |
| **N27** | 530 | 100 |
| **N28** | 530 | 185 |
| **N29** | 390 | 65 |
| **N30** | 390 | 100 |
| **N31** | 210 | 185 |

The triflute tools was broken several times during FSP. For example, in the 20th trial, tool fractured while it was being inserted into the plate (Figure 47). Therefore, it has been decided to work with the triflat tool.

Figure 47. Surface appearance after the trials with the tool triflude.

### 4.1.3. Tool Triflat

Triflat tool was used to process weld metal and study the effect of heat input. No tilting was applied. Processing was done on a milling machine such that underneath of processing line was not empty. In Table 10, trial processing parameters are given. Both single-pass and multi-pass processing were done. The single-pass studies 210 rpm-185 mm/min. and 720 rpm- 100 mm/min. were chosen as low heat input and high heat input sets respectively. Multi-pass processing parameters were 290 rpm- 185 mm/min., 720 rpm- 100 mm/min. and 290 rpm- 100 mm/min.. After comparison of FSP trials, 290 rpm -100 mm/min. parameter set was determined to be used in latter studies, i.e. FSP of the as-welded plates, in order to keep temperature and forces on the machine low.

Table 10. Processing parameters used in trials with the tool “triflat”.

| | Rotation speed (rpm) | Travel speed (mm/min.) |
|---|---|---|
| **N32** | 210 | 185 |
| **N33** | 530 | 185 |
| **N34** | 530 | 100 |
| **N35** | 720 | 65 |
| **N36** | 720 | 100 |
| **N37** | 290 | 185 |
| **N38** | 290 | 100 |

## 4.2. Microstructural Examination and Analyses

In this section, macro photos and images taken by optical microscope and scanning electron microscope are shown. Combinations of the images are also illustrated for comparison of different regions in friction stir processed samples. The results of grain size measurements are given. Intermetallic compounds were analyzed in terms of EDS and area fractions.

### 4.2.1. Microstructure of Al 5083 H111

Grain size of the base metal was found to be 92-25-58 μm in L-S-T direction with standard deviation of 6 μm (Figure 48).

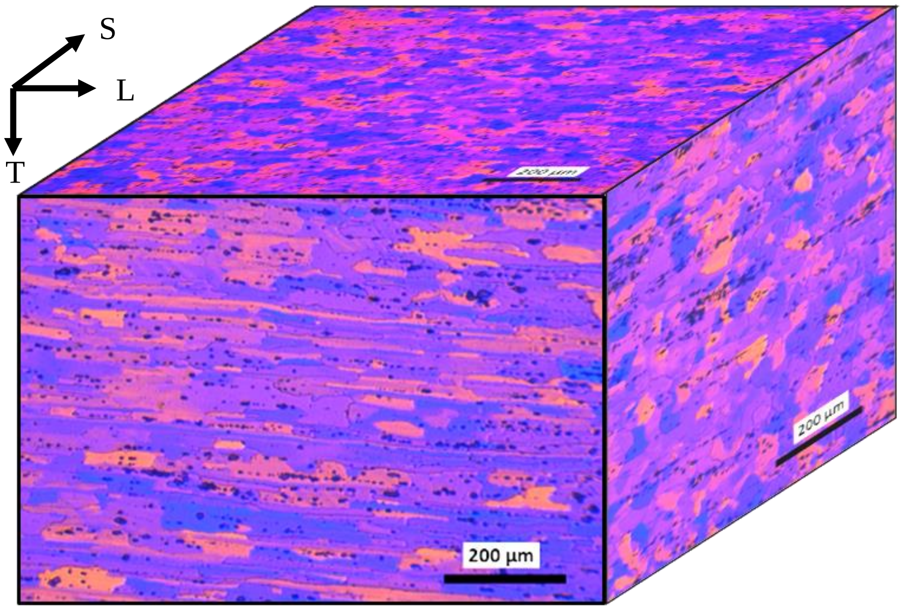

Figure 48. Optical images of etched base metal.

After testing, the compact tension specimens were etched. Images were taken near the fractured surface (Figure 49). Grain boundary spacing along the crack propagation direction was calculated as 54±9 μm.

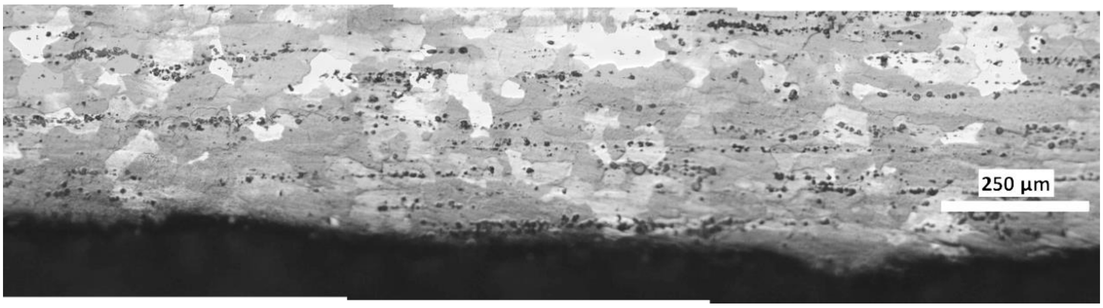

Figure 49. Images taken from the side view of the compact tension specimen of the base metal.

Two type of intermetallic compounds were observed as black and gray by optical microscope. Area fraction of secondary particles was 0.4-0.6-0.4 for optically black particles and 1.4-1.2-1.4 for optically gray particles in the sequence of perpendicular to rolling direction, parallel to rolling direction and rolling surface. Standard deviation was 0.2 for black, while it was 0.3 for gray particles. Images obtained by optical microscope are shown in Figure 50. In Figure 51, images taken by scanning electron microscope are also given. Intermetallic compounds were observed as the same way by SEM as by optical microscope; i.e. black particles as dark zones and gray particles with a lighter tone.

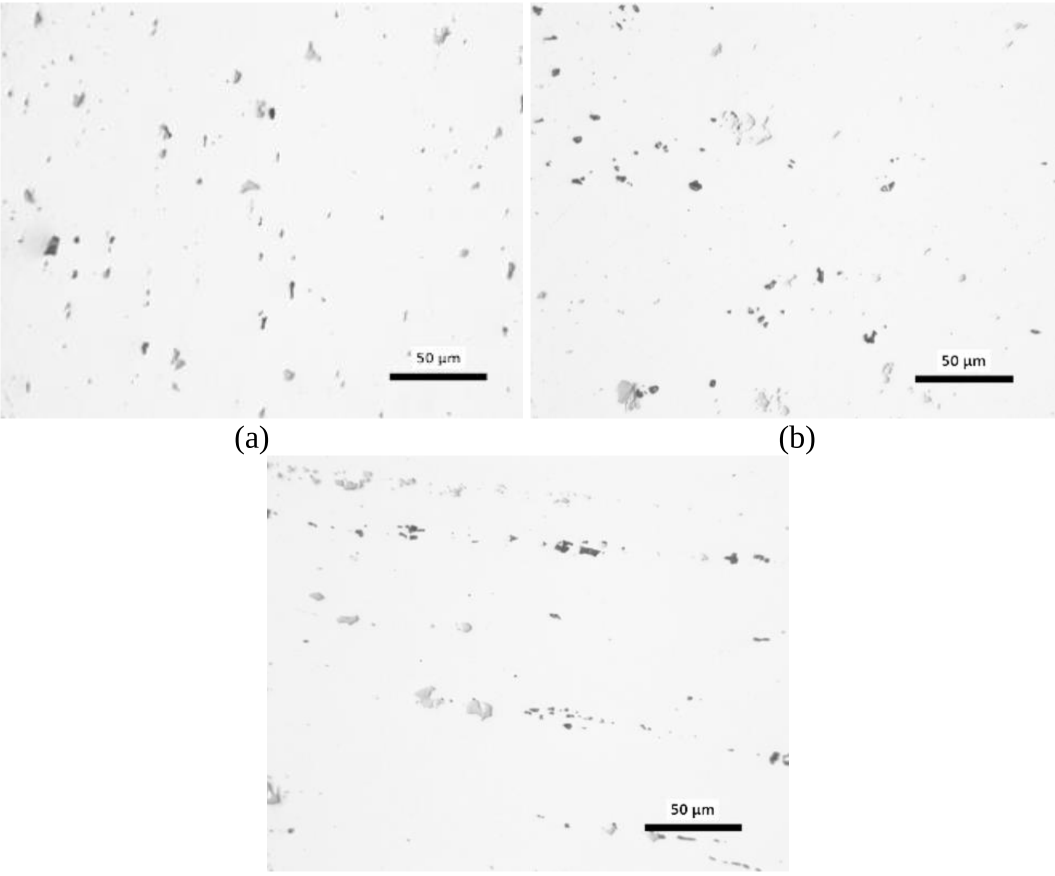

(a) (b)

(c)

Figure 50. Optical images of as-polished base metal (a) Perpendicular to the rolling direction, (b) Rolling surface, (c) Parallel to the rolling direction.

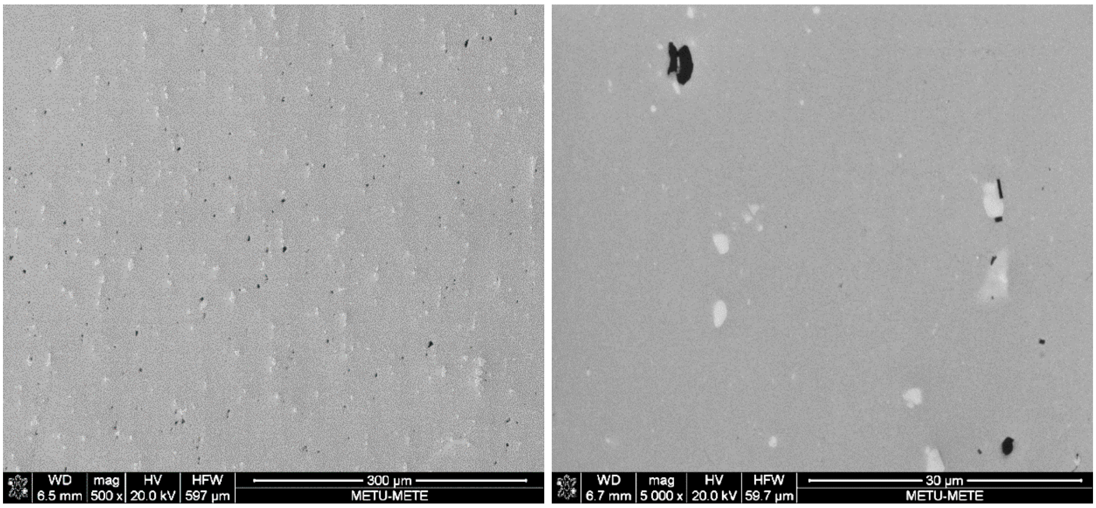

Figure 51. SEM of base metal from perpendicular to the rolling direction.

Energy-dispersive X-ray spectroscopy (EDS) indicates two types of secondary particles similar to the optical images. The black particles can be $Mg_2Si$ because EDS analysis result in high amount of magnesium and silicon (Figure 52 and Figure 53).

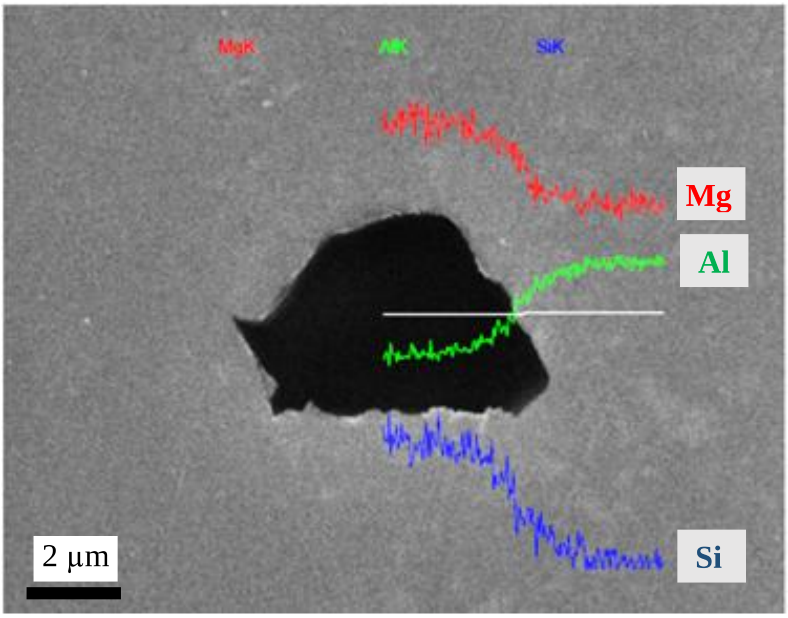

Figure 52. Line EDS analysis of the optically black secondary particle.

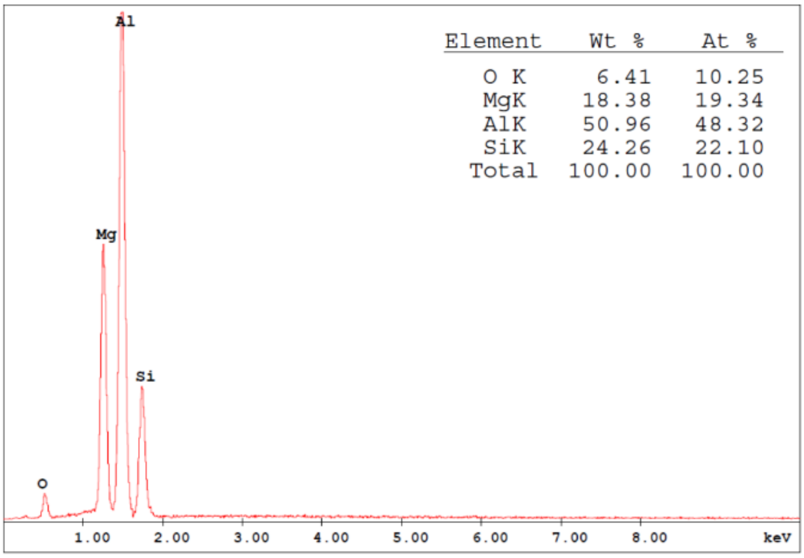

| Element | Wt % | At % |
|---|---|---|
| O K | 6.41 | 10.25 |
| MgK | 18.38 | 19.34 |
| AlK | 50.96 | 48.32 |
| SiK | 24.26 | 22.10 |
| Total | 100.00 | 100.00 |

Figure 53. EDS result of optically black secondary particle.

On the other hand, the gray particles has been found to be a phase containing Al-Mn-Fe-Si (Figure 54 and Figure 55). One possible intermetallic compound found in literature is $Al_{12}(Fe,Mn)_3Si$ [13, 47, 12].

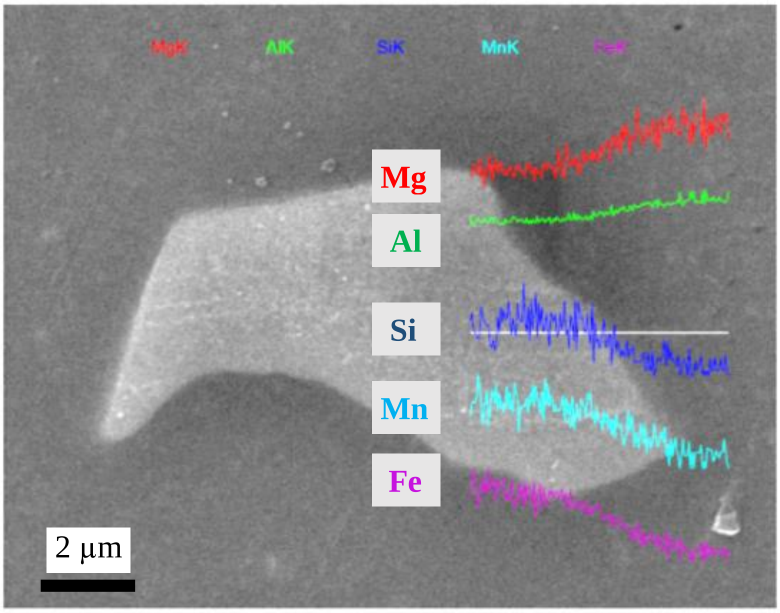

Figure 54. Line EDS analysis of the optically gray secondary particle.

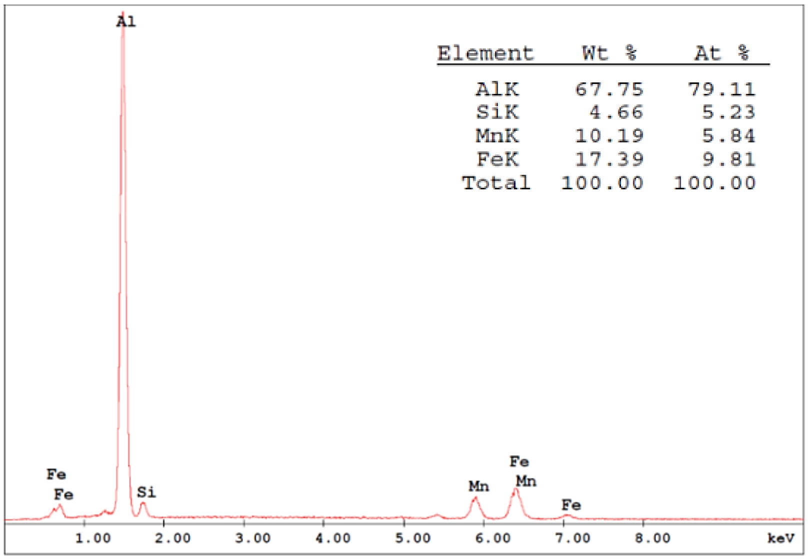

| Element | Wt % | At % |
|---|---|---|
| AlK | 67.75 | 79.11 |
| SiK | 4.66 | 5.23 |
| MnK | 10.19 | 5.84 |
| FeK | 17.39 | 9.81 |
| Total | 100.00 | 100.00 |

Figure 55. EDS results of optically gray secondary particle.

### 4.2.2. Microstructure of Friction Stir Processed Plates

#### 4.2.2.1. Single pass studies

Single pass studies 720 rpm- 100 mm/min and 210 rpm– 185 mm/min are named as high heat input and low heat input respectively. Grain size measurements were done at the center of nugget zone. Samples were examined only from transverse surface. Images taken from the high heat input sample gave an average grain size of 6±1 μm (Figure 56a). On the other hand, electron backscatter diffraction of the low heat input sample shows average grain size of 1 μm (Figure 57).

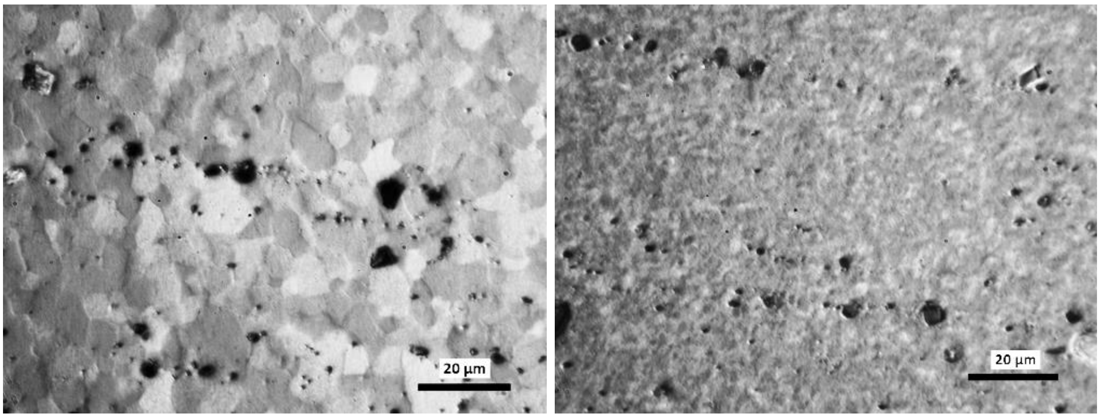

(a) (b)

Figure 56. Optical images of the FSPed samples (a) 720 rpm– 100 mm/min, (b) 210 rpm– 185 mm/min.

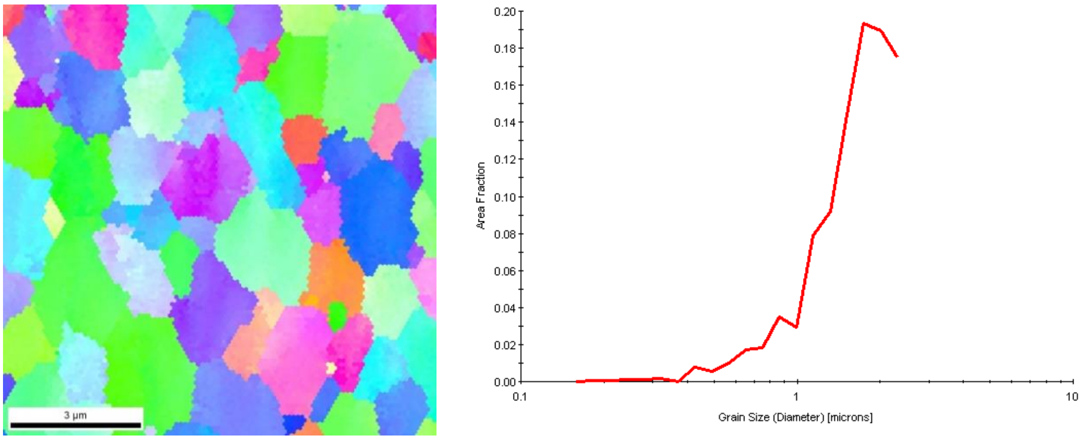

Figure 57. Electron backscatter diffraction image and grain size vs area fraction graph of the FSPed sample (210 rpm– 185 mm/min.).

Top views of the plates are given in Figure 58. Flash formation is observed at high heat input parameter set.

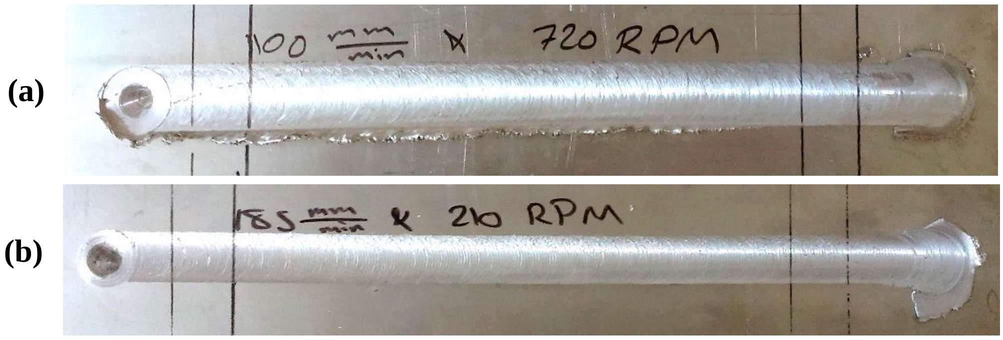

Figure 58. Top view of friction stir processed base metal
(a) High heat input, (b) Low heat input.

In Figure 59, macro images of the samples are shown. Nugget of the high heat input sample is larger compared to the low heat input sample. Images of two parameter sets were taken along a line in way that they include nugget, thermos-mechanically affected zone and unaffected base metal (Figure 59).

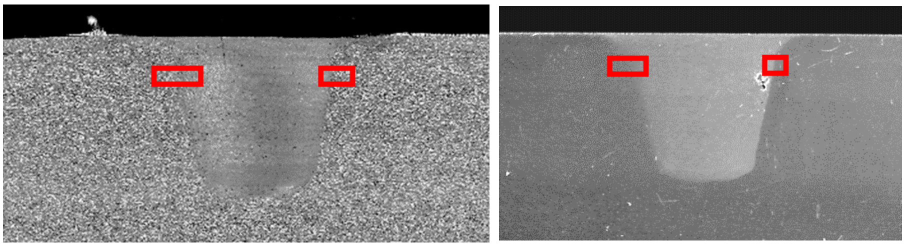

(a) (b)

Figure 59. Friction stir processed base metal (a) High heat input, (b) Low heat input.
Images were taken inside the red rectangles.

Thermo-mechanically affected zone (TMAZ) of the low heat input sample was found to be narrower compared to TMAZ of the high heat input sample (Figure 60 and Figure 61).

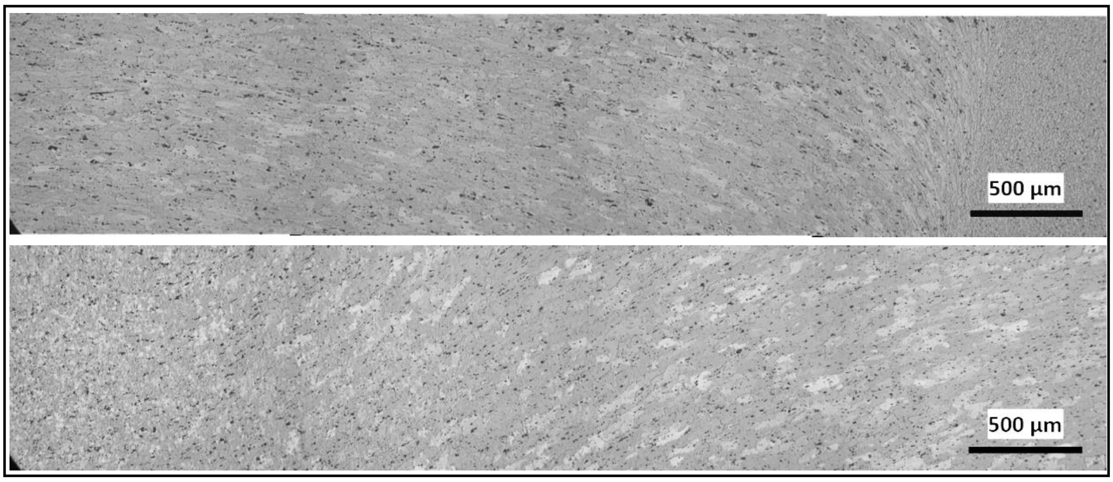

Figure 60. Combined optical images of the parameter set of 720 rpm– 100 mm/min.

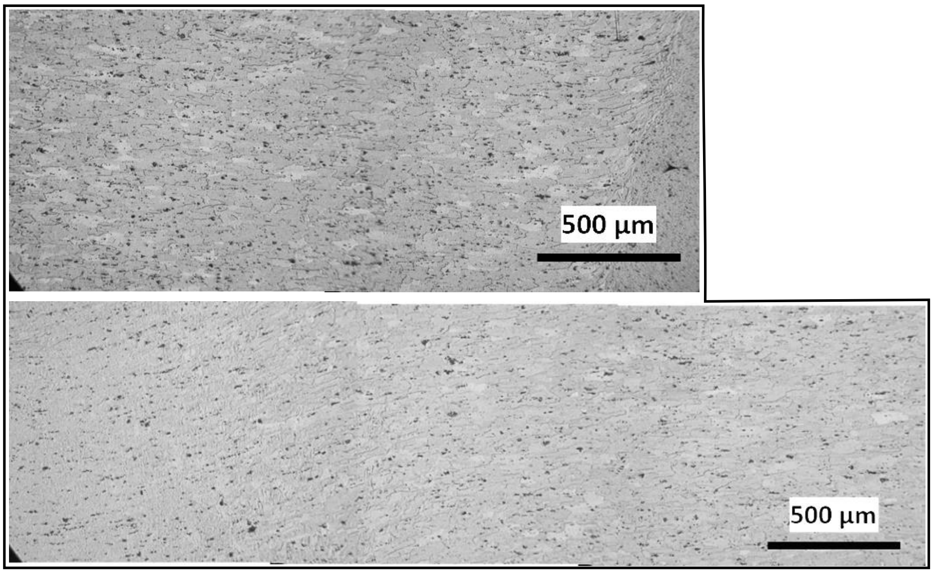

Figure 61. Combined optical images of the parameter set of 210 rpm– 185 mm/min.

To examine the microstructure of the nugget zone, the images were taken from regions shown in Figure 62. Inhomogeneity was observed in terms of grain size. Bottom part of the nugget seems to have greater grain size than upper part of the nugget (Figure 63 and Figure 64).

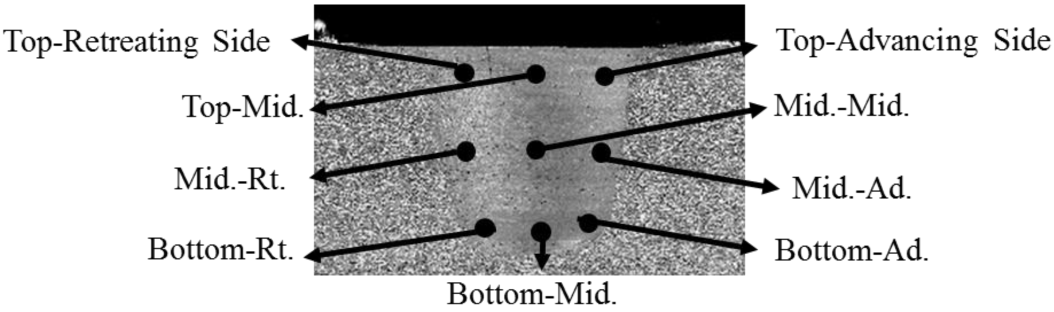

Figure 62. Positions of the images taken from nugget.

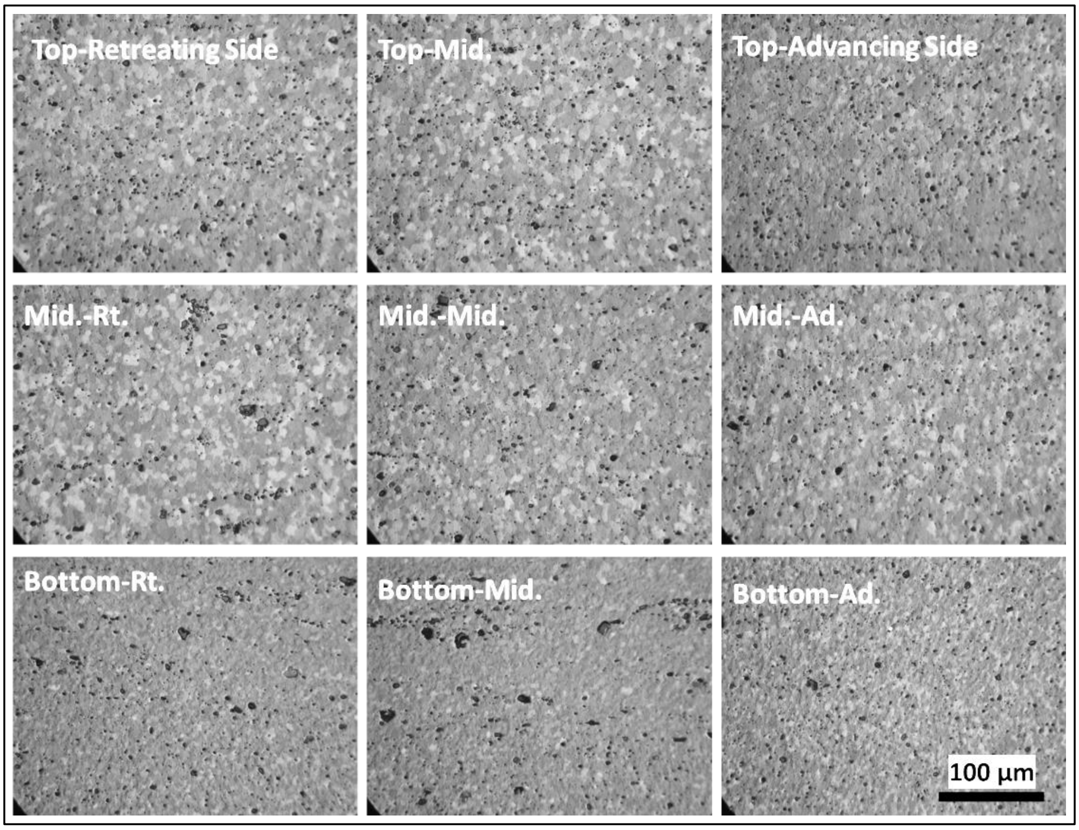

Figure 63. Optical images of the nugget (720 rpm– 100 mm/min., FSP).

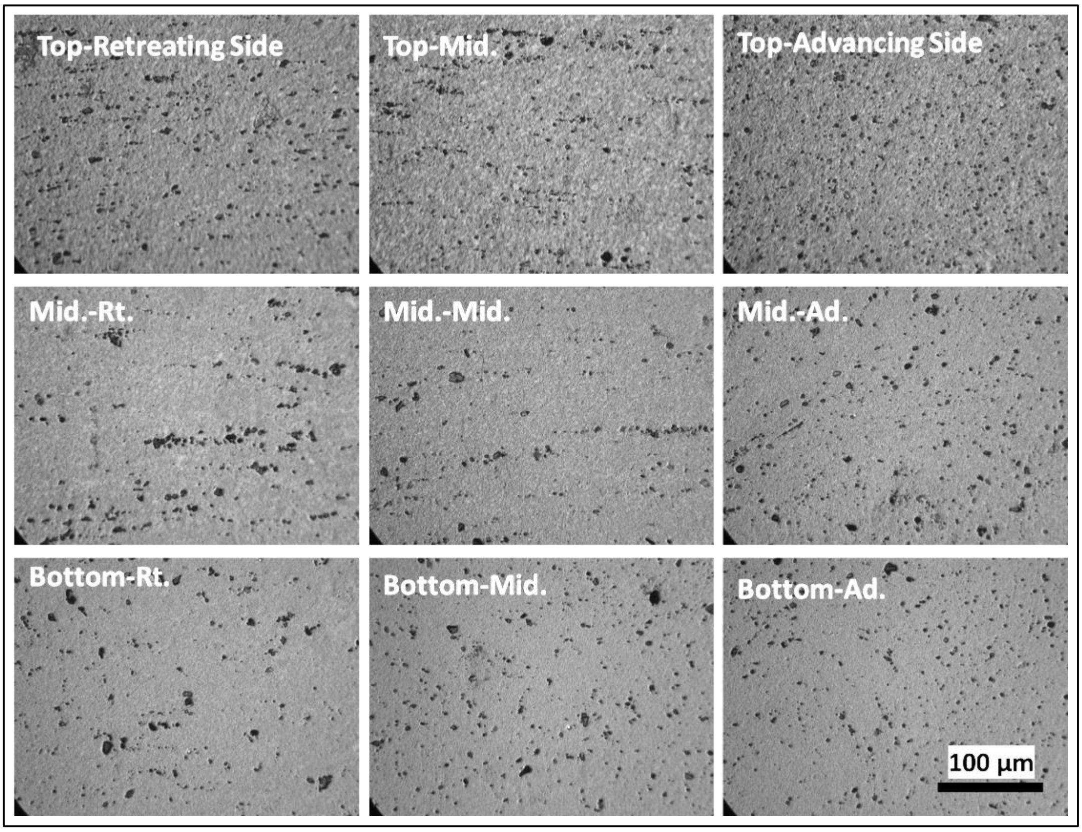

Figure 64. Optical images of the nugget (210 rpm– 185 mm/min., FSP).

#### 4.2.2.2. Multi-pass FSP studies

Multi-pass FSP studies were performed on the base metal (Figure 65).

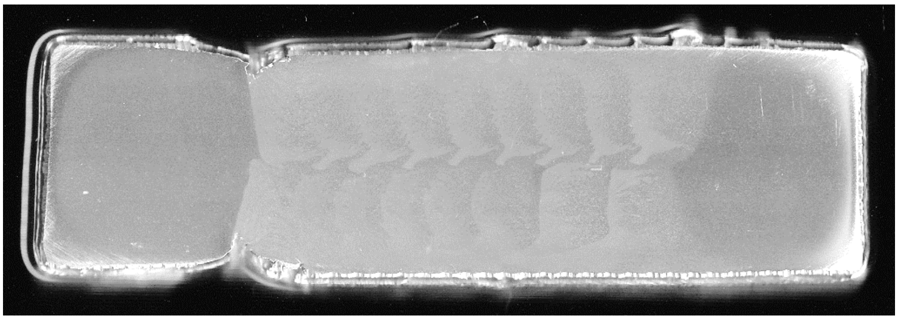

Figure 65. Macrograph of the multi-pass FSPed base metal (290 rpm– 185 mm/min.).

Grain size at the center of nugget was found to be same for single pass studies. While the average grain size after FSP with 720 rpm- 100 mm/min. was calculated as 6±1 μm (Figure 66), both 290 rpm- 100 mm/min. and 290 rpm- 185 mm/min. FSPed samples have been found to have the average grain size of 3±2 μm (Figure 66 and Figure 67).

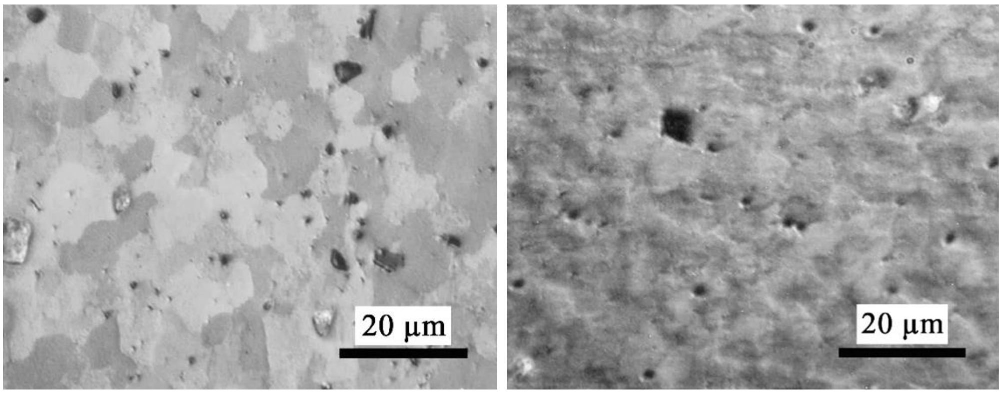

(a) (b)

Figure 66. Polarized optical microscope images (a) Multi-pass FSP with 720 rpm-100 mm/min, (b) Multi-pass FSP with 290 rpm- 185 mm/min..

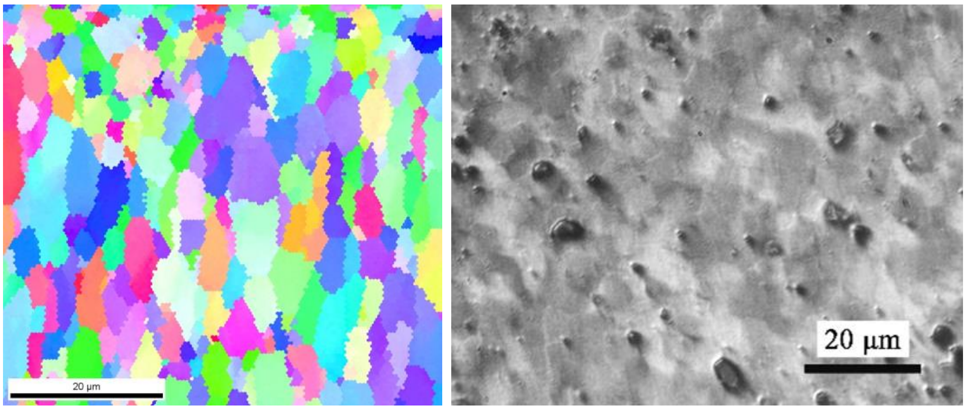

(a) (b)

Figure 67. Multi-pass FSP with 290 rpm- 100 mm/min.
(a) EBSD image, (b) Polarized optical microscope image.

### 4.2.3. Microstructure of As-welded Plates

Macrographs of the as-welded samples are given in Figure 68. One weldment had lack of penetration whereas other weldments were sound. The former was friction stir processed for further testing.

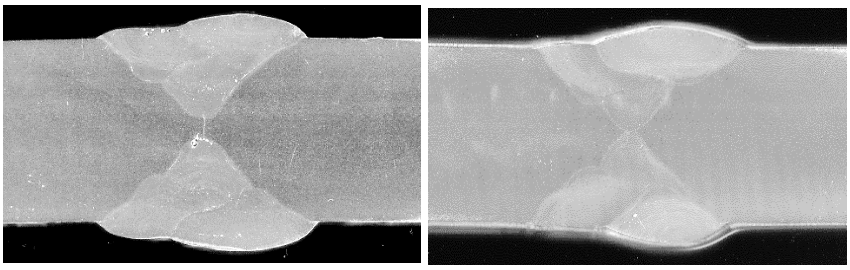

(a) (b)

Figure 68. Gas metal arc welded plates

(a) With lack of penetration, (b) Without any macro discontinuities.

Grain size measurement was done on the surface perpendicular to the rolling direction/welding direction. The average grain size is 47±9 µm (Figure 69).

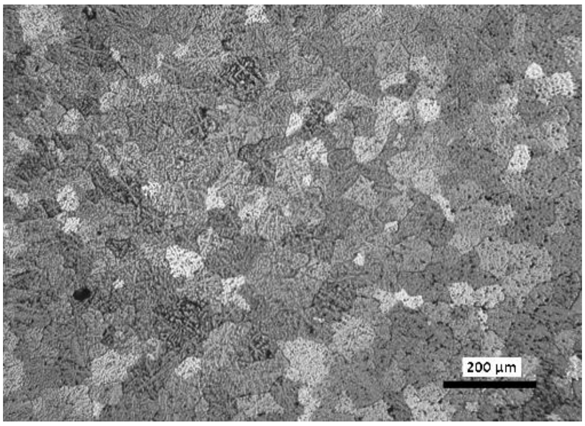

Figure 69. Optical image of the as-welded plate.

Grain boundary distance along crack growth direction in the compact tension samples was calculated as 45±5 µm. In Figure 70, combined images are given.

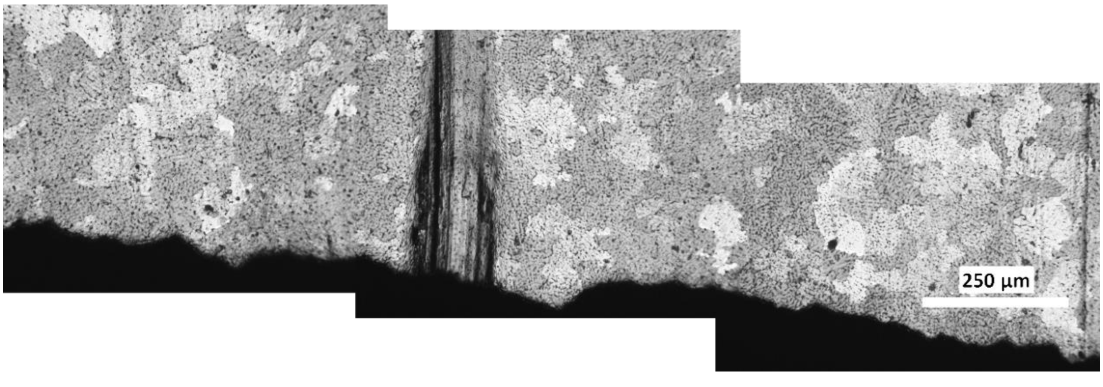

Figure 70. Side view of the compact tension specimen prepared from the weld metal.

Porosities and small intermetallics were observed (Figure 71). Size and fraction of secondary phases was too small to measure or count.

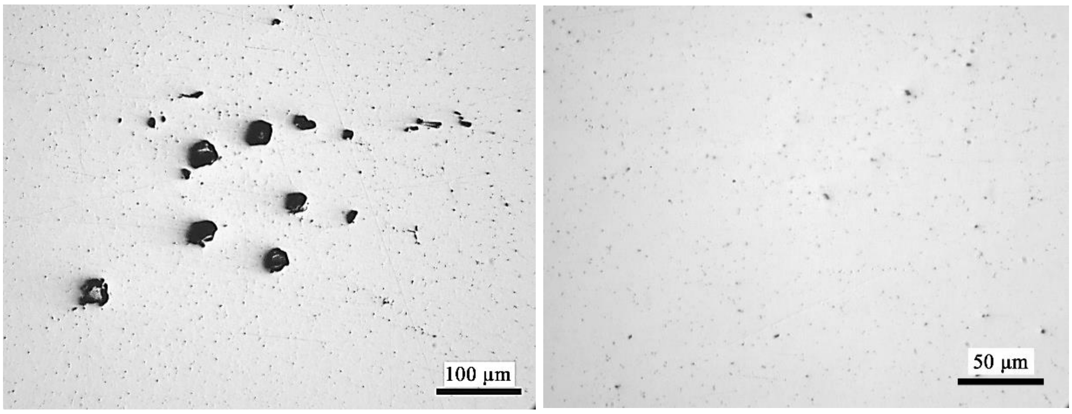

(a) (b)

Figure 71. Optical images of the polished weld metal
(a) Porosity, (b) Secondary particles.

Energy dispersive X-ray of secondary particles were found to be same as the ones in the base metal. In Figure 72, scanning electron microscope image of polished surface is given.

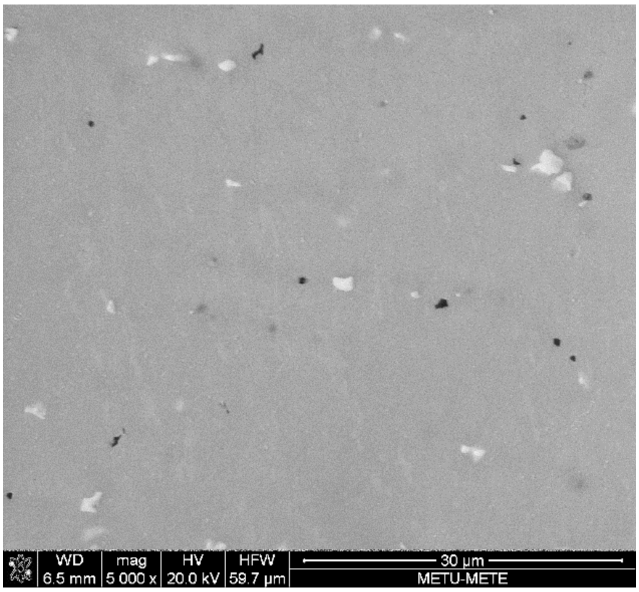

Figure 72. Scanning electron microscope image of the weld metal.

### 4.2.4. Microstructure of Friction Stir Processed Weldments

Stir zone passes the fusion line; consequently, alloy composition of weld metal could have changed with friction stir processing. On the other hand, any defects like lack of penetration is closed as shown in Figure 73.

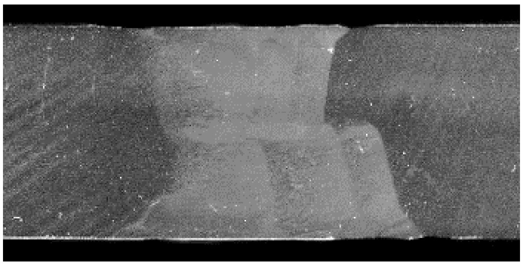

Figure 73. Friction stir processed weldment of Figure 68a

Optical images were taken from the rectangles shown in Figure 74. The combined images taken from the red rectangle are given in Figure 75 to show different structures of base metal, weld metal and FSPed weld metal.

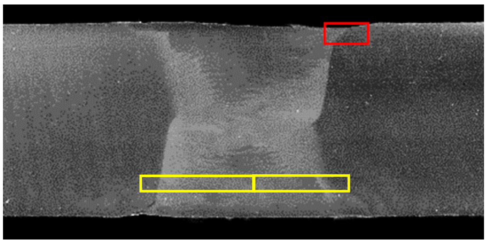

Figure 74. Friction stir processed weldment of Figure 29b.

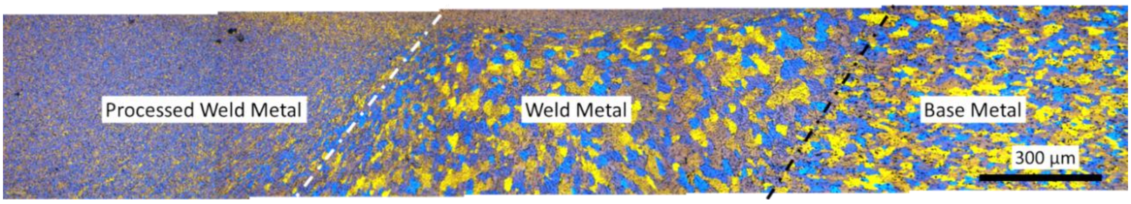

Figure 75. Combined optical images showing FSPed weld metal, weld metal and base metal.

In Figure 76, the combined images taken from the yellow rectangle are shown. The stir zone is seen to be inhomogeneous.

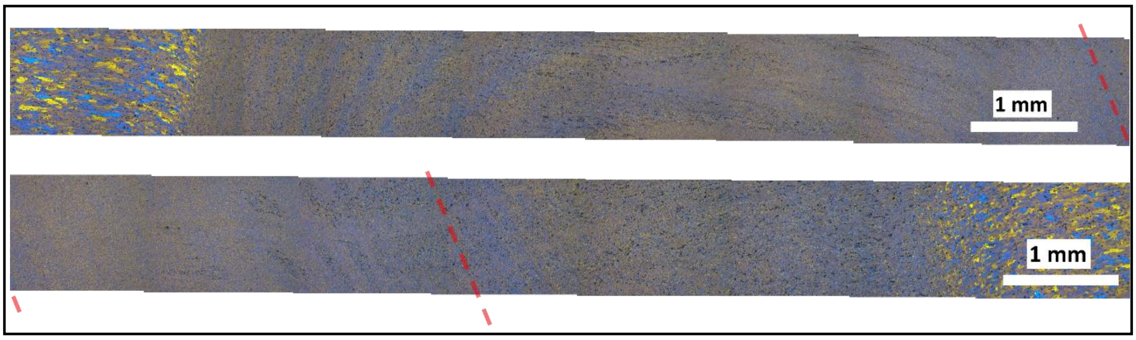

Figure 76. Combined optical images of stir zone.

Measurements on the images of the FSPed weld metal gave an average grain size of 3.5 µm throughout the stirred zone with a standard deviation of 1 µm. However, smaller grains are observed at bottom corner at advancing side of stir zone compared to upper retreating corner of stir zone. In Figure 77, images are given to show the differences in grain size in distant regions in stir zone.

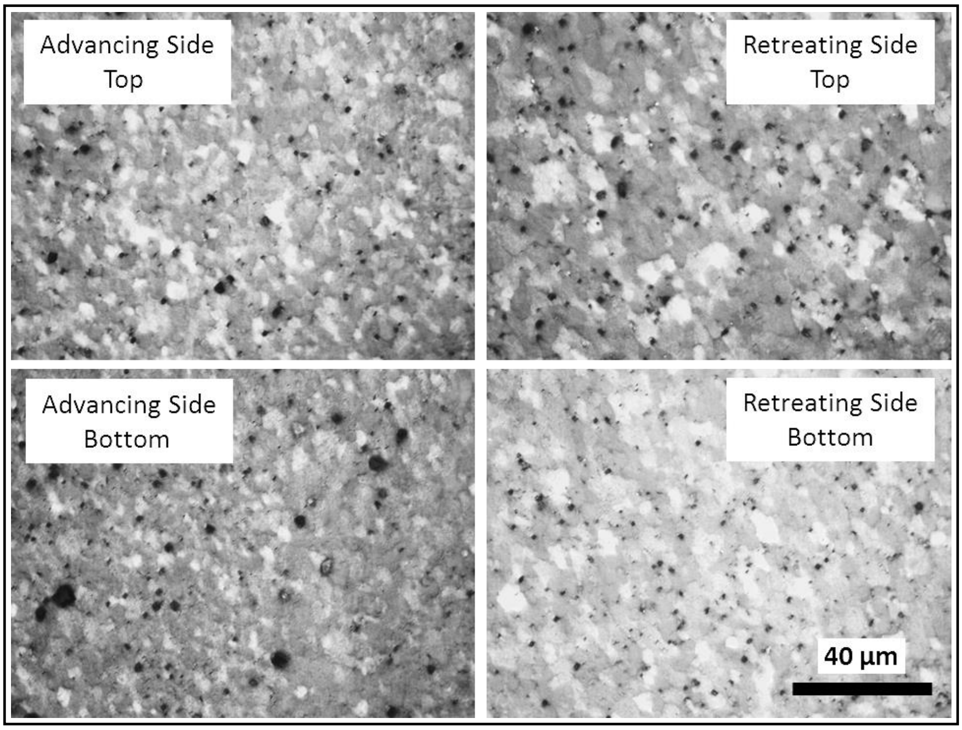

Figure 77. Optical images taken from different zones in the nugget zone of the FSPed weld metal.

Images taken from compact tension specimens are given in Figure 78. Grain boundary spacing along crack propagation line was measured as 3.2±0.5 µm.

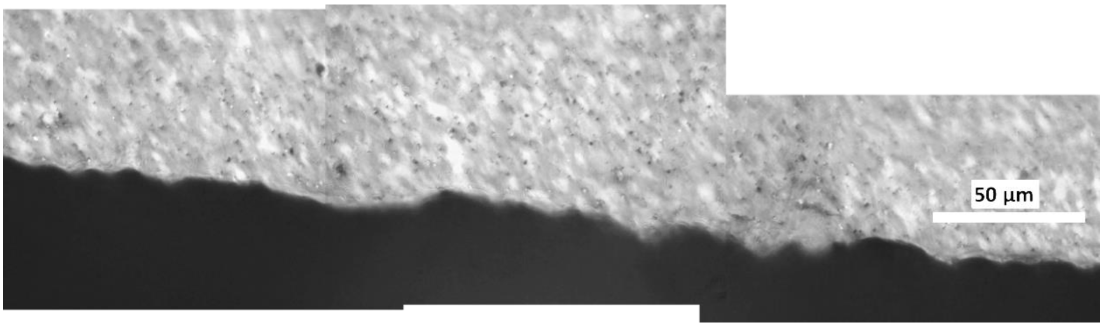

Figure 78. Images taken from side view of compact tension specimen of the FSPed weld metal.

Optical images and scanning electron microscope images of FSPed weld metal are also similar to the images of the as-welded material (Figure 79).

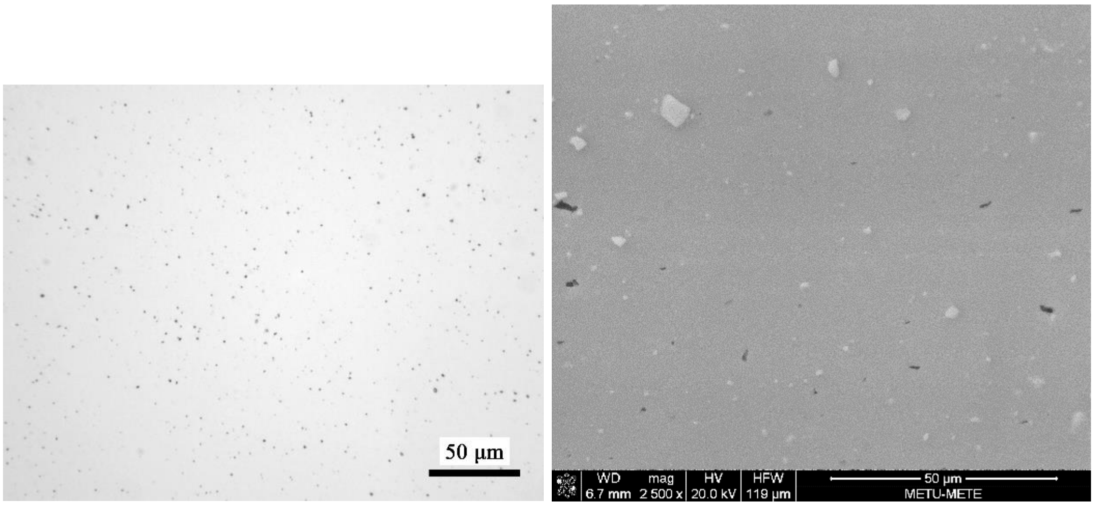

(a) (b)

Figure 79. Images of FSPed weld metal (a) Optical microscope, (b) SEM.

## 4.3. Mechanical Tests

Firstly, hardness profiles of as-welded plates and FSPed weldments are plotted. Secondly, fracture surfaces and tensile strengths obtained by tensile tests are compared. Finally, results of fatigue crack growth tests are given in the sequence of macro images of compact tension specimens, coefficients of Paris-Erdoğan region, stress intensity threshold, SEM analysis of crack line and fracture surface of compact tension specimens.

### 4.3.1. Hardness Profiles

#### 4.3.1.1. Hardness of friction stir processed base metal

Hardness profiles of multi-pass studies were taken both vertically and horizontally as shown in Figure 80.

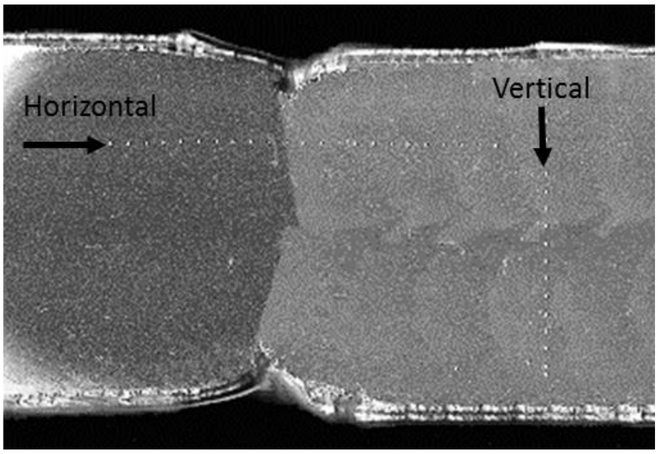

Figure 80. Vertical and horizontal hardness test indentation marks on multi-pass FSP sample (290 rpm -185 mm/min.).

Vertical hardness profiles of two multi-pass studies are given in Figure 81. While 290 rpm-185 mm/min. was found to have higher hardness, vertical hardness of multi-pass studies were found to be roughly uniform.

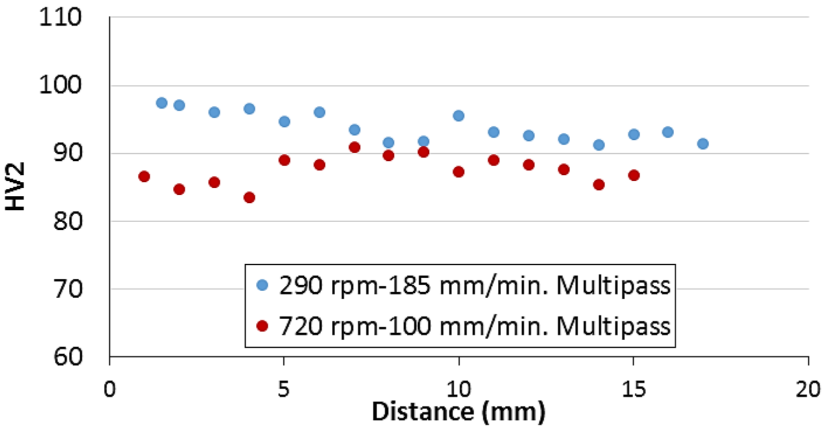

Figure 81. Vertical hardness profiles.

In Figure 82, horizontal hardness profiles are shown. Hardness of single pass and multi-pass studies with same process parameters were found to be similar. Low heat input, i.e. lower ratio of rotational speed to travel speed, causes higher hardness values. On the other hand, higher input studies tend to form a heat affected zone with lower hardness.

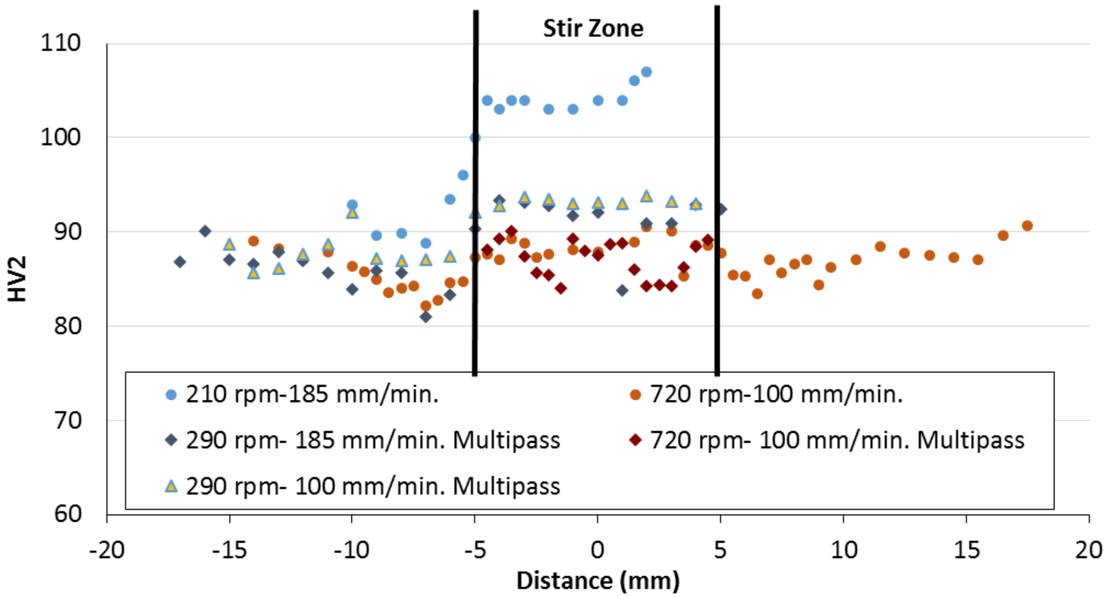

Figure 82. Horizontal hardness profiles of FSPed base metal samples.

#### 4.3.1.2. Hardness of the as-welded samples

The average hardness of the weld zone is 80±8 HV2 while that of the base metal is 89±5 HV2. In Figure 83, hardness profile starting at the center of weld metal is given. It can be separated into three regions depending on hardness values; weld metal, heat affected zone and unaffected base metal. The hardness in the heat affected zone is between those of the weld metal and base metal, i.e. 85 HV2.

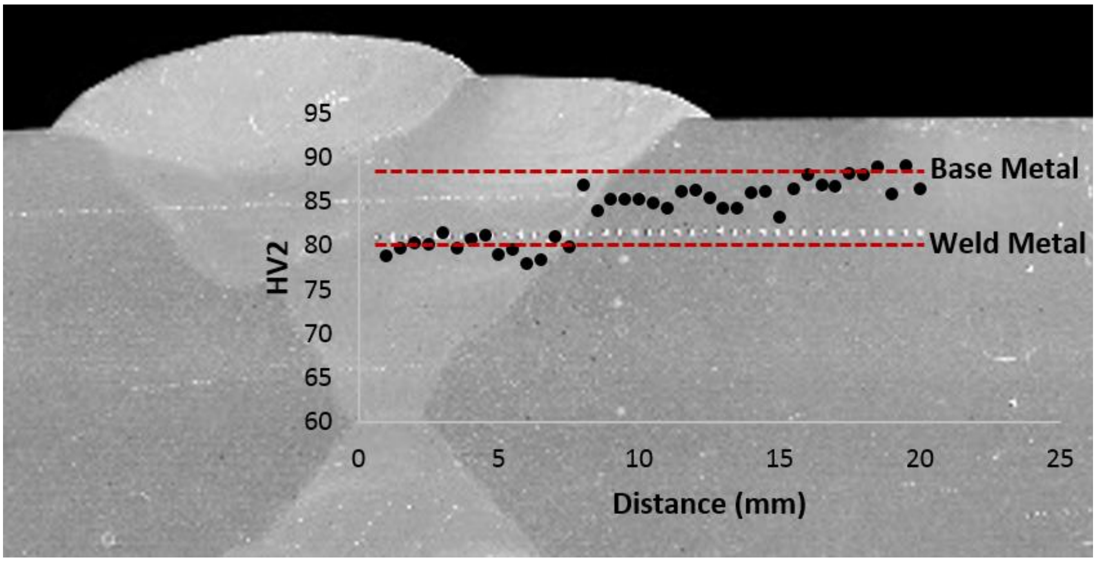

Figure 83. Hardness profile of the as-welded material.

#### 4.3.1.3. Hardness of the friction stir processed weld metal

The hardness profiles show that the average hardness of the weld zone increased from 80±8 HV2 to 92±3 HV2 after FSP which is similar to the hardness of unprocessed base material (Figure 84).

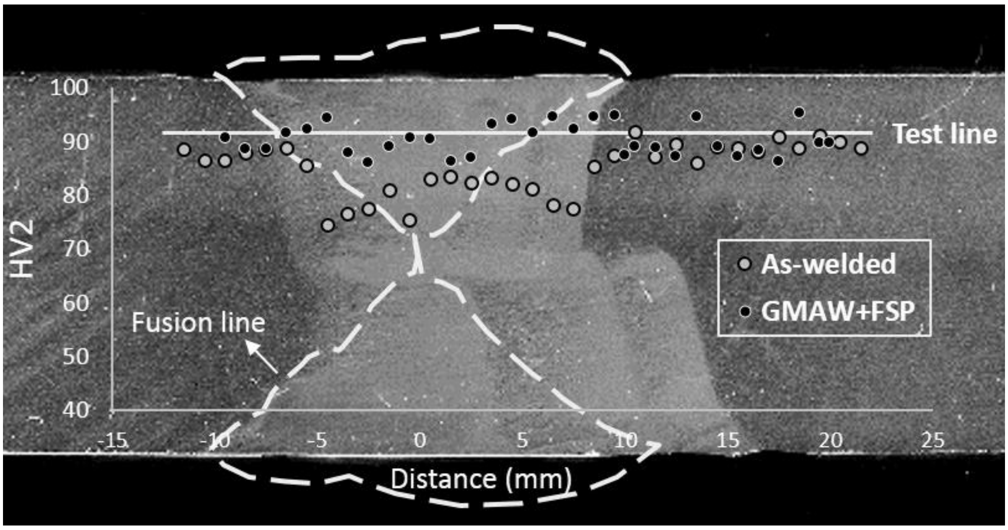

Figure 84. Hardness profiles of the as-welded sample and the FSPed sample.

### 4.3.2. Tensile Test

In Figure 85, tensile strain versus tensile stress graphs of FSPed base metal are given. Effects of friction stir processing was found depend on process parameters. Higher heat input increases elongation while decreasing yield strength. On the other hand, colder parameter set increased the tensile strength of base metal.

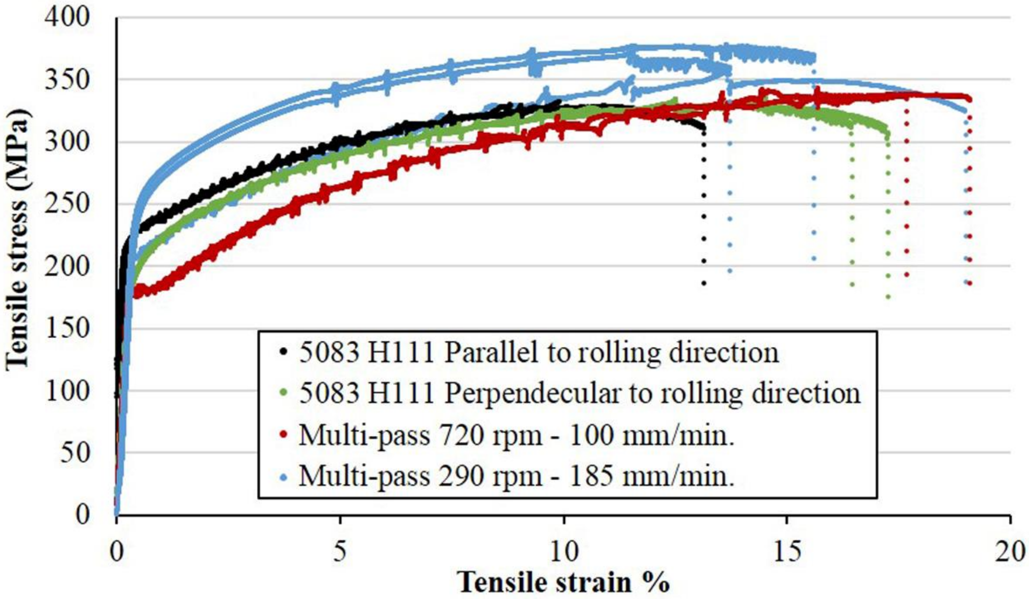

Figure 85. Stress-strain graphs.

Average ultimate tensile strength (UTS) values for the Type I specimens are tabulated in Table 11. Friction stir processing was found to improve ultimate tensile strength of weld metal by 14%; i.e. from 277 MPa to 333 MPa.

Table 11. Tensile test results

| | UTS (MPa) | Standard Deviation |
|---|---|---|
| **5083 H111** | 330 | 5 |
| **Weld Metal** | 277 | 20 |
| **FSPed weld metal** | 333 | 24 |

Cylindrical Type II specimens of the as-welded samples fractured at the fusion line; whereas, failure occurred outside the stir zone of the FSPed weldments.

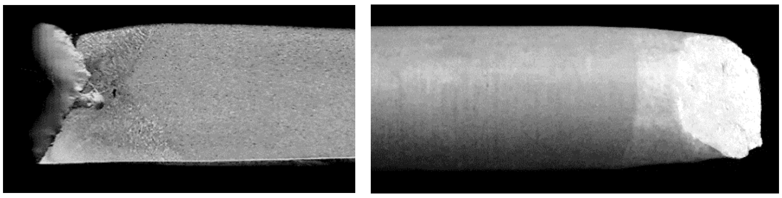

(a) (b)

Figure 86. Fractured Type II tensile specimens (a) Cross-section of as-welded, (b) FSPed weldment.

Fractography of the weld metal displayed a ductile fracture with high amount of discontinuities. For example, porosity and lack of fusion can be seen in Figure 87.

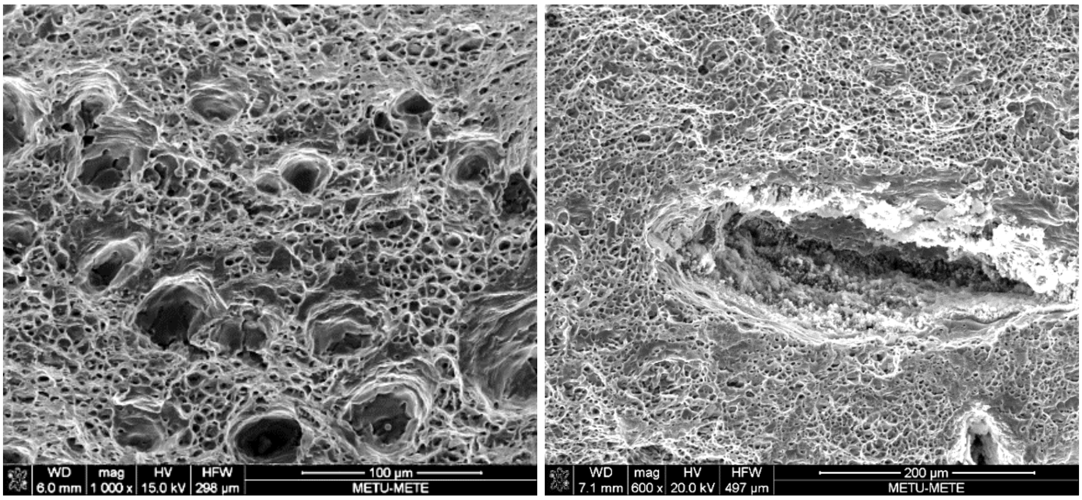

(a) (b)

Figure 87. Discontinuities on the fracture surface of the as-welded specimen (tensile test)

Friction stir processing of weld metal seems to close discontinuities formed during gas metal arc welding. However, some other discontinuities have been observed on the fracture surface of FSPed weld metal sample.

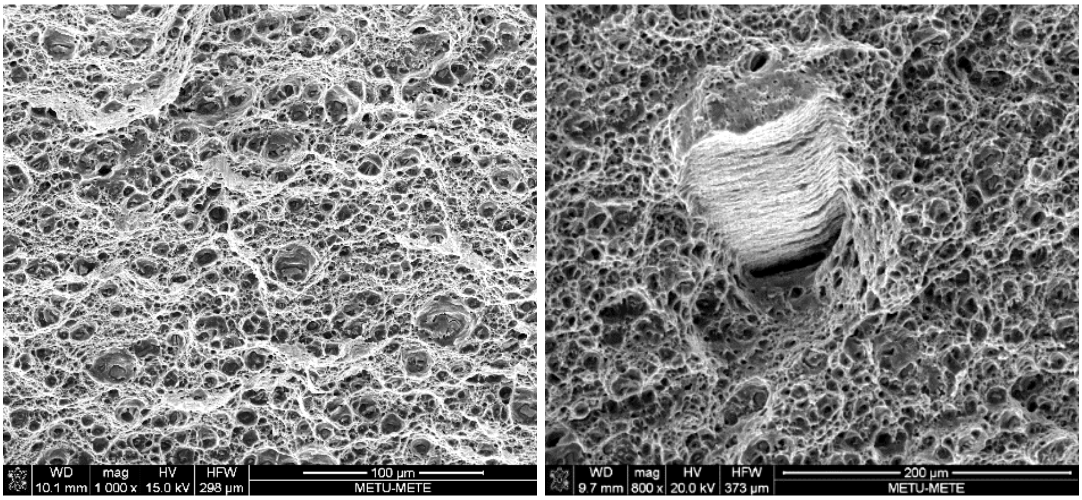

Figure 88. Fracture surfaces of the FSPed weldment (tensile test)

Although some brittle patterns are observed, the majority of the fracture surfaces consist of dimples indicating a ductile fracture (Figure 89).

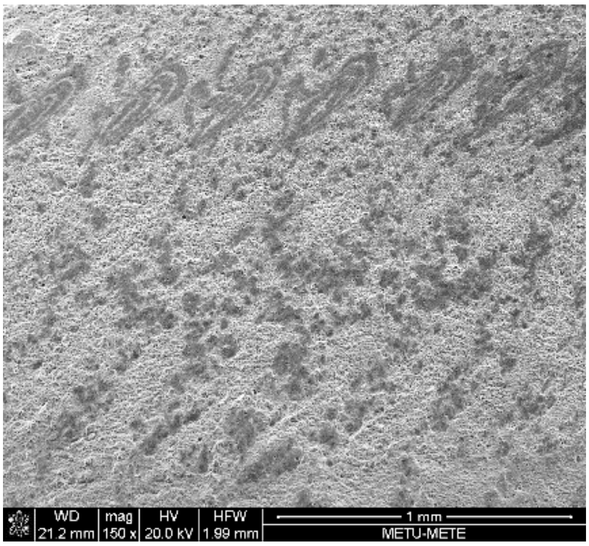

Figure 89. Brittle patterns on the fracture surface of the FSPed weldment (tensile test).

### 4.3.3. Fracture Toughness

Two samples of each condition (base metal, as-welded and FSPed weldment) were tested. Although the test is not valid for calculating $K_{IC}$, conditional results are given in Table 12.

Table 12. Results of fracture toughness tests

| | $K_Q$ (MPa m$^{1/2}$) | Standard deviation |
|---|---|---|
| **Base metal** | 24 | 0.4 |
| **As-welded** | 17 | 1.0 |
| **FSPed weld** | 25 | 1.0 |

Fractography of the base metal samples showed ductile fracture with fractured secondary phases (Figure 90). Three types of particles were distinguished with EDS analysis. These were composed of Mg-Si, Al-Mn-Fe and Al-Mn-Fe-Si.

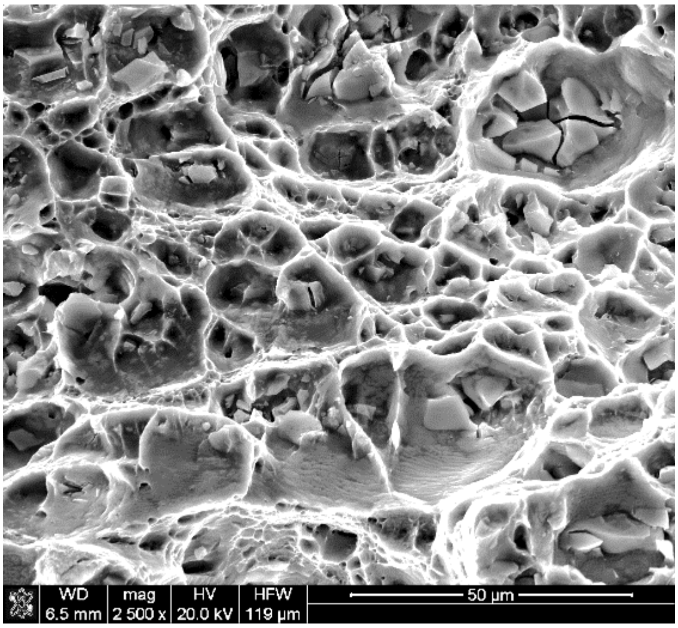

Figure 90. Fracture surface of the base metal (fracture toughness test).

In Figure 91 and Figure 92, SEM images of the as-welded sample are given. High amount of micro porosity was found on fracture surfaces. Few cracked particles were seen in contrast to the base metal. Although some particles were the same as those found in the base metal, EDS analysis gave only aluminum and magnesium peaks.

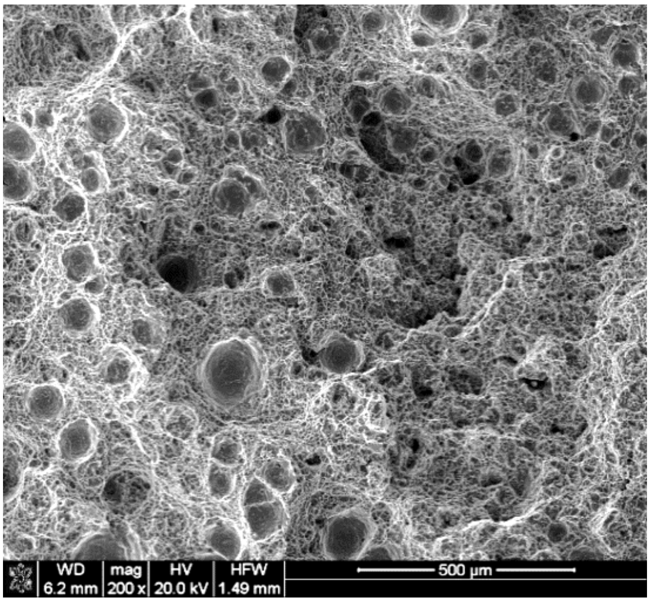

Figure 91. Porosities on the fracture surface of the as-welded sample (fracture toughness test).

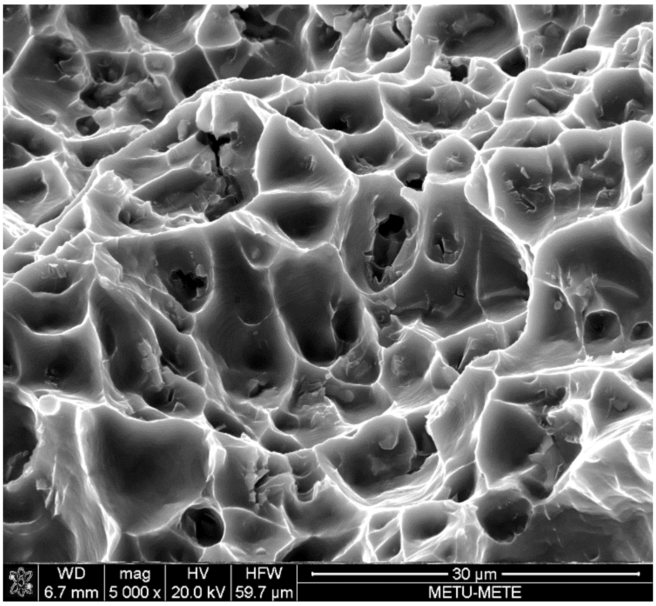

Figure 92. Fracture surface of the as-welded sample (fracture toughness test).

Fracture surfaces of FSPed weldments have dimples with some features that were not observed in others. Very small amount of secondary particles were observed.

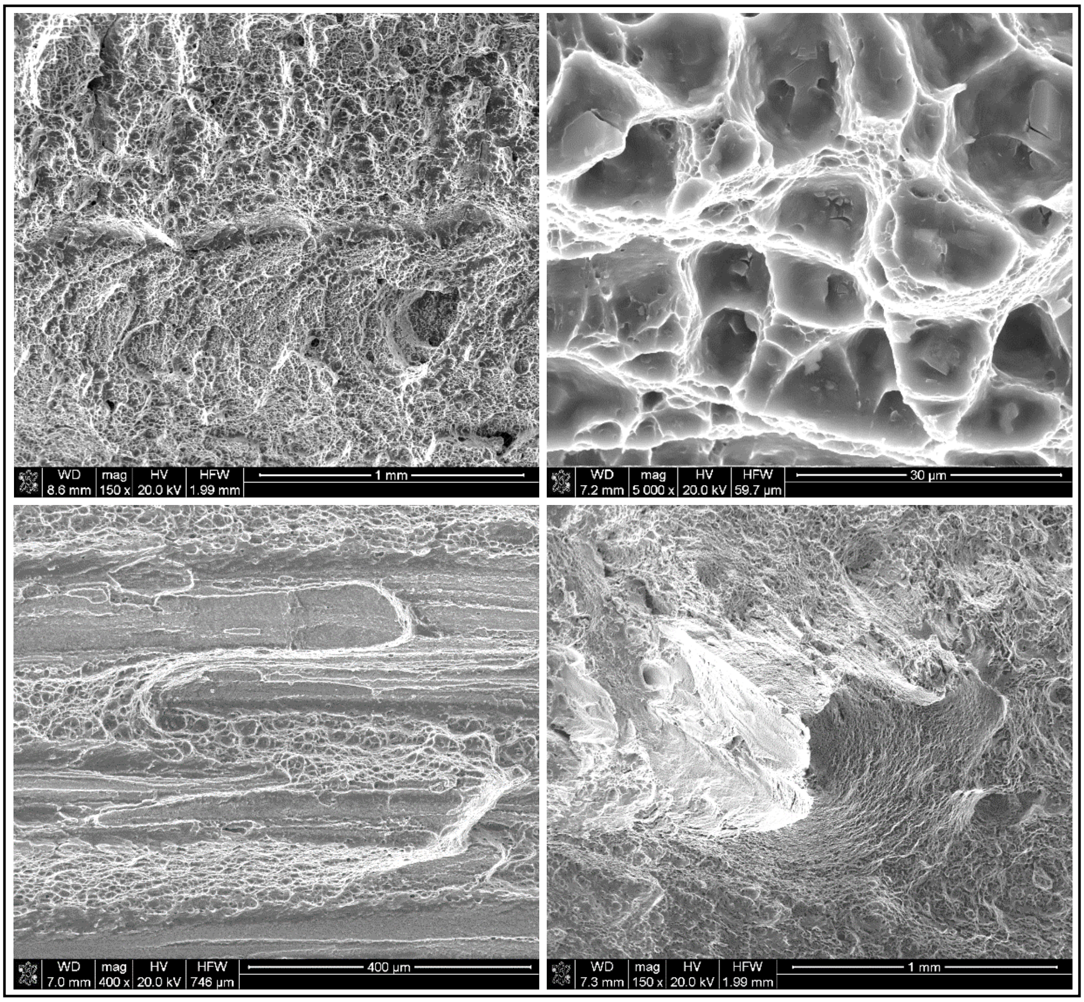

Figure 93. Fracture surface of FSPed weldment (fracture toughness test).

### 4.3.4. Fatigue Crack Propagation

In Figure 94, fractured compact tension specimens are shown. Beach marks are visible on FSPed weld metal specimen. Discontinuities which were not detected by radiographic inspection were found on the fracture surface of the as-welded sample.

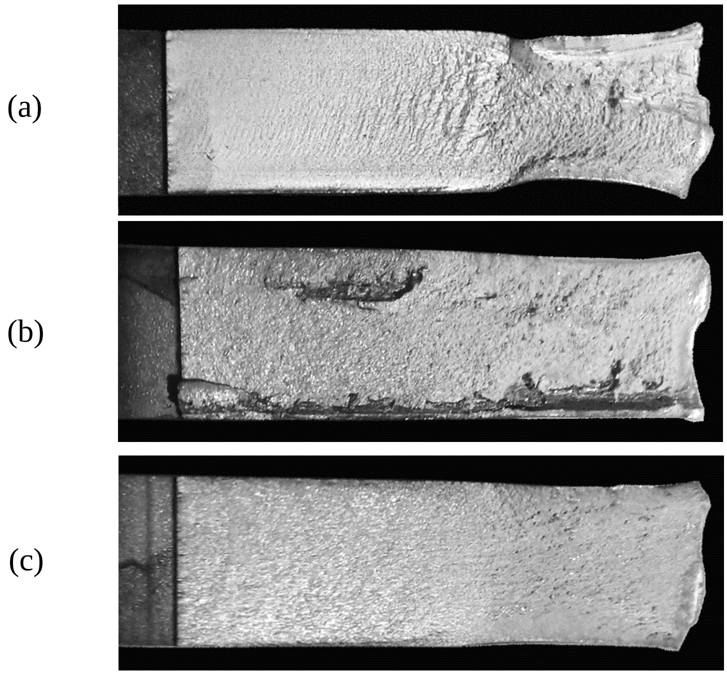

Figure 94. Macro images of the fractured compact tension samples
(a) FSPed weldment, (b) As-welded, (c) Base metal.

The crack growth rate versus stress intensity factor range graphs were drawn for both optical data and crack opening displacement (COD) data. The curves obtained by COD data were found to be similar to the results obtained by optical data for the most of the specimens (Figure 95).

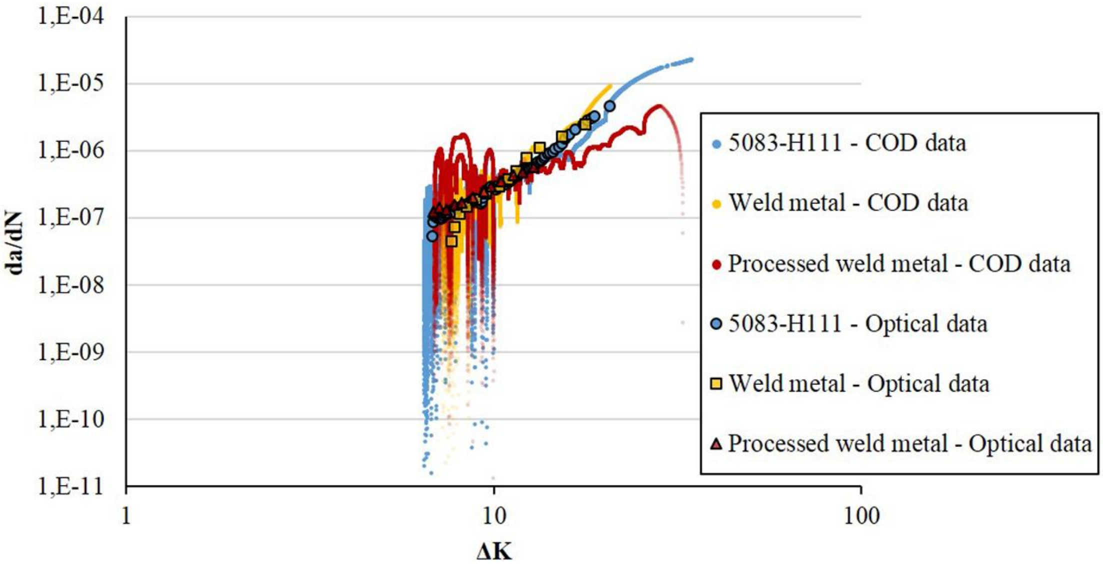

Figure 95. Fatigue crack growth rate versus stress intensity factor range graph

In Table 13, coefficients of Paris-Erdoğan equation and crack growth rate at $\Delta K=15$ MPa $m^{1/2}$ are given. Although crack propagation rate of weld metal is slowest at low stress intensity values, it escalates rapidly at high stress intensities. Diversity of calculated crack growth rate is high for weld metal specimens. It is thought to be due to varying micro-defect density in weld metal specimens. Friction stir processed weld metal specimens showed slower crack growth rate compared to the base metal and its crack growth resistance is determined to be best among base metal and weld metal at high stress intensity levels.

Table 13. Results of the fatigue crack growth investigations

| | **Base Metal** | | **Weld Metal** | | **FSPed Weld Metal** | |
|---|---|---|---|---|---|---|
| | Optical | CMOD | Optical | CMOD | Optical | CMOD |
| **C**x$10^{-10}$ | 1.4±0.1 | 3.1±2.1 | 0.3±0.3 | 0.51±4.0 | 4.1±3.9 | 30 ±10 |
| **m** | 3.36±0.02 | 3.23±0.27 | 4.83±1.19 | 4.00±0.38 | 2.88±0.61 | 1.99±0.43 |
| **da/dN*** | 1.2E-06 | 1.9E-06 | 1.5E-06 | 2.6E-06 | 9.8E-07 | 6.6E-07 |
| **da/dN*** | 1.3 x$10^{-06}$ ± 1.9 x$10^{-07}$ | | 2.1 x$10^{-06}$ ± 1.1 x$10^{-06}$ | | 8.2 x$10^{-07}$ ± 1.6 x$10^{-07}$ | |

*(1/m) Average @ $\Delta K=15$ MPa $m^{1/2}$

# CHAPTER 5

# DISCUSSION

## 5.1. Effect of Processing Parameters on Local Temperature

In Figure 96 and Figure 97, the effects of rotation and travel speed on temperature are shown. Constant travel and rotational speed were chosen as 21 mm/min. and 355 rpm respectively. At constant travel speed, 560 rpm and 900 rpm were selected as varying rotational speeds. The maximum temperatures measured were found to be approximately 400°C for lower rpm and 450°C for faster rotational speed.

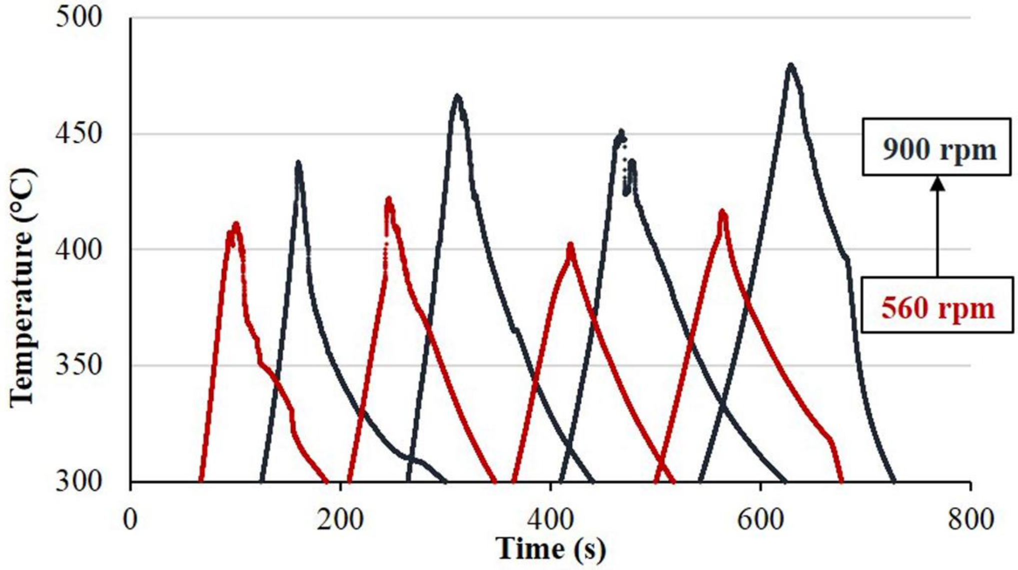

Figure 96. Temperature vs time for constant travel speed and different rotational speeds (21 mm/min. constant travel speed).

The varying travel speeds selected for the constant rotational speed were 21 and 43 mm/min. While maximum temperature was approximately 300°C for the lower travel speed of 21 mm/min; approximately 420°C was measured for 43 mm/min.

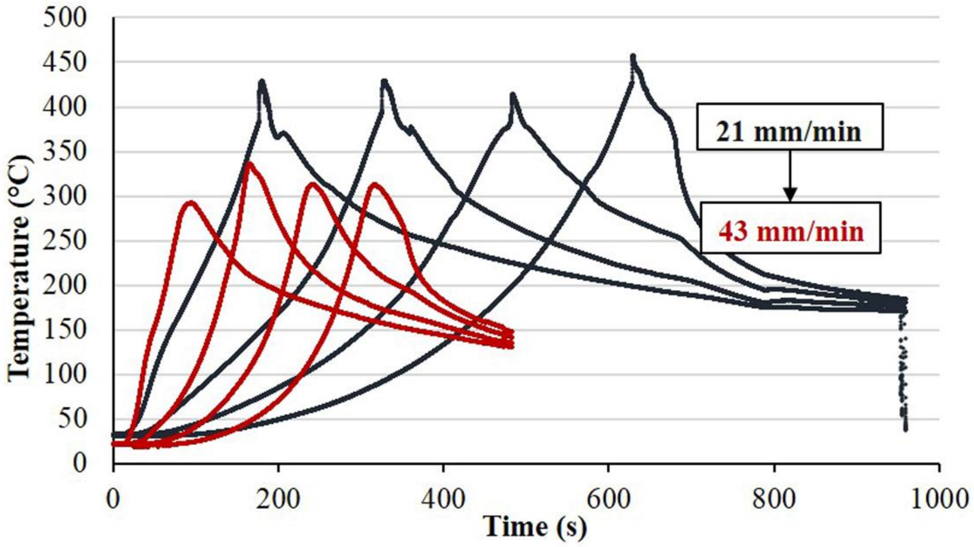

Figure 97. Temperature vs time for constant rotational speed & varying travelling speeds (355 rpm constant rotational speed).

Rotational speed and travel speed has been found to affect maximum temperature in opposite ways. While higher temperatures are reached with increased rotational speed, the maximum temperature decreases when slower travel speed is used.

### 5.2. Effect of Tool Features

Three types of tool geometries were used in this study. Geometrical features are summarized in Table 14.

Table 14. Tool Geometries.

| | A01 | Triflute | Triflat |
|---|---|---|---|
| **Pin Geometry** | Truncated cone | Truncated cone | Truncated cone |
| **Pin Features** | Threads | Threads & 3 Flutes | Threads & 3 Flats |
| **Shoulder Shape** | Flat | Convex | Convex |
| **Shoulder Feature** | - | Scroll | Scroll |

The best results were obtained by triflat tool in terms of their susceptibility to tunnel formation. A01 tool was tilted normal to workpiece surface in order to retard tunnel formation; however, it could not be prevented (Figure 98a, b). Friction stir processing done by tool triflute caused tool breakage multiple times. Defect-free FSPed plates were obtained in limited number of passes. Most of trials with tool triflat tool was defect-free. For example, both 720 rpm- 100 mm/min. (Figure 98c) and 290 rpm-100 mm/min. process parameter did not show any macro defects.

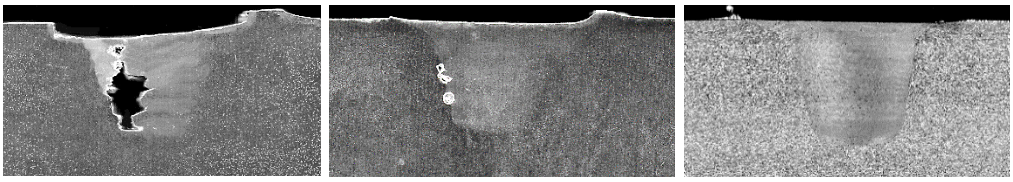
(a) (b) (c)

Figure 98. Macrographs of FSPed samples (a) and (b) by tool A01, (c) by Triflat.

Scrolls on the shoulder of triflute and triflat tools lead the material flow from shoulder towards the pin. Therefore, the channel structure of shoulder eliminate the necessity to tilt the tool [4].

Convex shoulders with scrolls are usually preferred for friction stir welding. This type of tool offers flexibility in the contact area between the shoulder and workpiece because these features directs material movement to pin [4]. Since frictional heat of shoulder is a major heat source, optimization of process parameters can be easier and better properties can be obtained.

Pin features on the tools triflute and triflat improves material flow; thus, tunnel formation is prevented. Threads and flutes are favored to aid the flow of metal and to reduce axial and transverse forces [20]. Addition of flat regions cause a turbulent flow of plasticized material [4, 48]. In Figure 99, two-dimensional metal flow in friction stir welding with a tool that has three flat sides is given. The deformation around the flats results in bulging of the streamlines shown in Figure 99c and d.

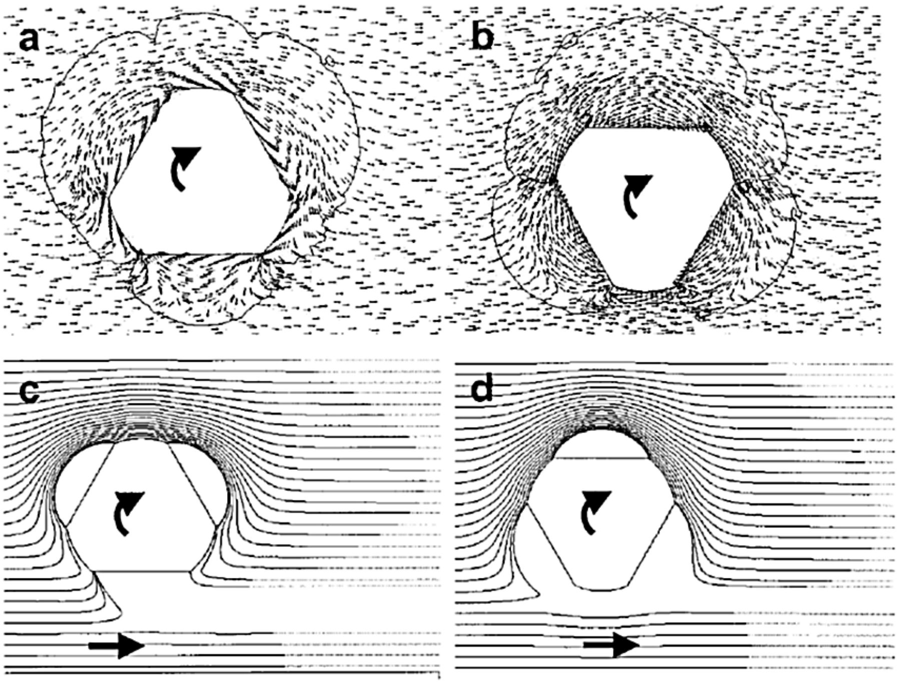

Figure 99. 2D material flow model of triflat tool
(a) Velocity vectors, (b) Rotated 60º, (c) streamlines, (d) Rotated 60º [48].

## 5.3. Effect of Processing Heat Input on Grain Size

In Figure 100, microstructure and temperature-time graphs of two processing trials are given. Processing parameters were 900 rpm- 21 mm/min. for DN3 and 355 rpm- 68 mm/min. for DN10. Since higher ratio of rotational speed to travel speed causes more heat generation, measured temperatures were found to be higher for DN3 trial. Maximum temperature measured near the shoulder of tools were approximately 465ºC for DN3 and 310ºC for DN10. Average readings of thermocouples show that time of exposure is also higher for DN3 trial. The micrographs of nugget show coarser grains for DN3 trial than DN10 trial.

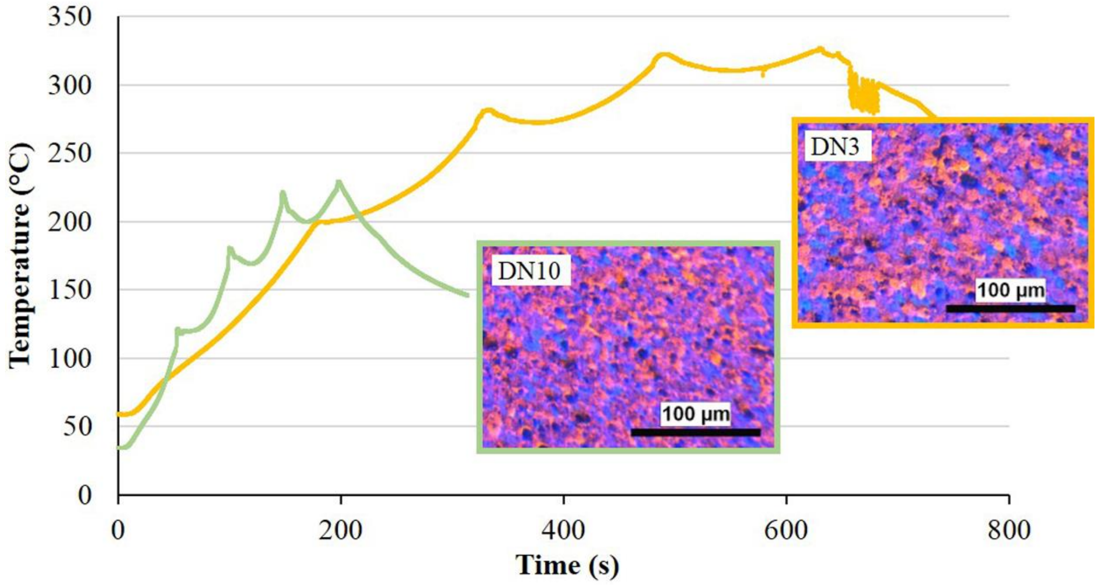

Figure 100. Temperature vs time graph of DN3 and DN10 trials.

The high heat input and low heat input trials (see Section 4.2.2.1.) done with triflat tool gave an average grain size of 6 and 1 µm respectively. Smaller grain size compared to base material are obtained by recrystallization triggered with friction stir processing. The final grain size of nugget was determined to be affected by the temperature of processed zone and exposure time. Higher temperature and longer time of exposure are believed to give rise to grain growth of newly formed grains. Therefore, the finer grain size were obtained by using process parameters for which heat generation is lower.

### 5.4. Effect of Processing on Hardness

Measured hardness of nugget was found to be uniform with standard deviation of 2-3 HV2 even in multi-pass studies. However, scatter of hardness values was high for base metal and weld metal. In Figure 101, average hardness values are given. Hardness is seemed to decrease with increasing amount of heat input. Weld metal which experiences highest temperature has lowest hardness. Hardness of nugget region increases by using smaller ratio of rotational speed to travel speed i.e. cooler processing. In high input study, a heat affected zone (HAZ) that have lower hardness than the base metal and nugget is observed.

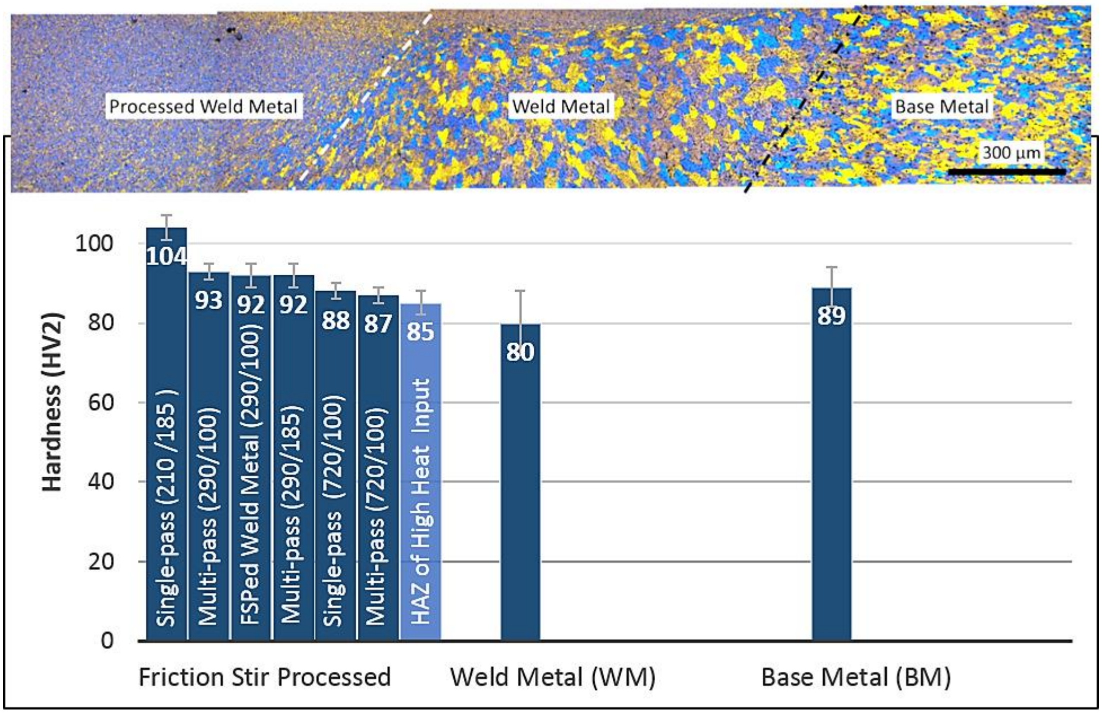

Figure 101. Average hardness values with representative micrograph. (Ratios of rotational speed to travel speed are given in parentheses.)

Hardness can be affected by particle density, elements in solid solution, grain size and dislocation density. Dissolution, growth or re-precipitation of small particles can occur while large particles can be broken into smaller ones. Thus, solid-solution hardening and precipitate hardening can be observed. For example, friction stir processing can cause dissolution of $Mg_xSi$ particles which can increase hardness by solid solution strengthening of magnesium [49]. Although the final size depends on the process parameters, recrystallization mechanism refines grains. Consequently, grain boundary strengthening can occur. Stirring action of processing can improve strength by strain hardening. In multi-pass studies, sequent passes could have affected prior passes. Therefore, the strain hardening level could have increased compared to unaffected nugget structure.

Chemical composition of weld metal could have changed with FSP since a small part of the base metal was inside the stir zone. Consequently, hardness of weld metal could have increased due to solid solution strengthening.

In their study, Yutaka et al. [50] suggest that hardness of friction stir welded 5083-O plate can be explained by the distribution of small particles of $Al_6$(Fe,Mn) (< 2 μm). The pinning effect of small particles can dominate the hardness rather than the effect of grain boundaries. In literature, it has been shown by TEM analysis that small particles are distributed in friction stir processed 5083 aluminum alloy [49, 50]. Therefore, main hardening mechanism behind FSPed weld metal can be increased dislocation density and its interaction with small $Al_6$(Mn,Fe) particles. Effect of grain refinement is found to be negligible because although the difference of grain sizes the hardness of base metal and FSPed regions are similar.

Lower hardness of high heat input trial can be explained by grain growth and recovery which result in less grain boundary and strain hardening. The heat affected zone might have formed due to recovery of cold-worked structure. Precipitate strengthening effect of secondary phases at HAZ, if present, might have diminished due to growth of particles.

## 5.5. Near Threshold Fatigue Crack Growth

Because roughness induced closure is more apparent in coarse-grained material, fine grain size of friction stir processed weld metal is expected to lower fatigue crack threshold. However, compressive residual stress has been said to compensate the detrimental effect of grain size [51, 52]. Residual stress distribution of friction stir welded plates is shown to depend on processes parameters [53]. While tensile stresses can be found, the severity of stresses are lower than gas metal arc welding [4, 54]. Tensile stresses are known to generally exist in weld metal in arc welded structures; however, weldments done in multiple passes can have compressive stress in fusion zone. For example, weld bead sequence and residual stress distribution of a 5 pass butt weld is shown in Figure 102.

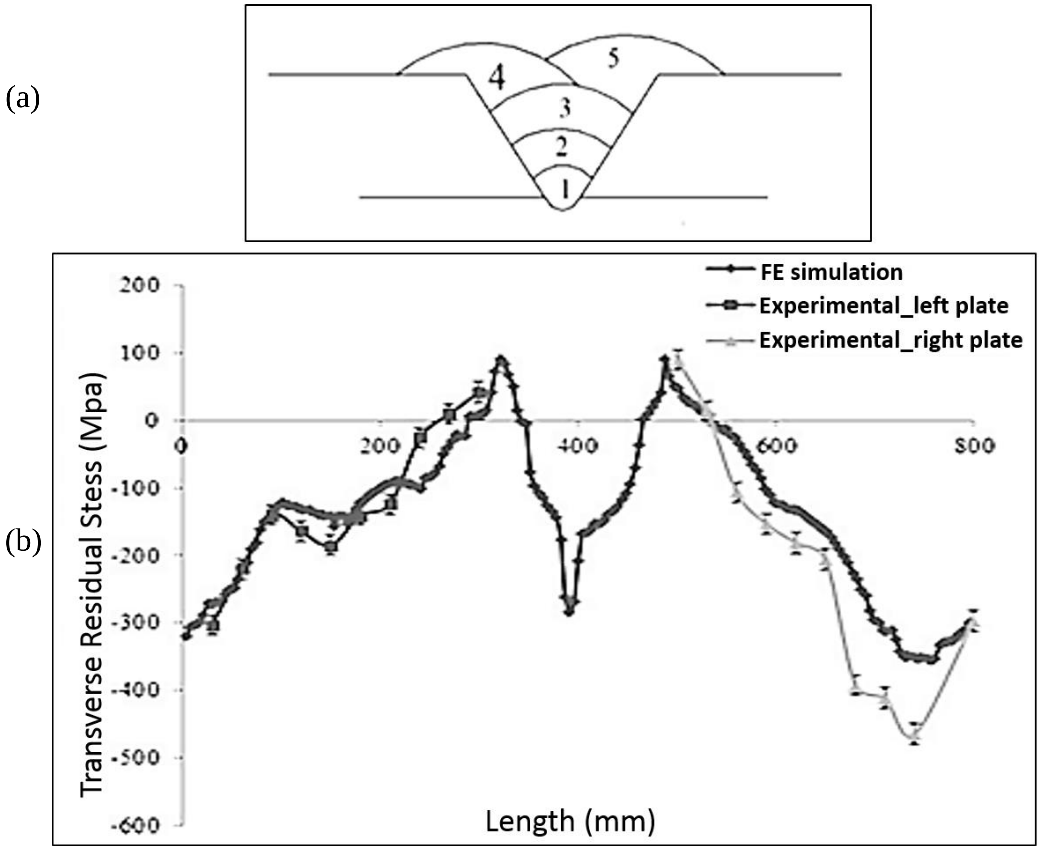

Figure 102. (a) Weld bead sequence, (b) Transverse residual stress at the top surface of the weld plate [55].

In Figure 103, fracture surfaces of the compact tension samples are given. Transgranular fracture is more evident in the weld metal and the base metal. Surface irregularities on the fracture surface can be seen due to welding defects in the as-welded samples. Striations are visible in all type of specimens. Although FSPed weld metal has more tortuous surface microscopically, crack deflection can be less effective compared to macroscopically rougher surface of weld and base metal samples.

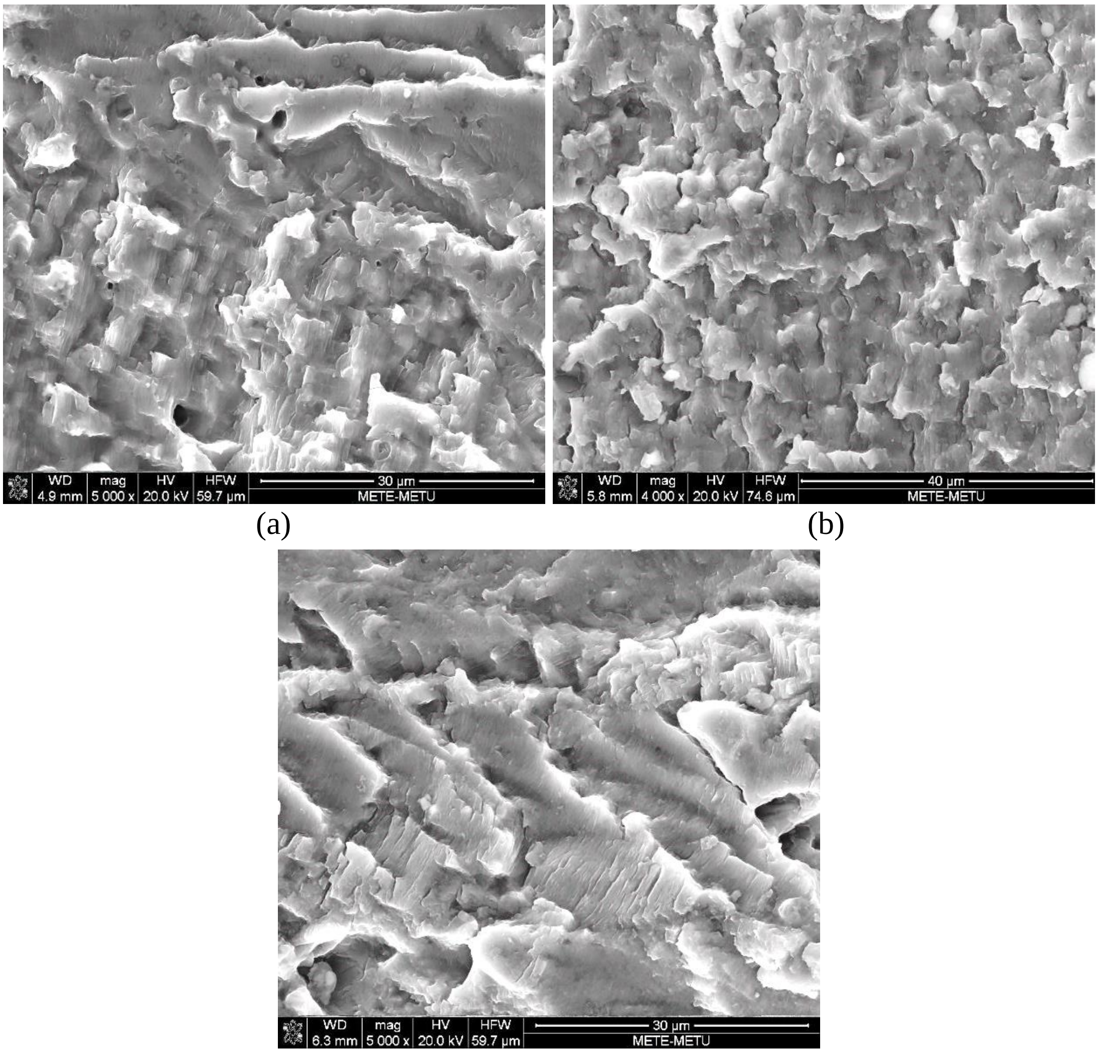

(a) (b)

(c)

Figure 103. Fracture surfaces near threshold
(a) Weld metal, (b) FSPed weld metal, (c) Base metal.

At low stress intensity levels, the crack growth rate is minimum in the weld metal. One possible reason is the high strain hardening capacity increasing the plasticity induced closure.

### 5.6. Steady State Fatigue Crack Growth

In Figure 104, fatigue crack curves obtained by calculated Paris-Erdoğan coefficients are given. While the crack growth rate in the as-welded sample is highest, crack growth resistance of FSPed weld metal is found to be highest.

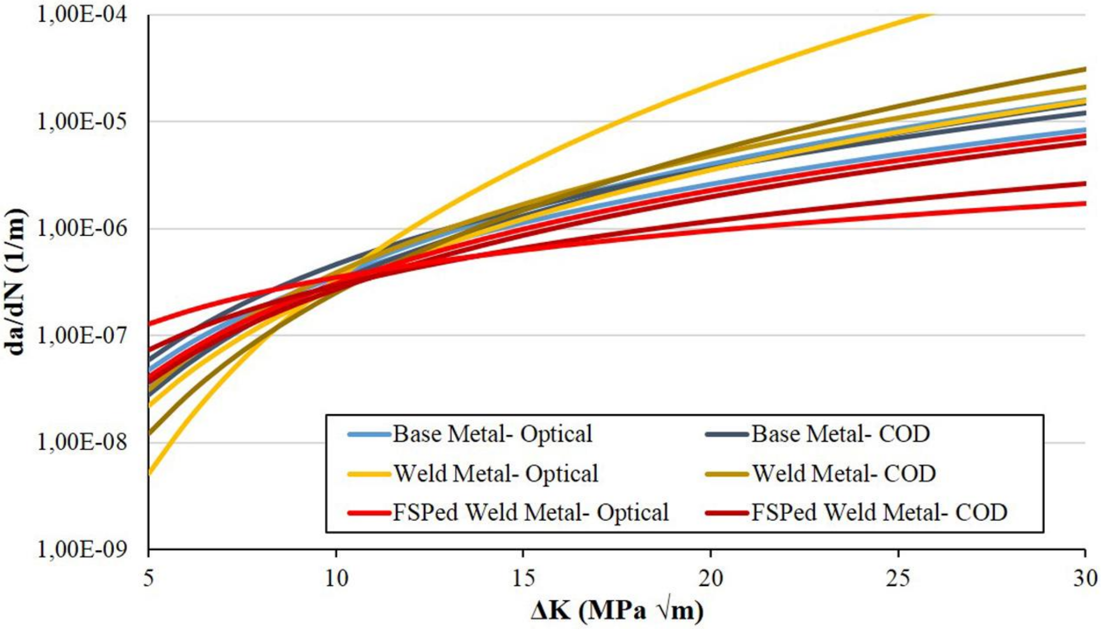

Figure 104. Fatigue crack growth curves obtained by using the calculated coefficients “C and m”.

Side views of the fractured compact tension specimens are given in Figure 105. Slip lines parallel to crack growth direction are observed in the as-welded specimens. Few side cracks are also observed. However, their number is greater on the fracture surface of the FSPed weld metal. Formation of these features might have increased the energy required for crack growth.

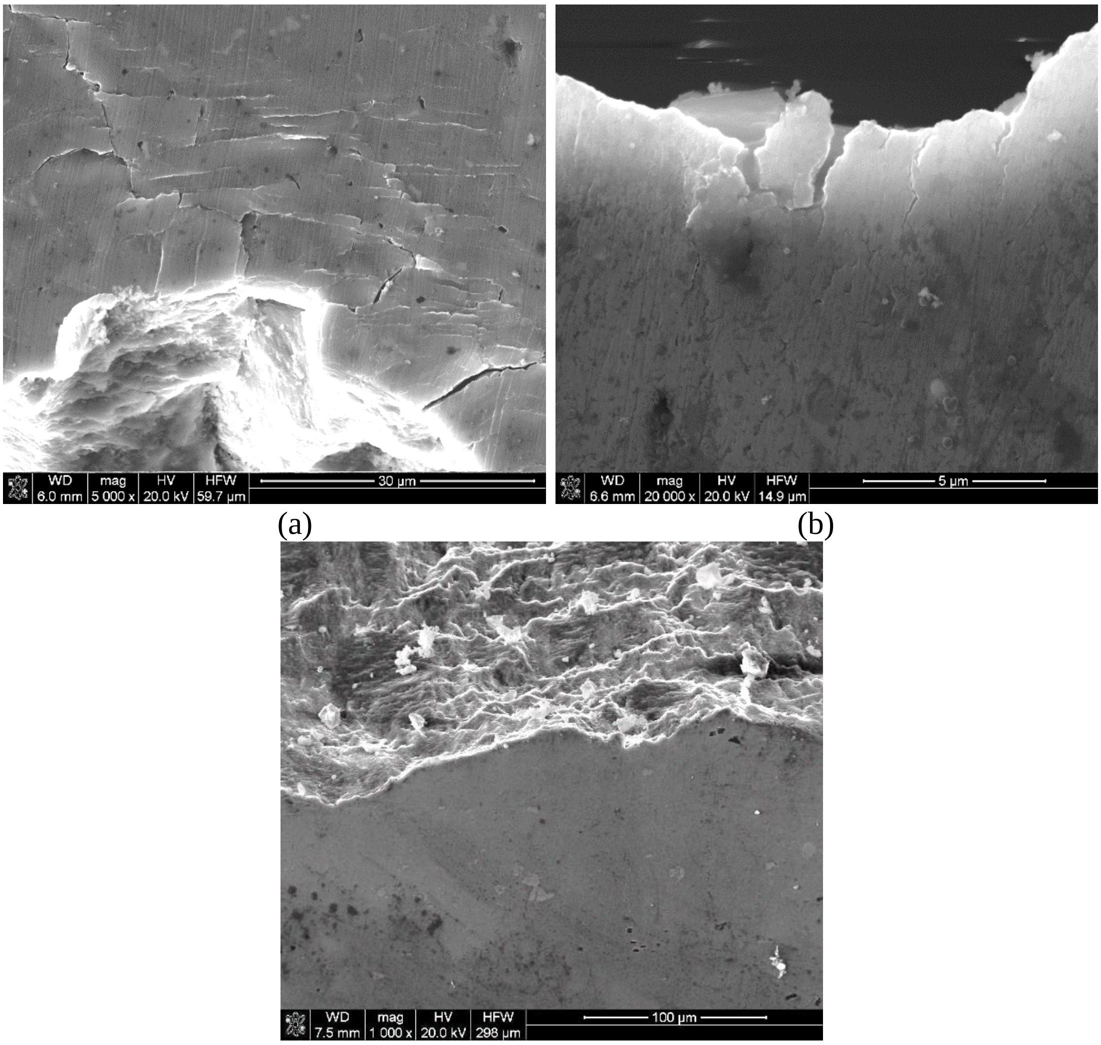

(a) (b)

(c)

Figure 105. Side views of the crack line at steady stage
(a) As-welded, (b) FSPed weldment, (c) Base metal.

Fracture surfaces of the specimens are shown can be seen in Figure 106. The major features of the as-welded samples are welding defects. FSPed weld metal consists of small hills which are larger than the grain size. Fracture surfaces of the base metal include high amount of secondary particles.

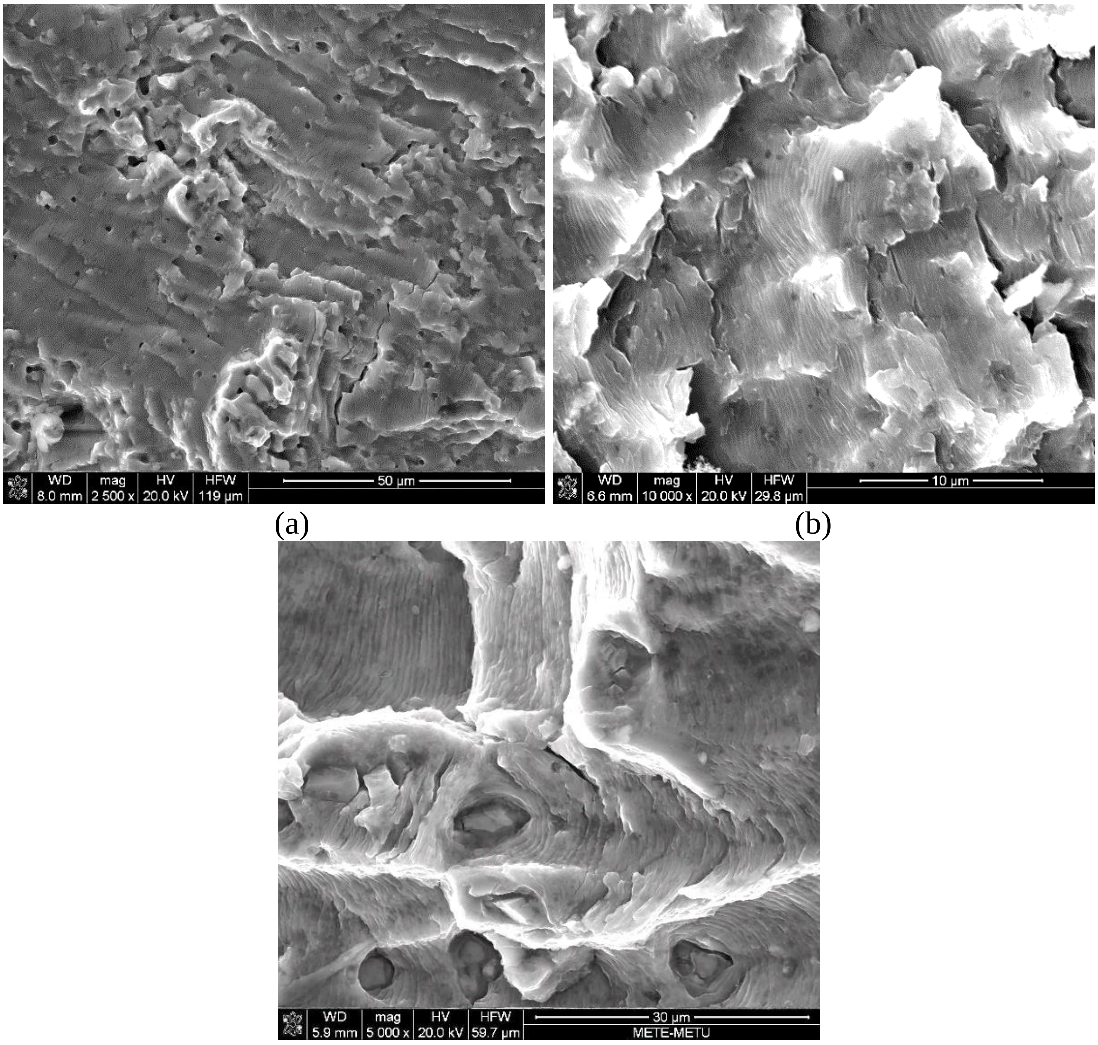

(a) (b)

**(c)**

Figure 106. Fracture surface at steady stage
(a) As-welded, (b) FSPed weldment, (c) Base metal.

Gas voids and slag inclusions are shown in Figure 107. In addition to voids as big as 100 µm, micro-voids are also present throughout the specimen. Crack growth seems to be affected locally due to increased density of porosity.

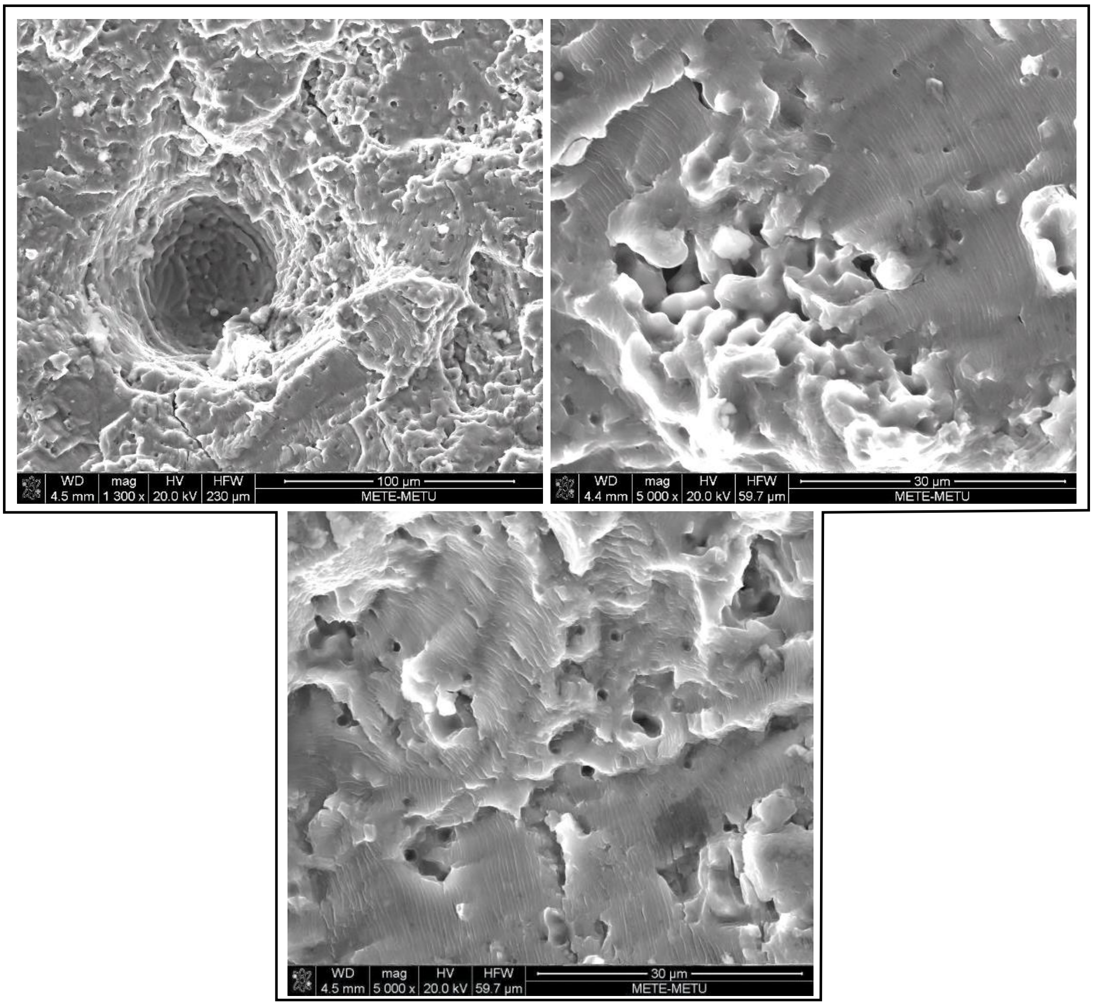

Figure 107. Welding defects found on the fracture surfaces of the compact tension samples.

Many secondary phase particles exist on the fracture surfaces of the base metal specimen which were fractured and segregated from matrix (Figure 108). They seem to have promoted void formation.

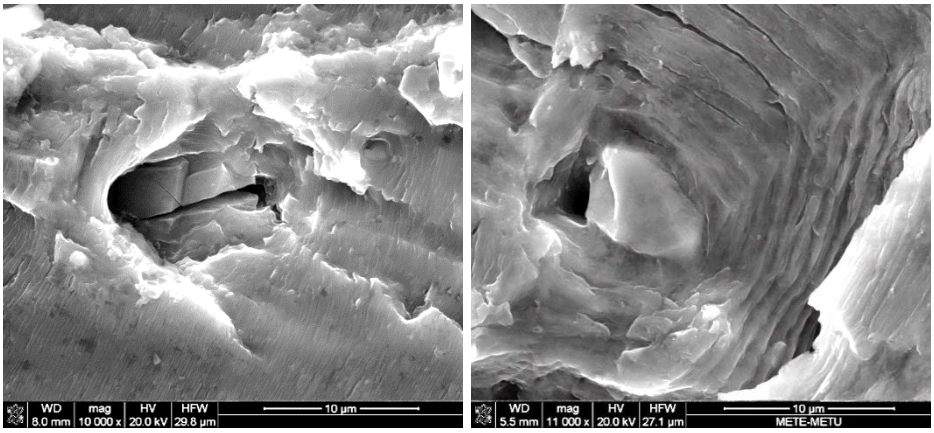

Figure 108. Secondary particles on the fracture surfaces of the base metal.

The overall crack growth rate could be affected by welding defects and residual stresses. The main reason behind rapid crack growth rate of weld metal is thought to be defects decreasing the load carrying area. The superior fatigue crack growth behavior of FSPed weld metal can be due to compressive residual stress.

# CHAPTER 6

# CONCLUSION

The effects of friction stir processing (FSP) on the grain structure and mechanical properties of welded 20 mm thick Al-5083 H111 plates were investigated. A preliminary study was done on the effect of FSP on base metal. The type, rotational speed, and travel speed of the FSP tool were decided by optimization trials. Microstructural examination, hardness and tensile test were done. Afterwards, effects of FSP on weld metal was investigated in terms of microstructure, hardness, tensile, fracture toughness and fatigue crack growth.

Following conclusions can be drawn from this particular study:

1. FSP of base metal:

- The initial optimization trials of FSP showed that the tunnel formation risk is minimum for triflat tool in comparison with the triflude and simple treaded tools.
- 2-12% reduction in the average grain size is possible depending upon the FSP parameters.
- Increasing the ratio of rotational speed to travel speed increases the maximum local temperature. Consequently, high heat input causes wider TMAZ and the formation of HAZ outside the nugget.
- Hardness and tensile properties depend on the processing parameters. While the yield strength and hardness decreased in higher heat input samples, tensile strength and hardness increased in lower heat input samples.
- Single-pass and multi-pass FSP forms similar grain size and hardness profiles.

2. FSP of weld metal

- FSP eliminates macro defects like lack of penetration and micro defects like porosity.
- FSPed weld metal has better mechanical properties compared to the unprocessed weld metal in terms of tensile strength, hardness, fracture toughness and crack growth resistance at Paris regime.
- Fractography of tensile, fracture toughness and fatigue crack growth specimens revealed secondary particles of which are mostly broken on base metal; micro discontinuities like porosity on weld metal; distinct patterns on FSPed weld metal specimens.
- Beach marks were present on the fracture surface of fatigue crack growth specimen of FSPed weld metal. Fractography revealed rough surface with striations.

# CHAPTER 7

# RECOMMENDATIONS FOR FURTHER STUDIES

In this study effect of friction stir processing on fatigue and tensile properties were investigated; however, residual stress which has a major effect on crack growth behavior could not be analyzed. Therefore, residual stress analysis of multi-pass FSP should be studied.

Microstructure analysis were done with optical microscope and scanning electron microscope (SEM). Chemical analysis of secondary particles were done by EDS; however, detailed examination could not be done. Size, shape, chemical structure and amount of secondary phases should be studied.

Fractography of FSPed samples showed distinct features that were not encountered in base metal or weld metal. Beach marks were also visible on fatigue crack growth specimens of FSPed specimens. The differences and mechanism of formation of these features in the stir zone can be studied.

# REFERENCES

[1] G. Mathers, The Welding of Aluminium and Its Alloys, England: Woodhead Publishing, 2002.

[2] Y. Liu, W. Wang, J. Xie, S. Sun, L. Wang, Y. Qian, Y. Meng, Y. Wei,, "Microstructure and mechanical properties of aluminum 5083 weldments by gas tungsten arc and gas metal arc welding," *Materials Science and Engineering A*, vol. 549, pp. 7-13, 2012.

[3] S. Malarvizhi, V. Balasubramanian, "Effect of welding processes on AA2219 aluminium alloy joint properties," *Transactions of Nonferrous Metals Society of China*, vol. 21, no. 5, pp. 962-973, 2011.

[4] R. S. Mishra, M. W. Mahoney, Friction Stir Welding and Processing, United States of America: ASM International, 2007.

[5] K. Nakata,Y.G. Kim, H. Fujii, T. Tsumura, T. Komazaki, "Improvement of mechanical properties of aluminum die casting alloy by multi-pass friction stir processing," *Materials Science and Engineering: A*, vol. 437, no. 2, pp. 274-280, 2006.

[6] Z. Y. Ma, A. L. Pilchak, M. C. Juhas, J. C. Williams,, "Microstructural refinement and property enhancement of cast light alloys via friction stir processing," *Scripta Materialia*, vol. 58, no. 5, pp. 361-366, 2008.

[7] M. L. Santella, T. Engstrom, D. Storjohann, T. Y. Pan, "Effects of friction stir processing on mechanical properties of the cast aluminum alloys A319 and A356," *Scripta Materialia*, vol. 53, no. 2, pp. 201-206, 2005.

[8] Y. Jiang, D. Lu, M. Zhou, S. Wei, R. Zhou, "The Mechanical Properties of Al-30Si Alloy by Friction Stir Processing," *Advanced Materials Research,* Vols. 189 - 193, pp. 3601-3604, 2011.

[9] L. Karthikeyan, V.S. Senthilkumar, V. Balasubramanian, "Mechanical property and microstructural changes during friction stir processing of cast aluminum 2285 alloy," *Materials & Design,* vol. 30, no. 6, p. 2237–2242, 2009.

[10] Z. Y. Ma, S. R. Sharma, R. S. Mishra, "Effect of multiple-pass friction stir processing on microstructure and tensile properties of a cast aluminum–silicon alloy," *Scripta Materialia,* vol. 54, no. 9, p. 1623–1626, 2006.

[11] ESAB Knowledge center, "Understanding the Aluminum Alloy Designation System," 26 March 2014. [Online]. Available: http://www.esab.ca/ca/en/education/blog/understanding-the-aluminum-alloy-designation-system.cfm. [Last Accessed on January 12, 2015].

[12] G. E. Tot ten, D. S. MacKenzie, Handbook of Aluminum, New York: Marcel Dekker, 2003.

[13] R. D. Joseph, Aluminum and aluminum alloys, ASM International, 1993.

[14] J. Nadzam, "GMAW Welding Guide," Lincoln Electric.

[15] J. H. Dudas, F. R. Collins, "Preventing welding cracks in high-strength aluminum alloys," *Welding Journal,* vol. 45, no. 6, pp. 241-249, 1966.

[16] P. L. Threadgill, A. J. Leonard, H. R. Shercliff, P. J. Withers, "Friction stir welding of aluminium alloys," *International Materials Reviews,* vol. 54, no. 2, pp. 49-93, 2009.

[17] H. J. K. Lemmen , R. C. Alderliesten, R. Benedictus, "Macro and microscopic observations of fatigue crack growth in friction stir welded aluminum joints," *Engineering Fracture Mechanics,* vol. 78, p. 930–943, 2011.

[18] J. Su, Tr. W. Nelson, C. J. Sterling, "Microstructure evolution during FSW/FSP of high strength aluminum alloys," *Materials Science and Engineering A*, vol. 405, p. 277–286, 2005.

[19] R. M. Miranda, J. Gandra and P. Vilaça, "Surface Modification by Friction Based Processes," InTech, 2013. [Online]. Available: http://www.intechopen.com/books/modern-surface-engineering-treatments/surface-modification-by-friction-based-processes. [Last Accessed on March 08, 2015].

[20] R. Rai, A. De, H. K. D. H. Bhadeshia, T. DebRoy, "Review: friction stir welding tools," *Science and Technology of Welding and Joining,* vol. 16, no. 4, pp. 325-342, 2011.

[21] F. Hidetoshi, C. Ling, M. Masakatsu, N. Kiyoshi, "Effect of tool shape on mechanical properties and microstructure of friction stir welded aluminum alloys," *Materials Science and Engineering A*, vol. 419, pp. 25-31, 2006.

[22] W. M. Thomas, D. G. Staines, E. D. Nicholas, P. Evans, "Reversal Stir Welding-Re-Stir-Preliminary trials," TWI , 2003. [Online]. Available: http://www.twi-global.com/news-events/connect/2003/march-april-2003/re-stirtm-reversal-stir-welding/. [Last Accessed on October 23, 2014].

[23] J. Gandra, R.M. Miranda, P. Vilaça, "Effect of overlapping direction in multipass friction stir processing," *Materials Science and Engineering A*, vol. 528, p. 5592–5599, 2011.

[24] C. Bathias, A. Pineau, Fatigue of Materials and Structures Fundamentals, ISTE Ltd and John Wiley & Sons, Inc., 2010.

[25] C. Kranenburg, Fatigue crack growth in Aluminium Alloys, Technische Universiteit Delft.

[26] J. Schijve, Fatigue of Structures and Materials, Springer Science+Business Media, B.V., 2009.

[27] N. Perez, Fracture Mechanics, United States of America: Kluwer Academic Publishers, 2004.

[28] A. L. Biro, B. F. Chenelle, D. A. Lados, "Processing, Microstructure, and Residual Stress Effects on Strength and Fatigue Crack Growth Properties in Friction Stir Welding: A Review," *Metallurgical and Materials Transactions B* , vol. 43B, pp. 1622-1637, 2012.

[29] P. P. Milella, Fatigue and Corrosion in Metals, Springer-Verlag Italia, 2013.

[30] G. Powell, "Elevated-Temperature Failures," *ASM Handbook: Failure Analysis and Prevention,* vol. 11, p. 263–297, 1986.

[31] T. L. Anderson, Fracture Mechanics: Fundamentals and Applications, CRC Press, 2005.

[32] R. M. J. Kemp, "Fatigue Crack Closure-A Review," Royal Aerospace Establishment, 1990.

[33] P. S. Pao, H. N. Jones, S. F. Cheng, C. R. Feng, "Fatigue crack propagation in ultrafine grained Al–Mg alloy," *International Journal of Fatigue,* vol. 27, p. 1164–1169, 2005.

[34] P. K. Liaw, "Overview of Crack Closure at Near-Threshold Fatigue Crack Growth Levels," in *Mechanics of Fatigue Crack Closure*, Philadelphia, American Society for Testing and Materials, 1988, pp. 62-92.

[35] J. da Silva, J.M. Costa ⥣, A. Loureiro, J.M. Ferreira, "Fatigue behaviour of AA6082-T6 MIG welded butt joints improved by friction stir processing," *Materials and Design,* vol. 51, p. 315–322, 2013.

[36] J. D. M. Costa, J. S. Jesus, A. Loureiro, J. A. M. Ferreira, L. P. Borrego, "Fatigue life improvement of mig welded aluminium T-joints by friction stir processing," *International Journal of Fatigue,* vol. 61, p. 244–254, 2014.

[37] C. B. Fuller, M. W. Mahoney, "The Effect of Friction Stir Processing on 5083-H321/5356 Al Arc Welds: Microstructural and Mechanical Analysis," *Metallurgical and Materials Transactions A,* vol. 37A, pp. 3605-3615, 2006.

[38] L. P. Borrego, J. D. Costa, J. S. Jesus, A. R. Loureiro, J. M. Ferreira, "Fatigue life improvement by friction stir processing of 5083 aluminium alloy MIG butt welds," *Theoretical and Applied Fracture Mechanics,* vol. 70, p. 68–74, 2014.

[39] J. R. Rule, J. M. Rodelas, J. C. Lippold, "Application of Friction Stir Processing as a Pretreatment to Fusion Welding," *Welding Journal,* vol. 92, no. 10, pp. 283-290, 2013.

[40] J.P. Nobre, A.C. Batista, J.R. Kornmeier, J.D. Costa, A. Loureiro, "Neutron and X-ray Diffraction Residual Stress Measurements in Aluminium Alloys MIG Welded T-Joints after Friction Stir Processing," *Advanced Materials Research,* vol. 996, pp. 439-444, 2014.

[41] ASTM B209M, "Standard Specification for Aluminum and Aluminum-Alloy Sheet and Plate (Metric)," 2014.

[42] AWS Committee on Filler Metals and Allied Materials, "AWS A5.10 Specification for Bare Aluminum and Aluminum-Alloy Welding Electrodes and Rods," 1999.

[43] "EN ISO 17636-1 Non-destructive testing of welds - Radiographic testing - Part 1: X- and gamma-ray techniques with film," 2013.

[44] ASTM E112, Standard Test Methods for Determining Average Grain Size, 2013.

[45] ASTM E399, Standard Test Method for Linear-Elastic Plane-Strain Fracture Toughness KIc of Metallic Materials, 2012.

[46] ASTM E647, Standard Test Method for Measurement of Fatigue Crack Growth Rate, 2013.

[47] J. R. Flores Ramirez, The Role of Magnesium in the Electrochemical Behaviour of 5XXX Aluminium-Magnesium Alloys, 2006.

[48] P. A. Colegrove, H. R. Shercliff, "Two-dimensional CFD modelling of flow round profiled FSW tooling," *Science and Technology of Welding and Joining,* vol. 9, no. 6, pp. 483-492, 2004.

[49] M. M. Attallah, Microstructure-Property Development In Friction Stir Welds Of Aluminium-Based Alloys, University of Birmingham, 2007.

[50] Y. S. Sato, S. Hwan, C. Park, H. Kokawa, "Microstructural Factors Governing Hardness in Friction-Stir Welds of Solid-Solution-Hardened Al Alloys," *Metallurgical and Materials Transactions A,* vol. 32A, pp. 3033-3042, 2001.

[51] R. W. Fonda, P. S. Pao, H. N. Jones, C. R. Feng, B. J. Connolly, A. J. Davenport, "Microstructure, mechanical properties, and corrosion of friction stir welded Al 5456," *Materials Science and Engineering A,* vol. 519, p. 1–8, 2009.

[52] K. Sangshik, G. L. Chang, K. Sung-Joon, "Fatigue crack propagation behavior of friction stir welded 5083-H32 and 6061-T651 aluminum alloys," *Materials Science and Engineering A,* vol. 478, p. 56–64, 2008.

[53] P. Cavaliere, "Friction stir welding of Al alloys: analysis of processing parameters affecting mechanical behavior," in *Pasquale Cavaliere / Procedia CIRP*, 2013.

[54] W. Lei, T. Mitsuyosi, "Comparison of Residual Stress Between MIG Welding and Friction Stir Welding," *Applied Mechanics and Materials,* Vols. 155-156, pp. 1218-1222, 2012.

[55] R.R. Chand, I.S. Kim b, J.P. Lee, Y.S. Kim, D.G. Kim, "Numerical and experiment study of residual stress and strain in multi-pass GMA welding," *Journal of Achievements in Materials and Manufacturing Engineering,* vol. 57, no. 1, pp. 31-37, 2013.